



Fig. 4.8 Optical microstructure of a specimen helium quenched from 420 °C after bainite transformation.

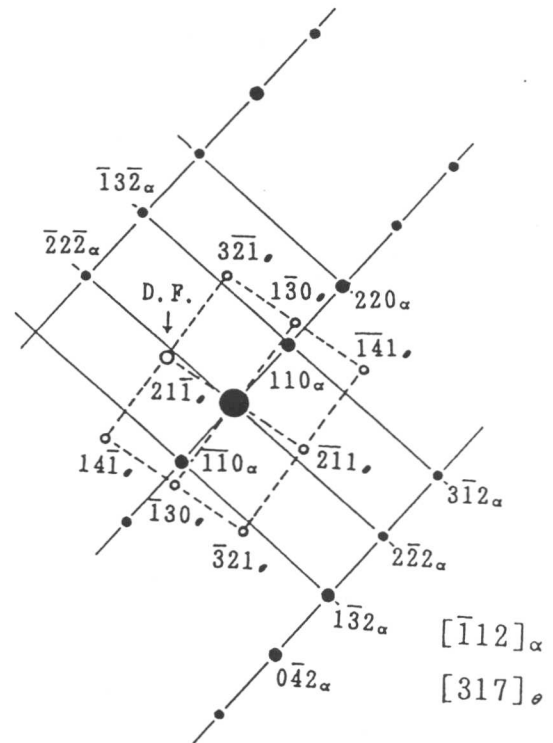
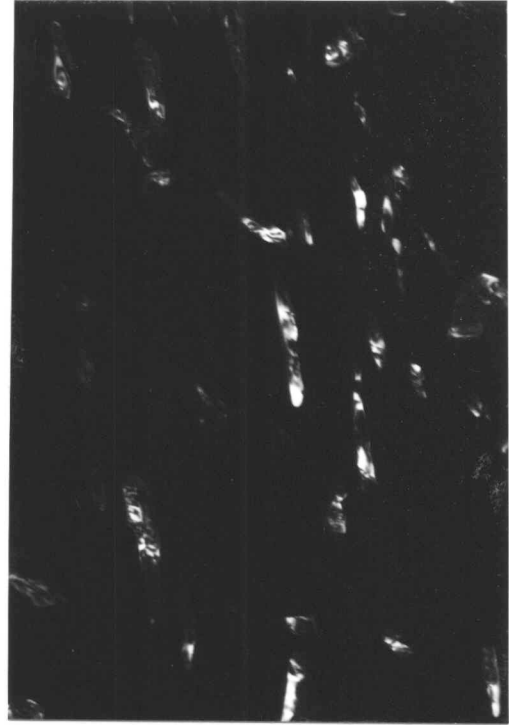
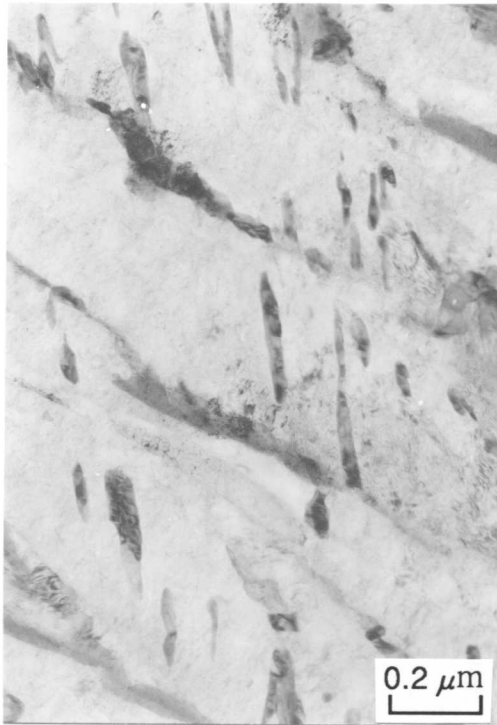


Fig. 4.9 TEM bright field image of the initial lower bainitic microstructure and a dark field image of cementite particles.



Fig. 4.10 TEM bright field image of lower bainite after 23 days of isothermal holding at 478 °C.

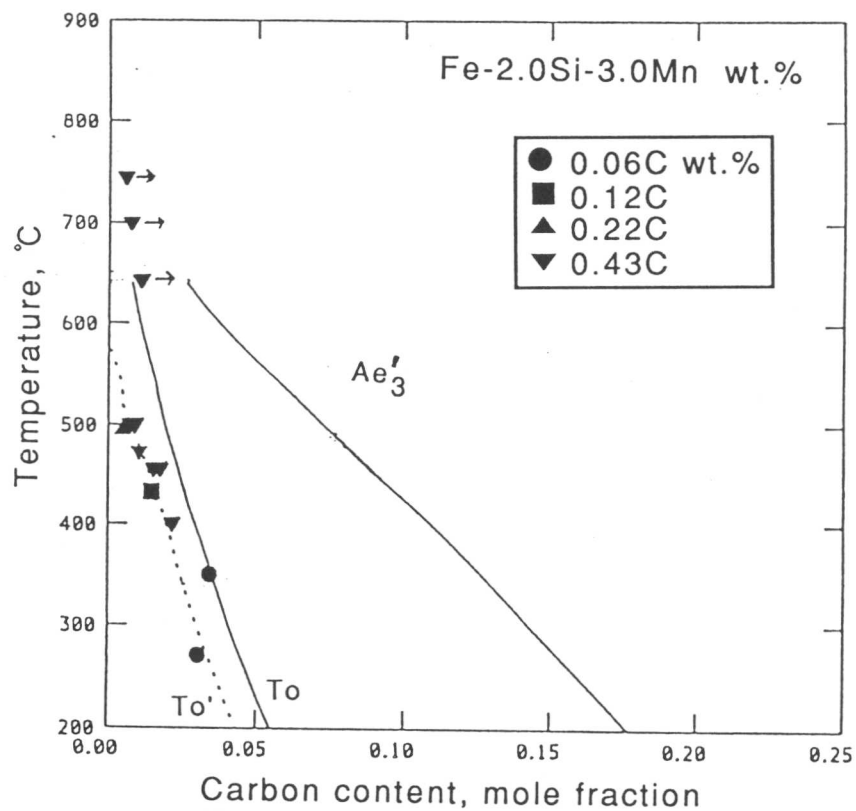
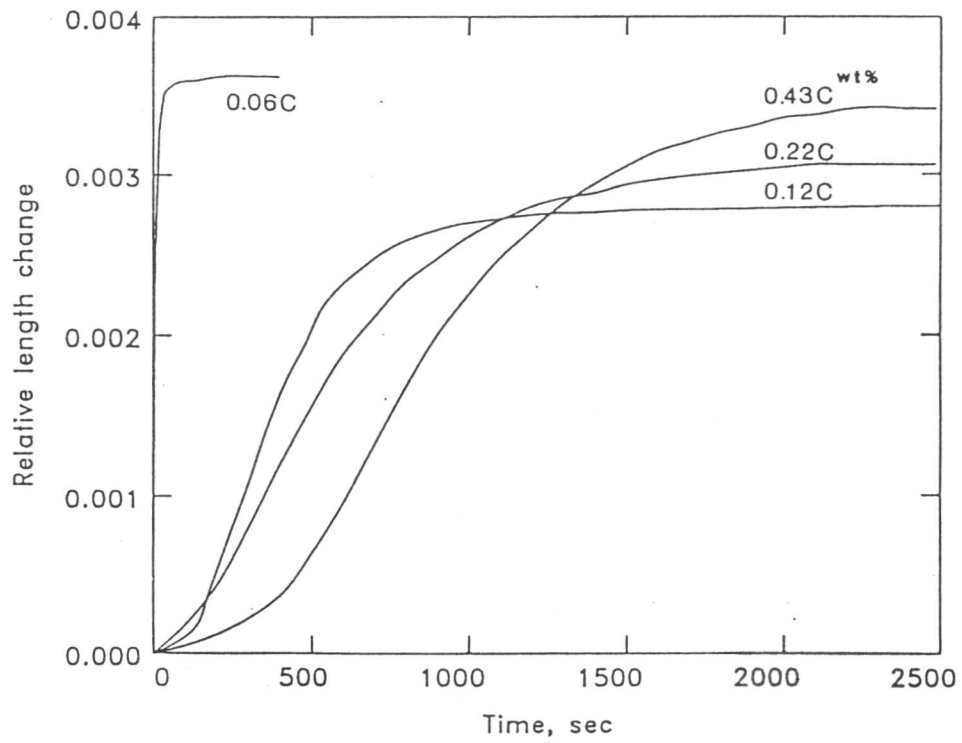


Fig. 4.11 Relative length change during isothermal bainite transformation at each reaction temperatures (a) and calculated phase diagram of the Fe-2.0Si-3.0Mn system with plots of calculated carbon concentration of residual austenite (b).

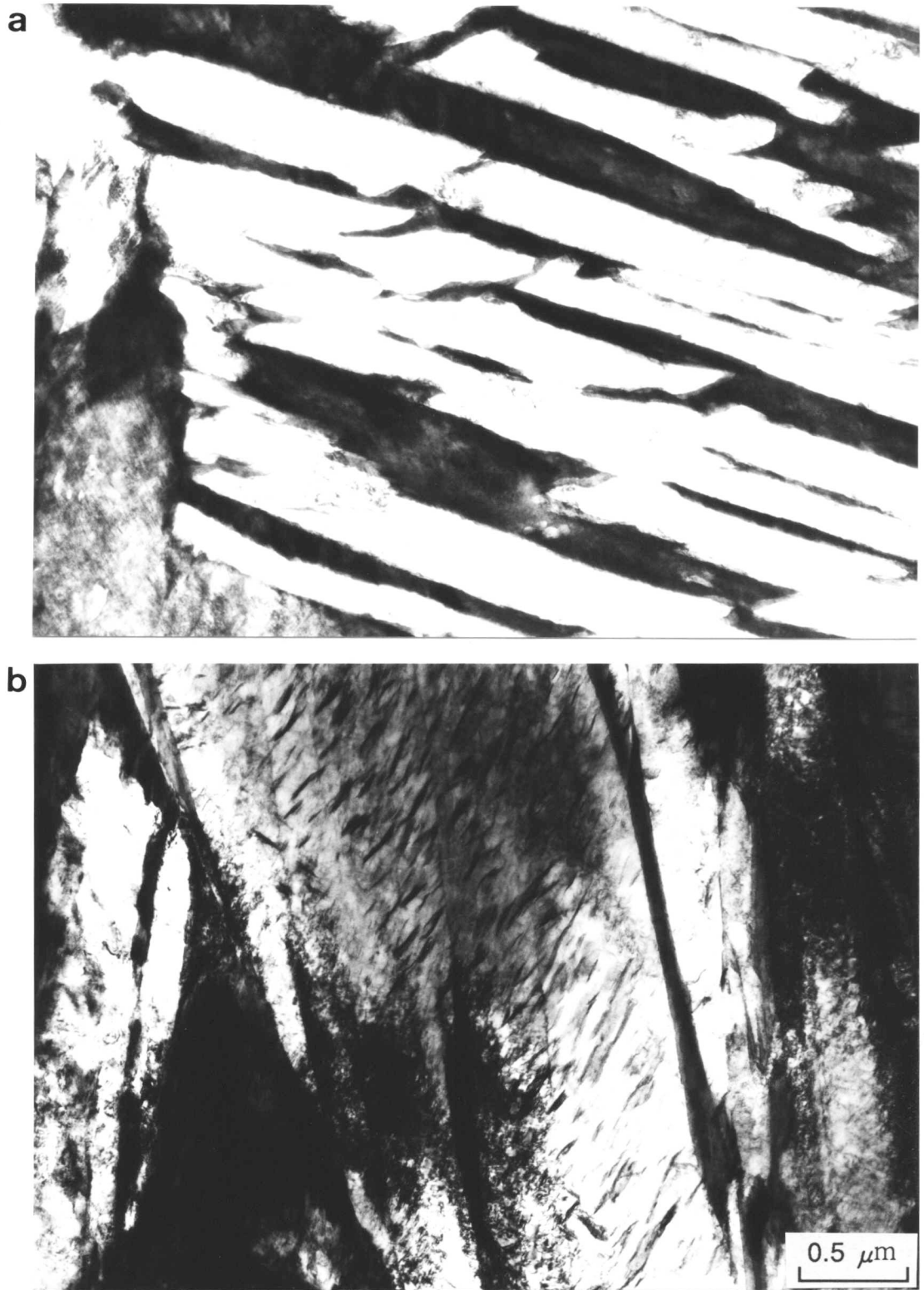


Fig. 4.12 Typical TEM micrographs of upper and lower bainite obtained in the Fe-0.43C-2.0Si-3.0Mn alloy at a) 350 °C and b) 270 °C respectively.

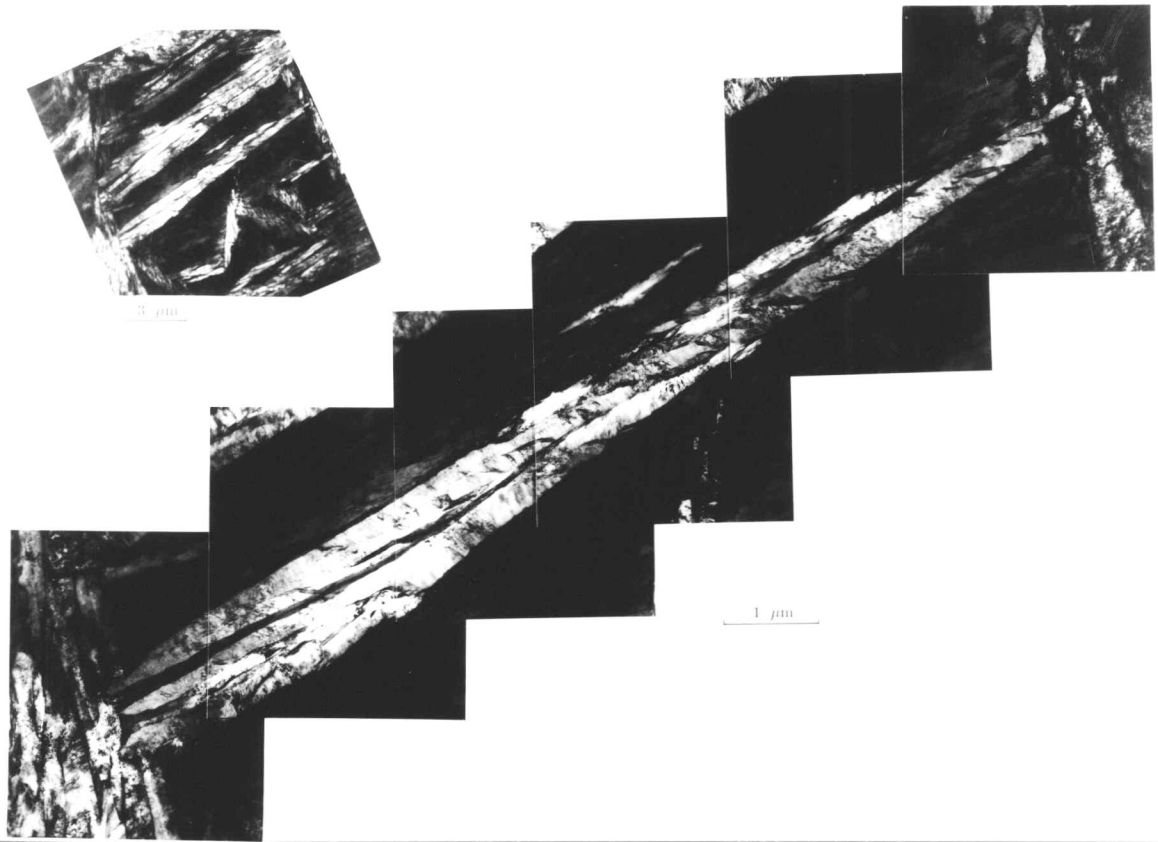


Fig. 4.13 TEM bright field image of upper bainite microstructure obtained at 350 °C in the Fe-0.43C-2.0Si-3.0Mn alloy.

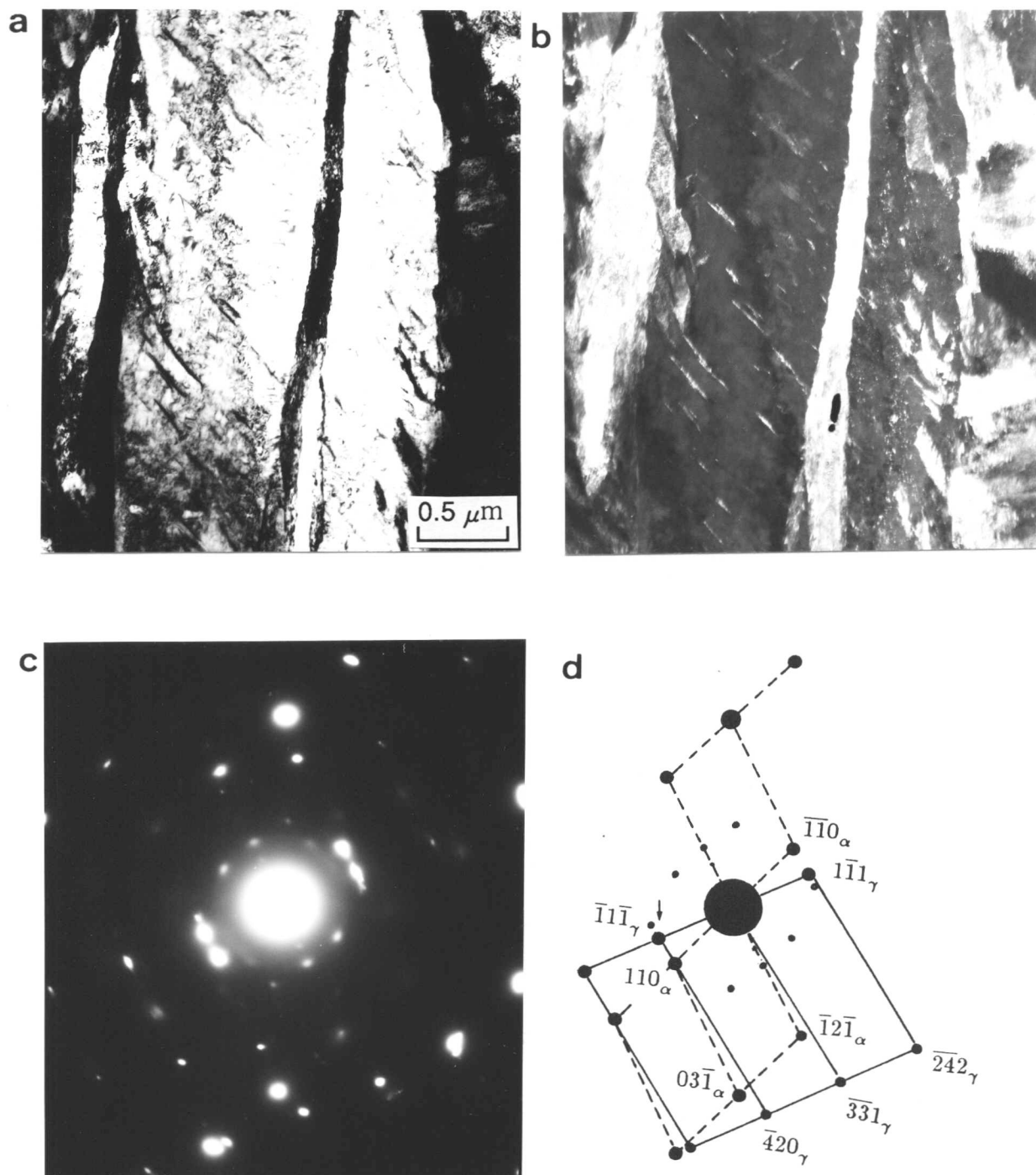
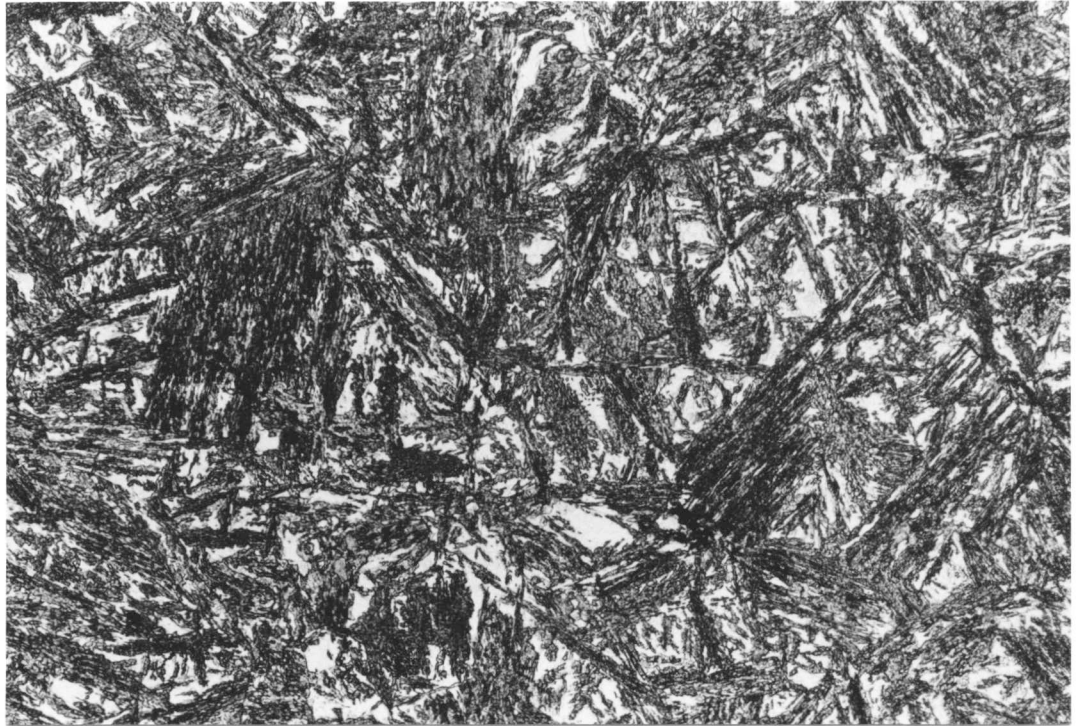


Fig. 4.14 (a) TEM bright field image of lower bainite obtained at 270 °C in the Fe-0.43C-2.0Si-3.0Mn alloy and (b) a dark field image of residual austenite trapped in between two adjacent bainitic ferrite plates. (c) is a selected area diffraction pattern.

a) Reaustenitised at 778 °C



b) Reaustenitised at 785 °C



Fig. 4.15 Optical micrographs of isothermally reaustenitised specimens at a) 778 °C, b) 785 °C, c) 790 °C and d) 805 °C.

c) Reaustenitised at 790 °C



d) Reaustenitised at 805 °C



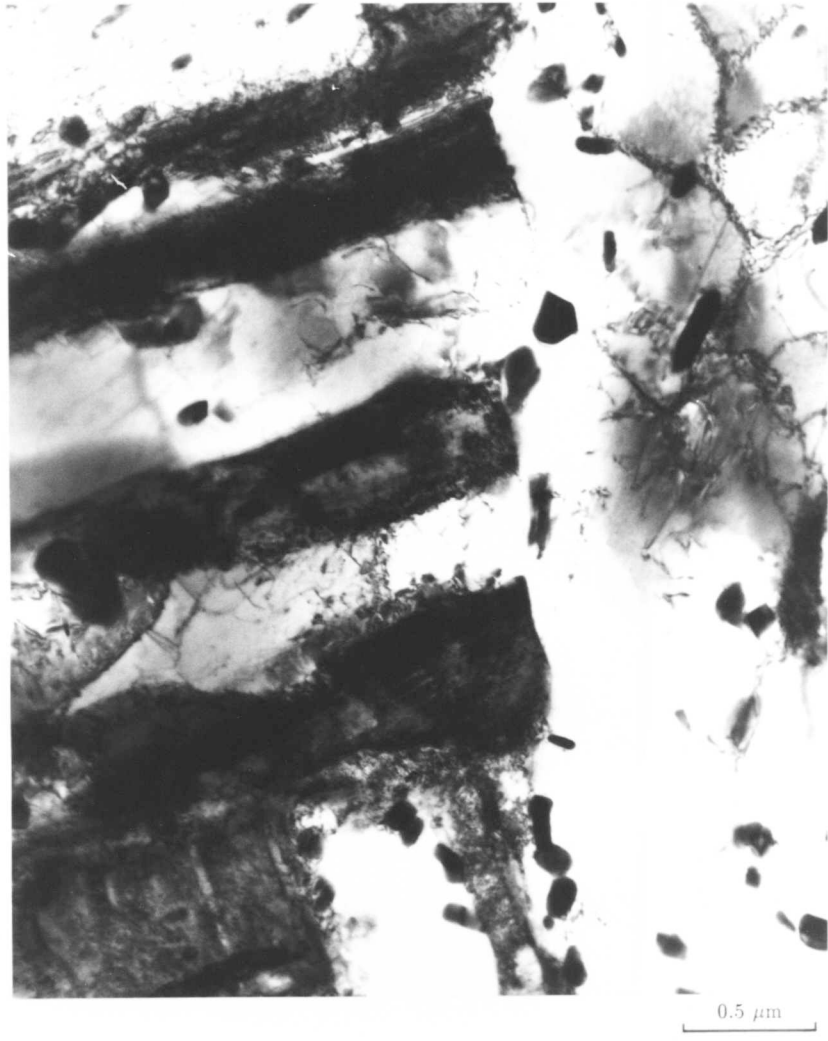


Fig. 4.16 TEM bright field image of a specimen quenched from 785 °C after 30 min of isothermal reaustenitisation at the temperature.

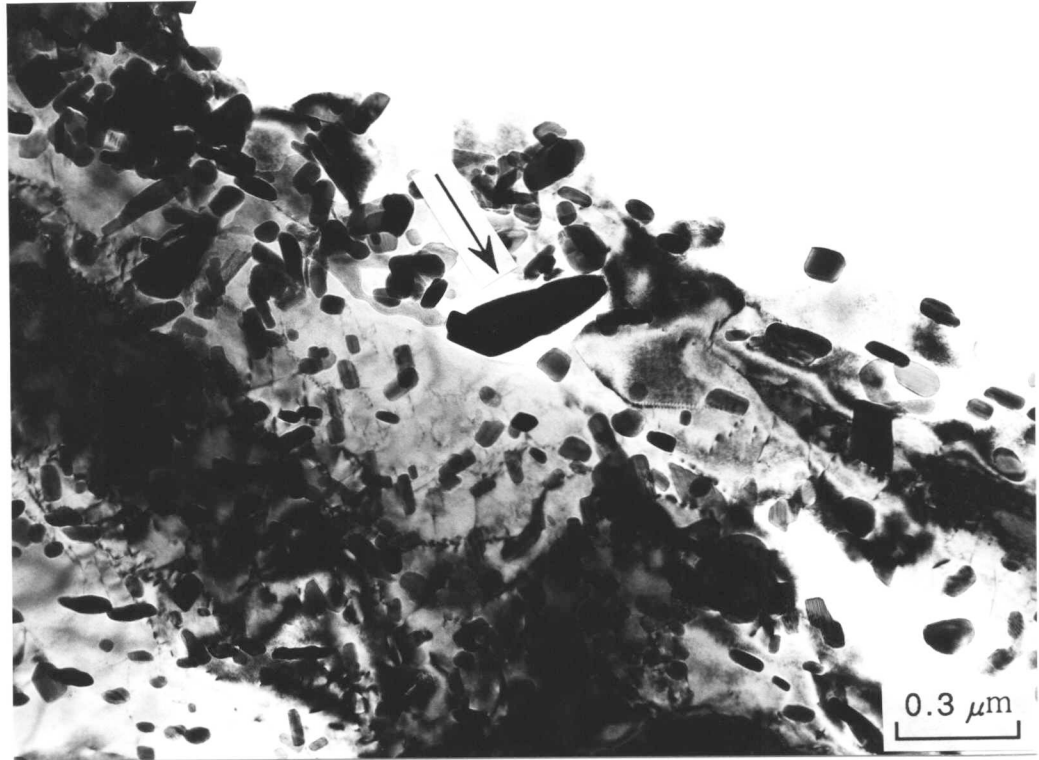


Fig. 4.17 TEM bright field image of precipitates with a selected area electron diffraction pattern and a convergent beam electron diffraction pattern of one of the particles.



Fig. 4.18 TEM bright field image of a specimen re-austenitised at 778 °C.



Fig. 4.19 TEM bright field image of a specimen re-austenitised at 778 °C.

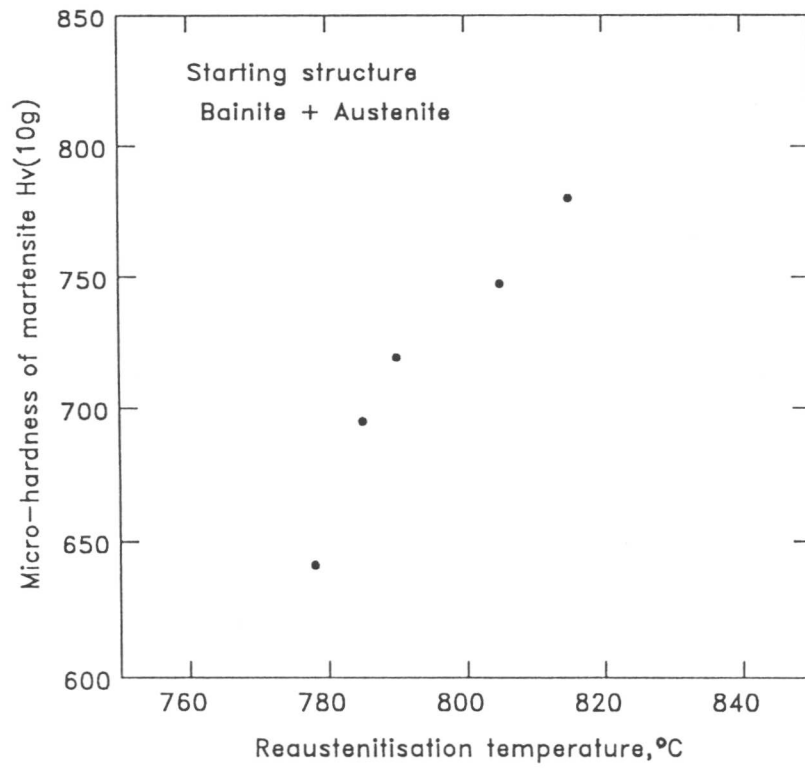


Fig. 4.20 Change in hardness of martensite with reaustenitisation temperature.

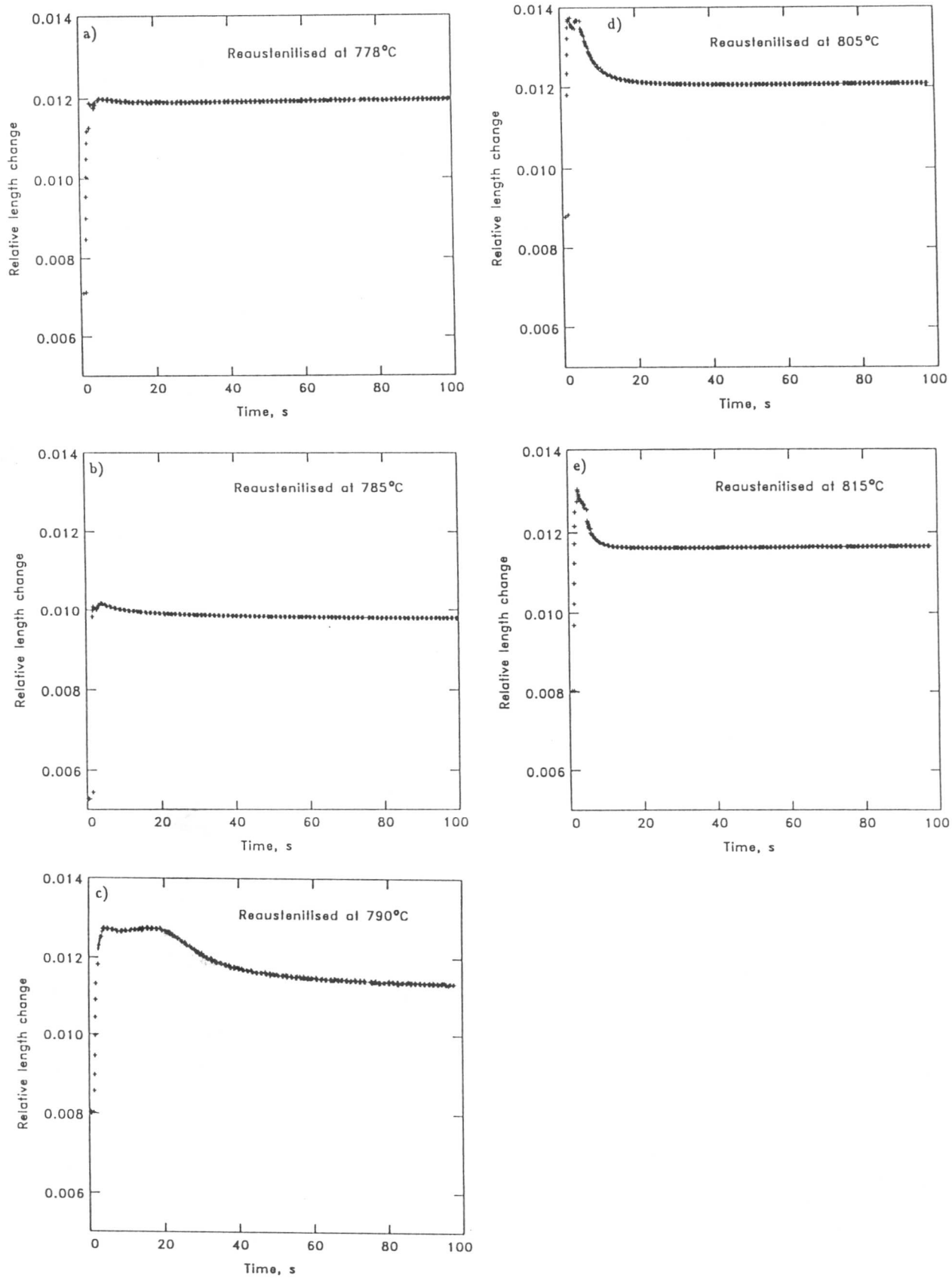


Fig. 4.21 Relative length changes during isothermal reustenitisation from a mixture of bainite and austenite at a) 778 °C, b) 785 °C, c) 790 °C, d) 805 °C and e) 815 °C.

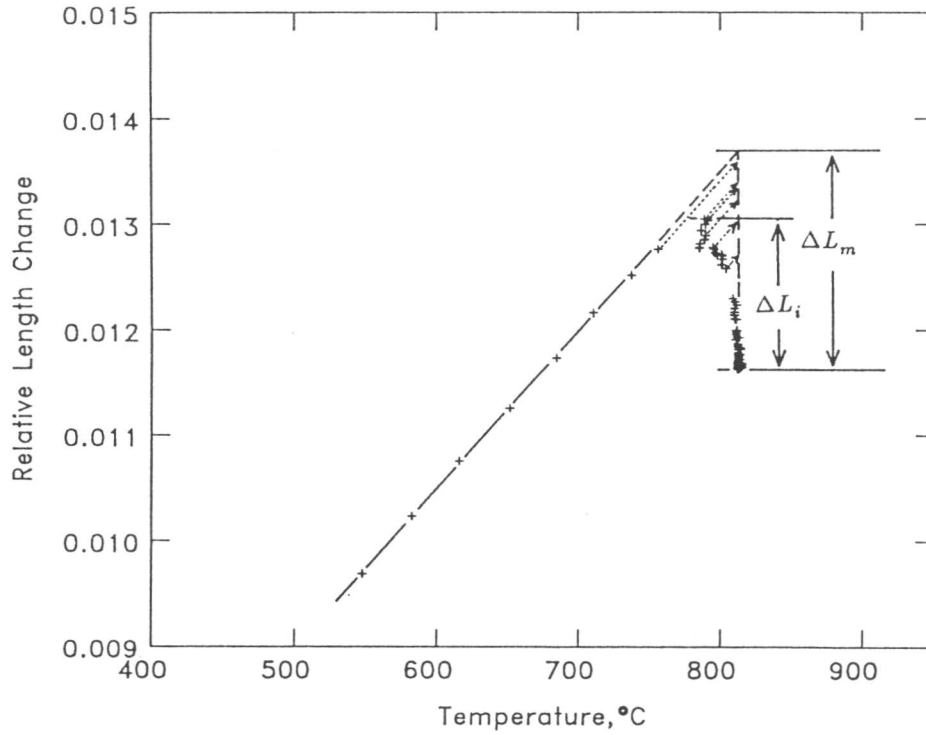


Fig. 4.22 Change in relative length during up-quenching and isothermal holding at 815 °C. A method of the temperature correction is illustrated in the figure.

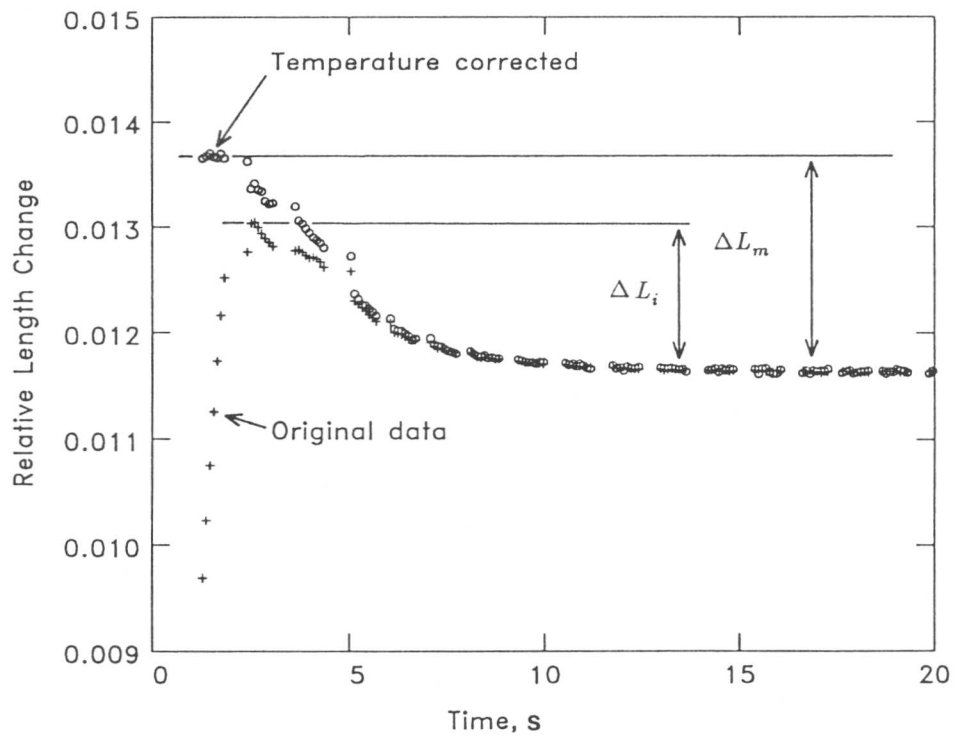


Fig. 4.23 Temperature corrected relative length change of the data in Fig. 4.22.

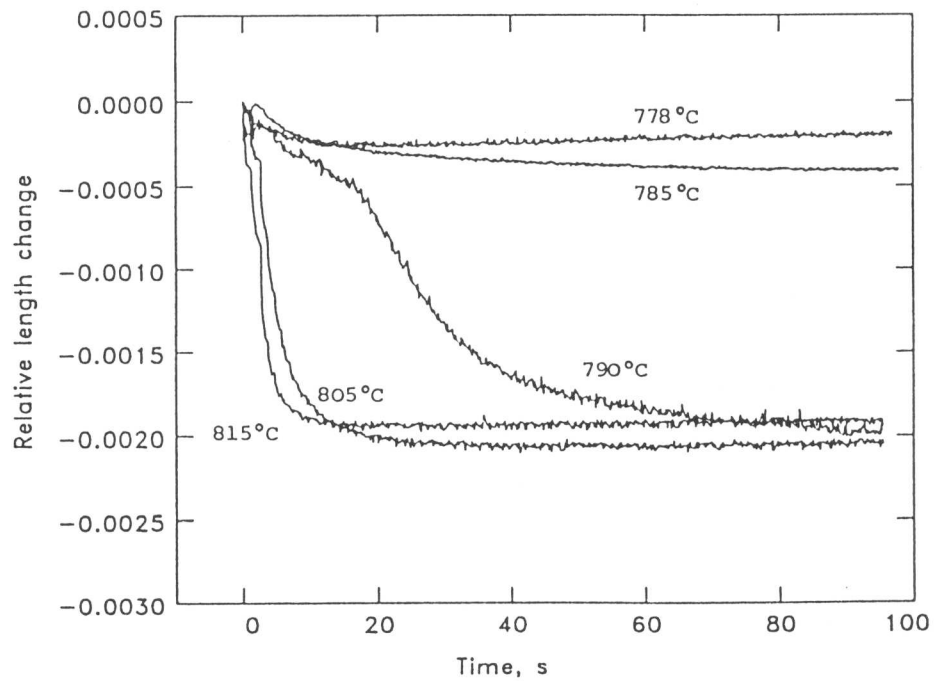


Fig. 4.24 Relative length changes during isothermal re-austenitisation from the mixture of bainite and austenite at different reaction temperatures.

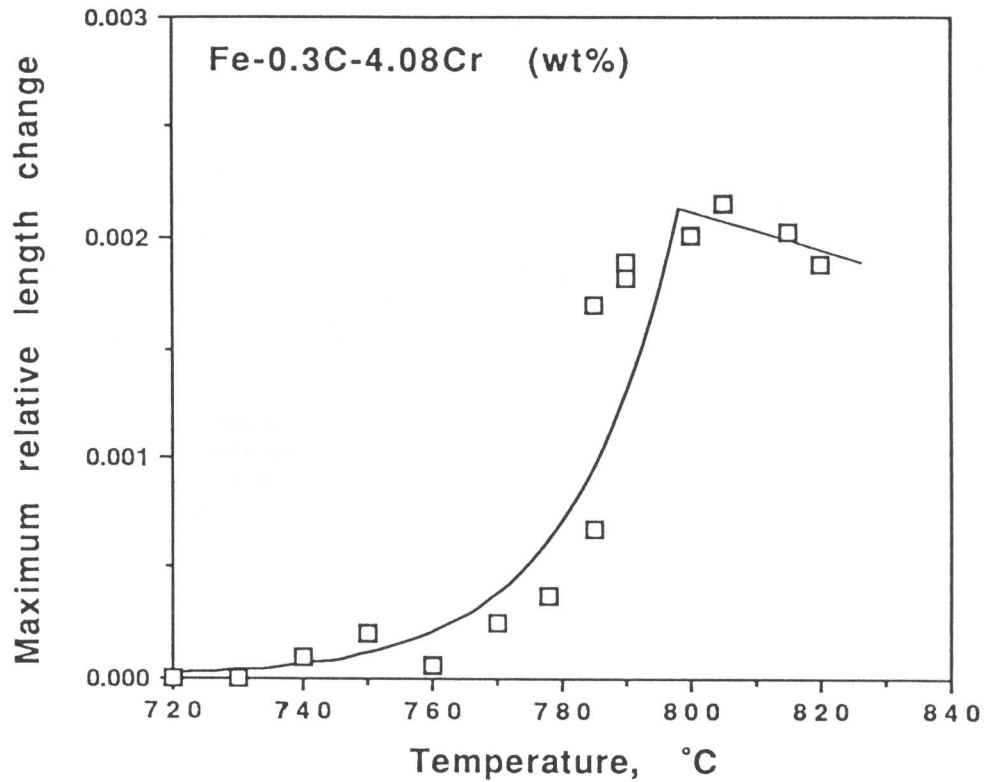


Fig. 4.25 Maximum relative length changes due to isothermal re-austenitisation from the mixture of bainite and austenite at different reaction temperatures.

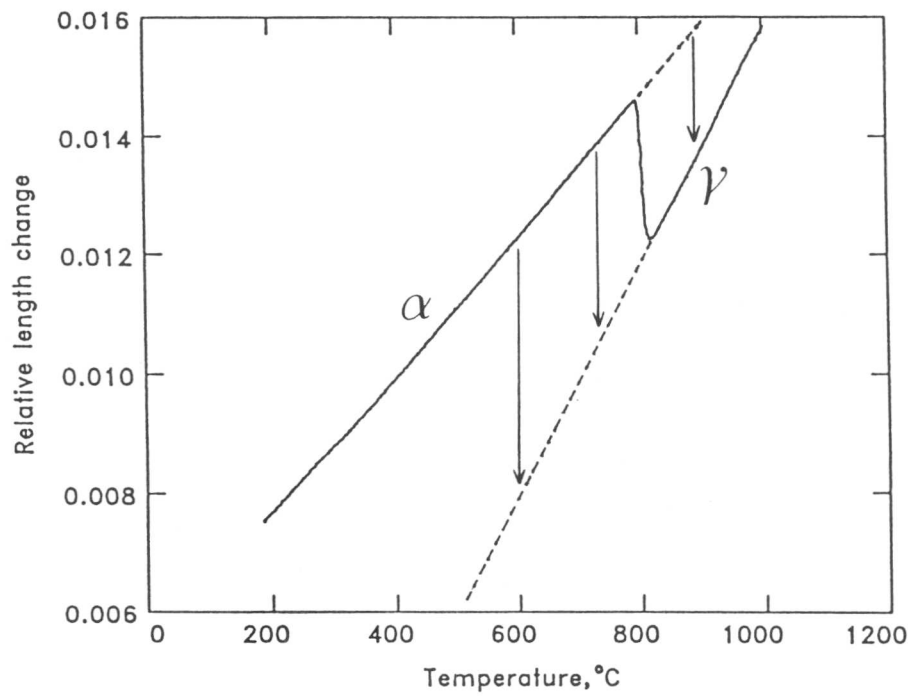


Fig. 4.26 Relative length change as a function of temperature during heating. Difference in thermal expansion coefficients of ferrite and austenite causes a change in the maximum relative length change due to 100 % of transformation.

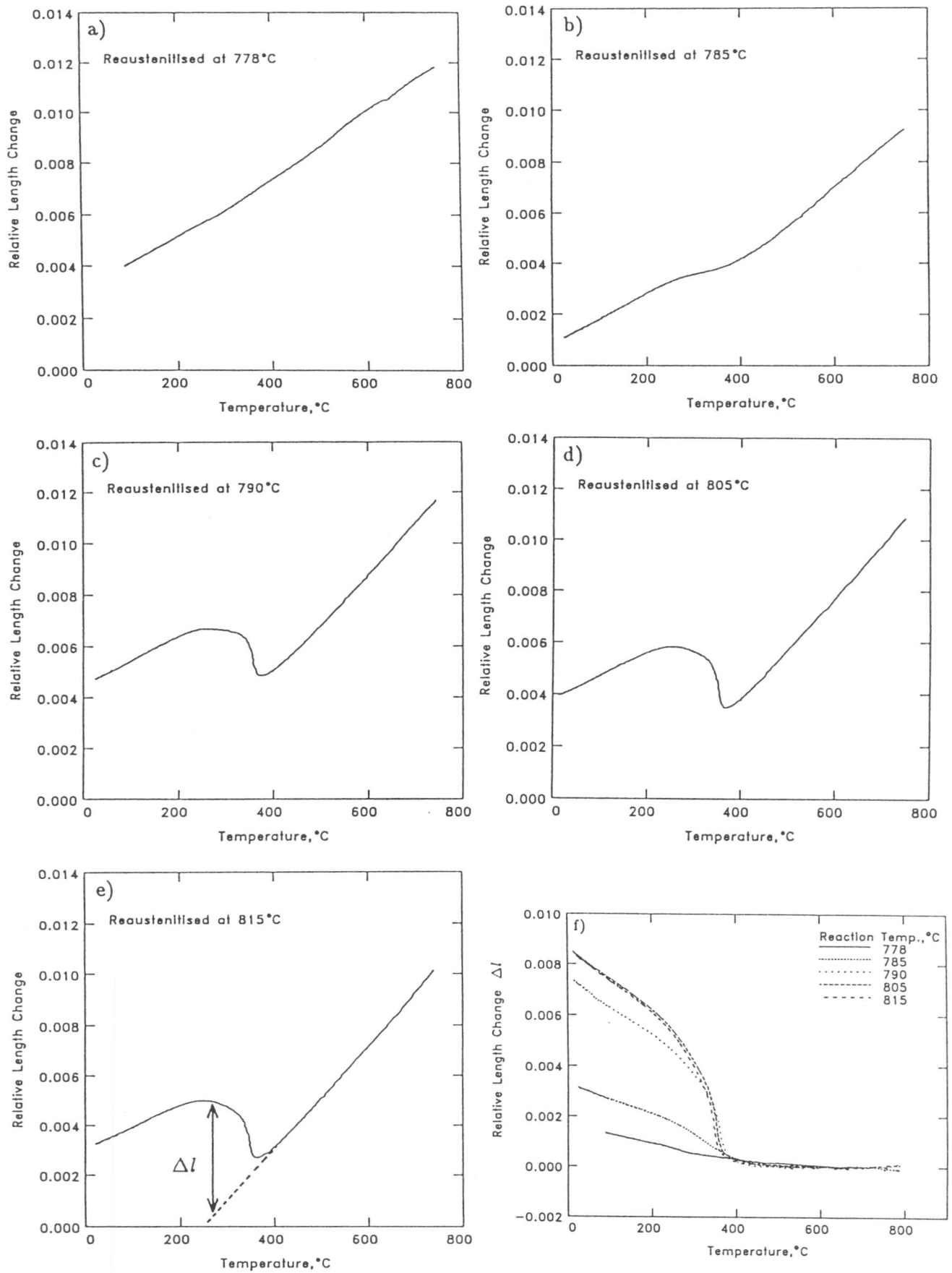


Fig. 4.27 Relative length changes during helium quenching after 30 min of isothermal re-austenitisation from the mixture of bainite and austenite at a) 778 °C, b) 785 °C, c) 790 °C d) 805 °C and e) 815 °C. Relative length changes  $\Delta l$  due to martensitic transformation are compared in f).

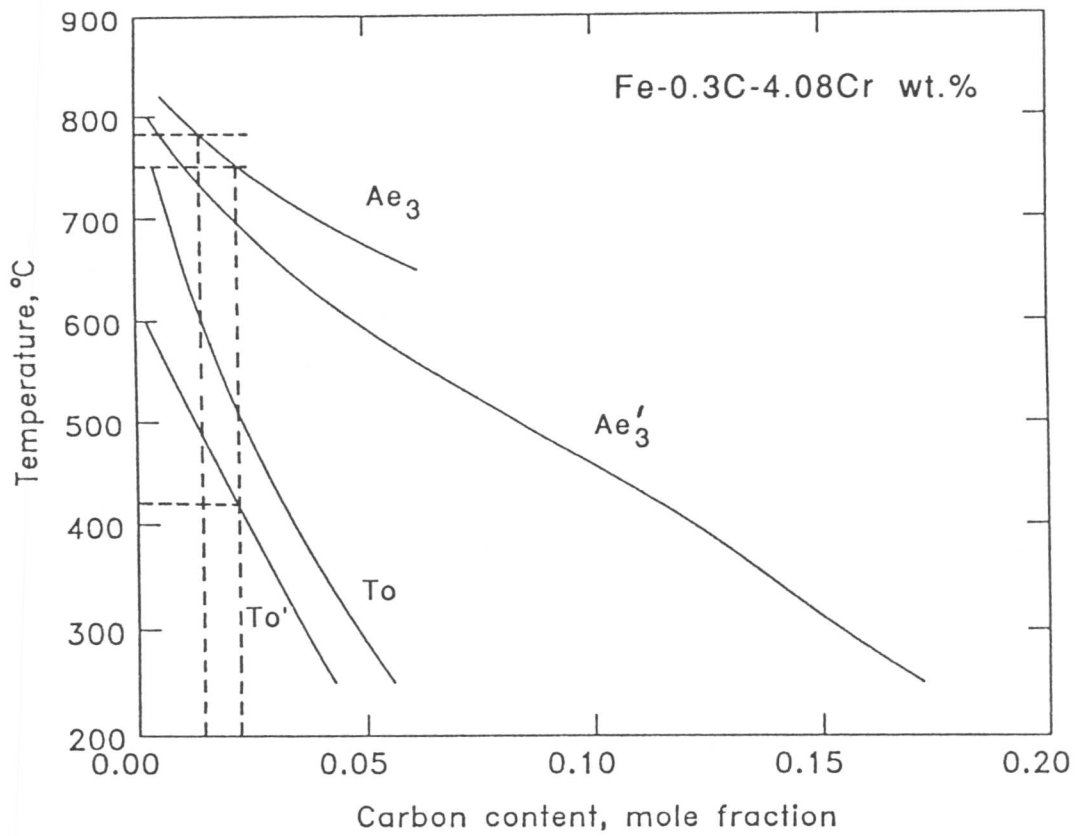


Fig. 4.28 Calculated phase diagram of the Fe-0.3C-4.08Cr alloy, which illustrates the partially re-austenitised temperature range.

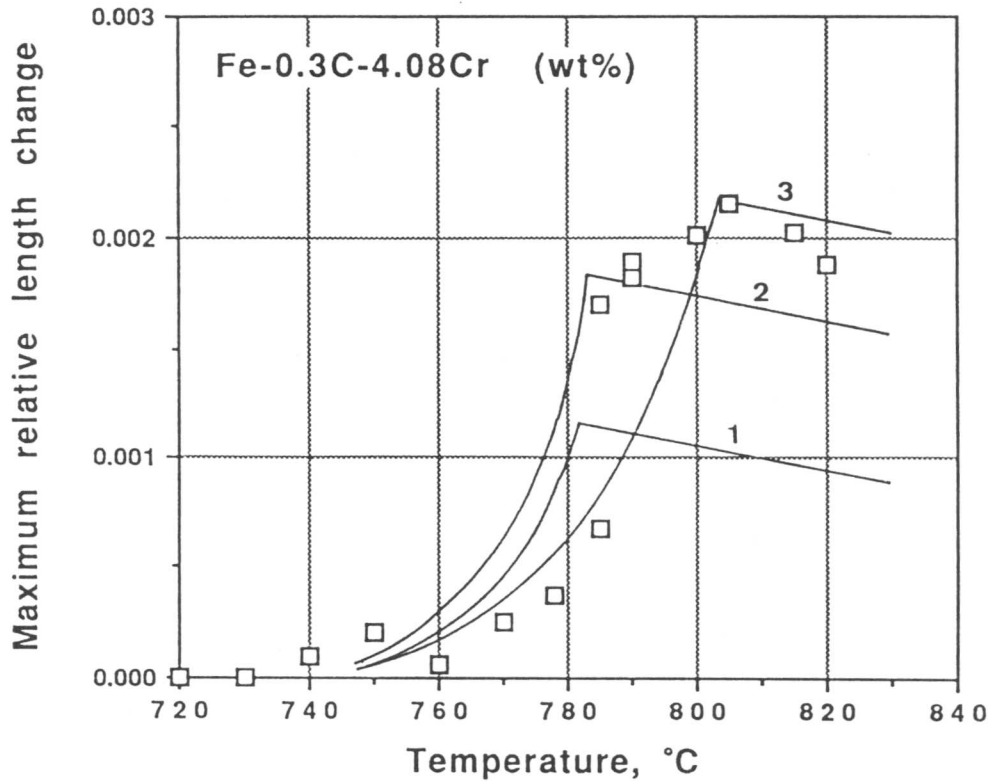


Fig. 4.29 Calculated maximum relative length changes for equilibrium isothermal re-austenitisation. Line 1 is calculated for case (1), line 2 for case (2) and line 3 for case (3). Plots are experimentally observed maximum relative length changes.

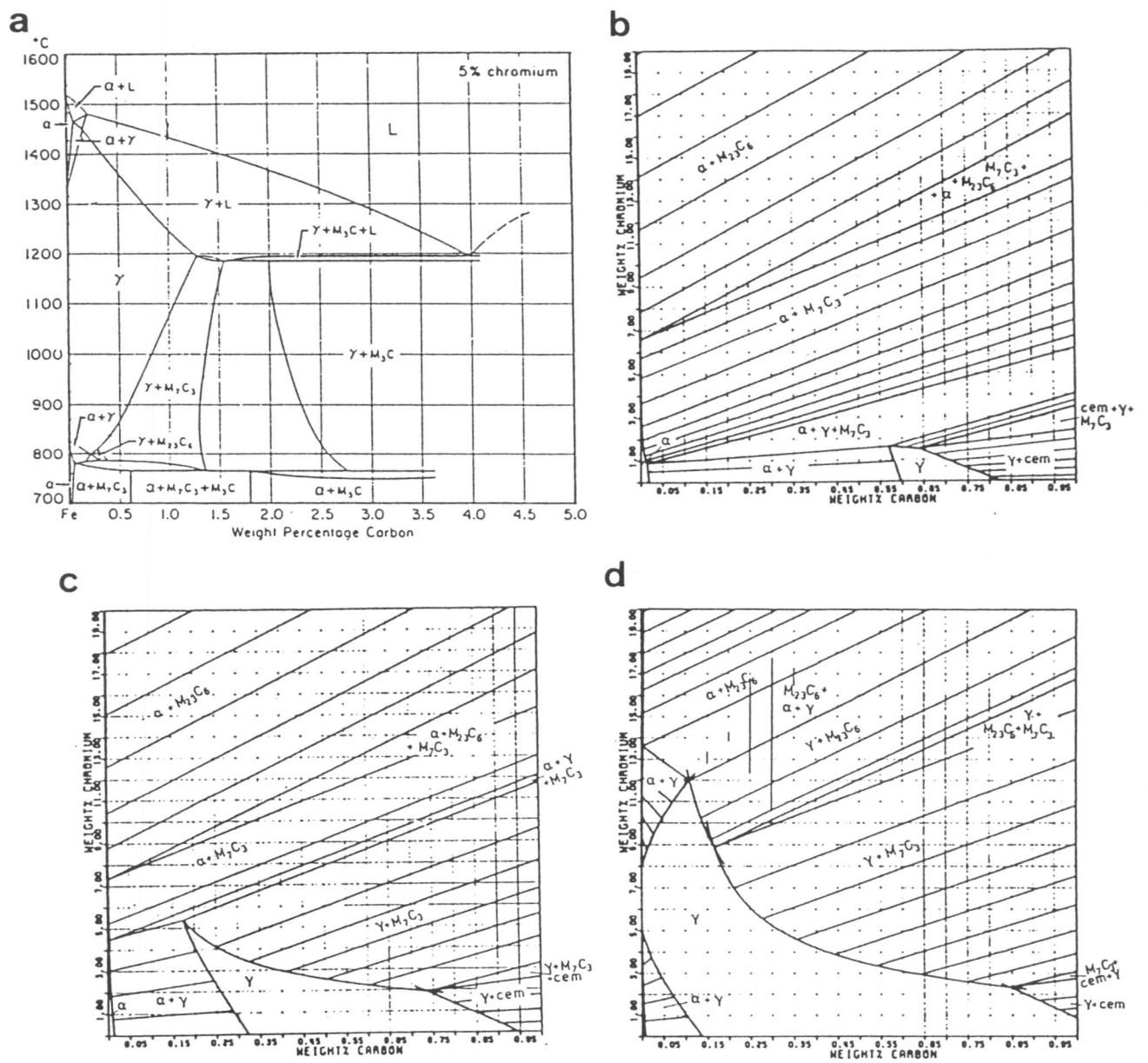


Fig. 4.30 (a) Equilibrium phase diagram of a Fe-5 wt.% Cr alloy (Metals Handbook) and calculated equilibrium phase diagrams for Fe-C-Cr ternary alloy at (b) 750 °C, (c) 800 °C and (d) 850 °C [18].

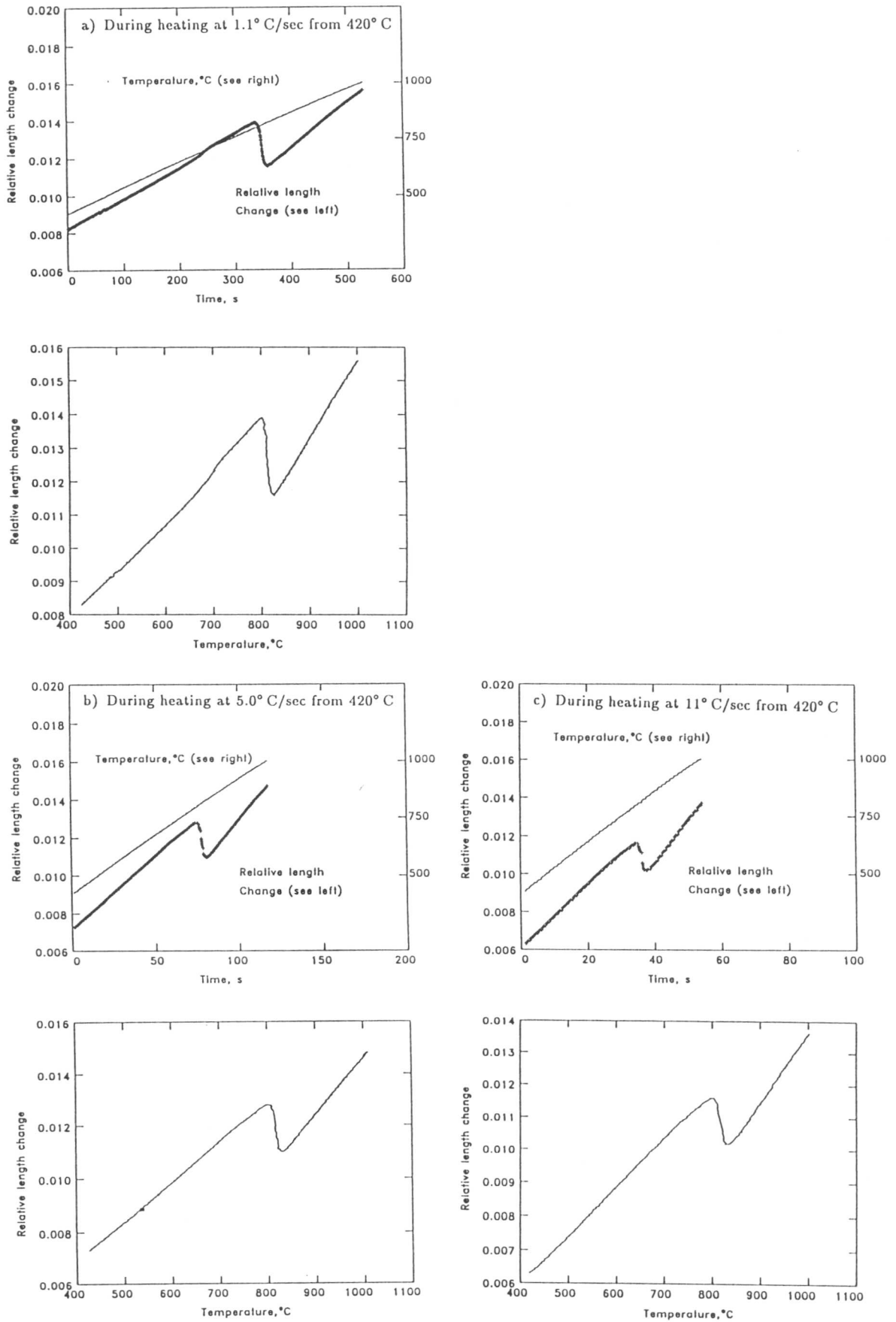


Fig. 4.31 Change in relative length and temperature during continuous heating re-austenitisation from the mixture of bainite and austenite at a)  $1.1\text{ }^{\circ}\text{C s}^{-1}$  from  $420\text{ }^{\circ}\text{C}$ , b)  $5.0\text{ }^{\circ}\text{C s}^{-1}$  from  $420\text{ }^{\circ}\text{C}$ , c)  $11\text{ }^{\circ}\text{C s}^{-1}$  from  $420\text{ }^{\circ}\text{C}$ , d)  $1.1\text{ }^{\circ}\text{C s}^{-1}$  from  $448\text{ }^{\circ}\text{C}$ , e)  $5.0\text{ }^{\circ}\text{C s}^{-1}$  from  $448\text{ }^{\circ}\text{C}$ , f)  $1.1\text{ }^{\circ}\text{C s}^{-1}$  from  $472\text{ }^{\circ}\text{C}$  and g)  $5.0\text{ }^{\circ}\text{C s}^{-1}$  from  $472\text{ }^{\circ}\text{C}$ .

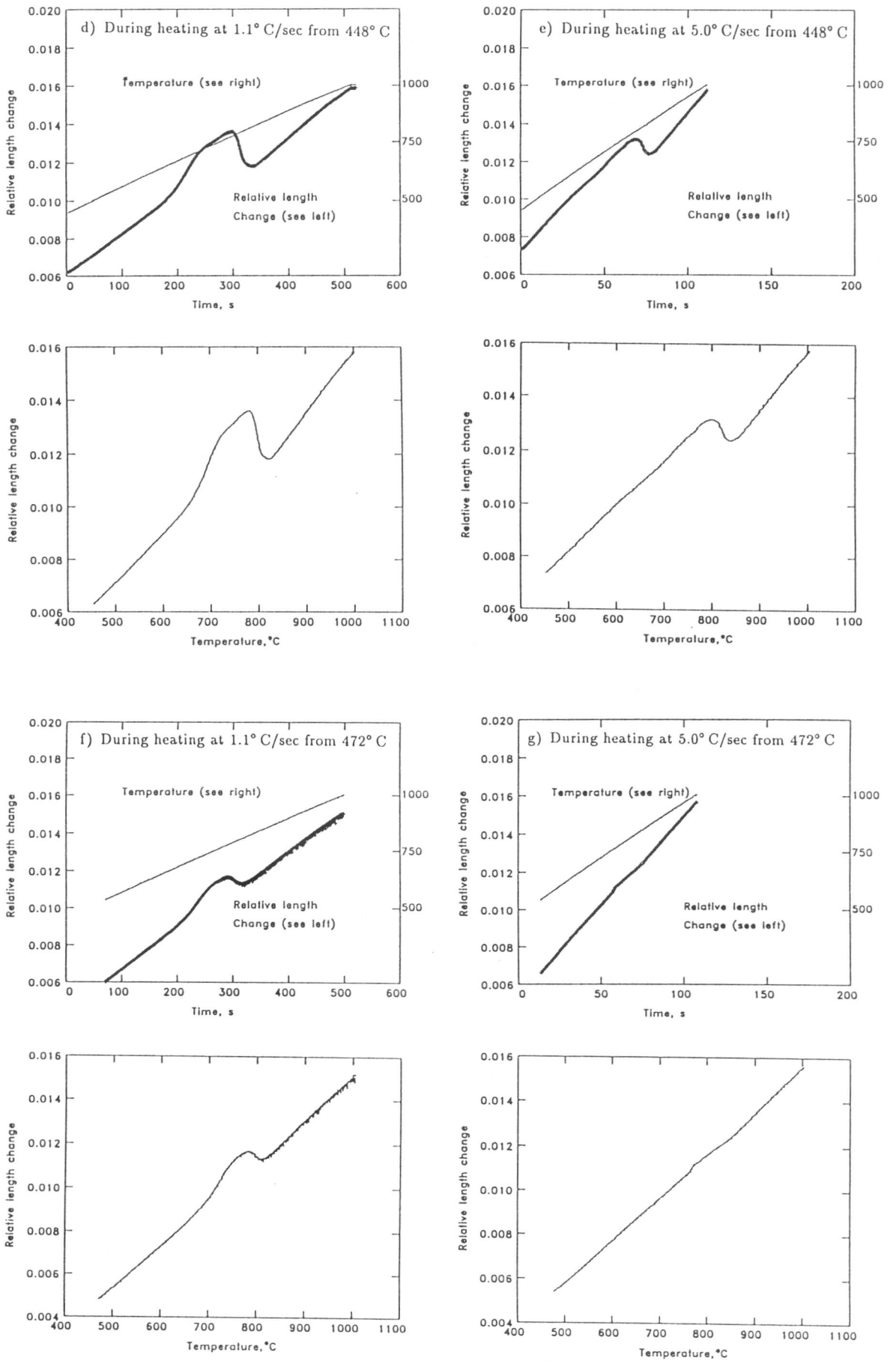


Fig. 4.31 (continued).

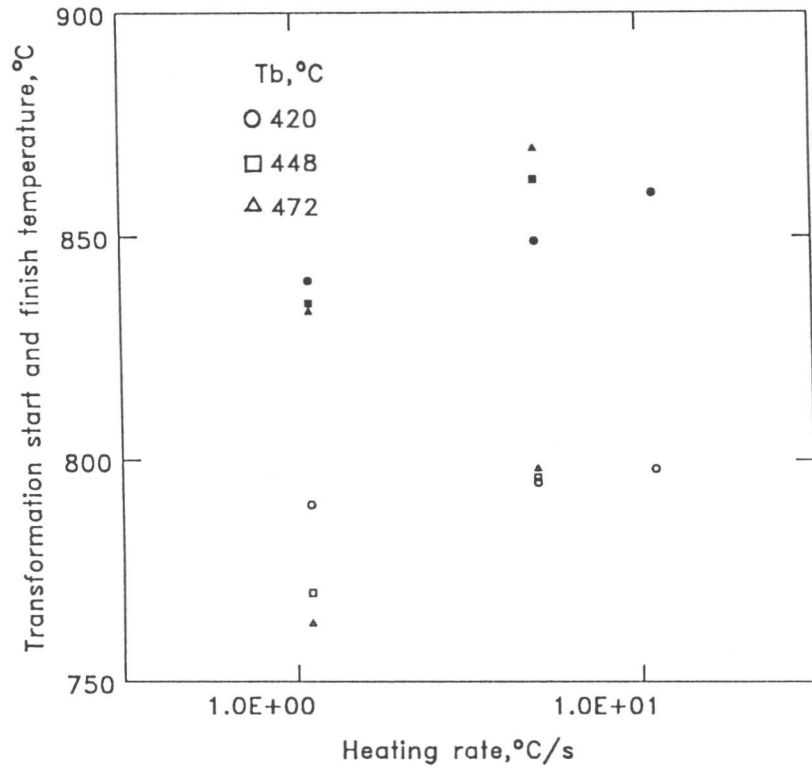


Fig. 4.32 Change in the thermal expansion coefficient of the initial microstructure of mixtures of bainite and austenite as a function of bainite transformation temperature.

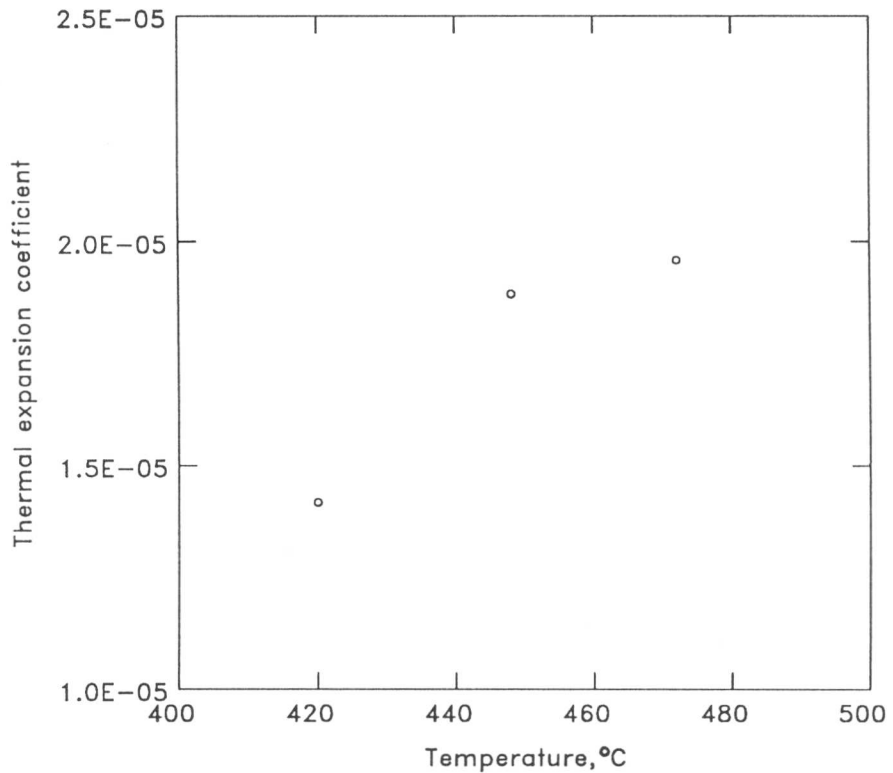


Fig. 4.33 Transformation-start (open) and -finish (solid) temperatures during continuous heating re-austenitisation from the mixtures of bainite and austenite obtained at  $T_b$ .

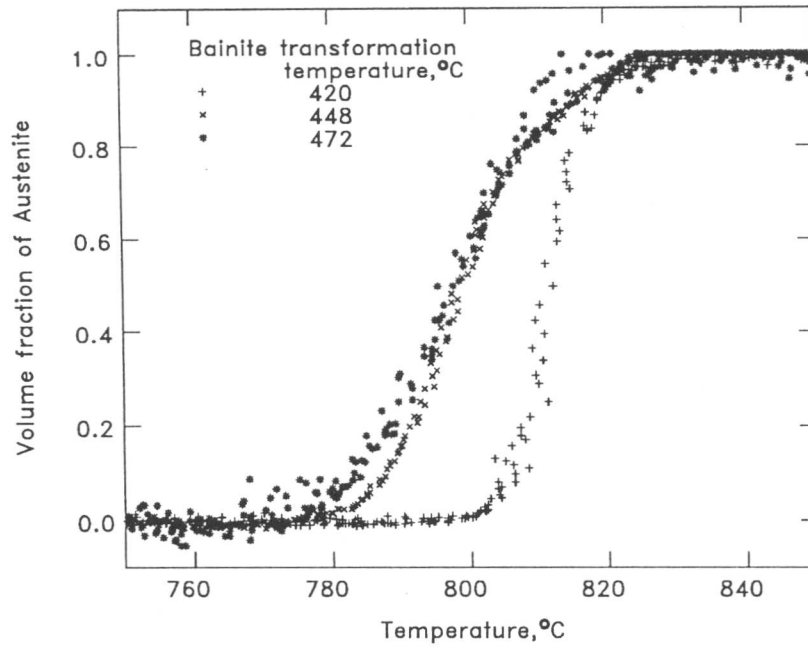


Fig. 4.34 Normalised volume fraction of austenite transformed on heating as a function of temperature.

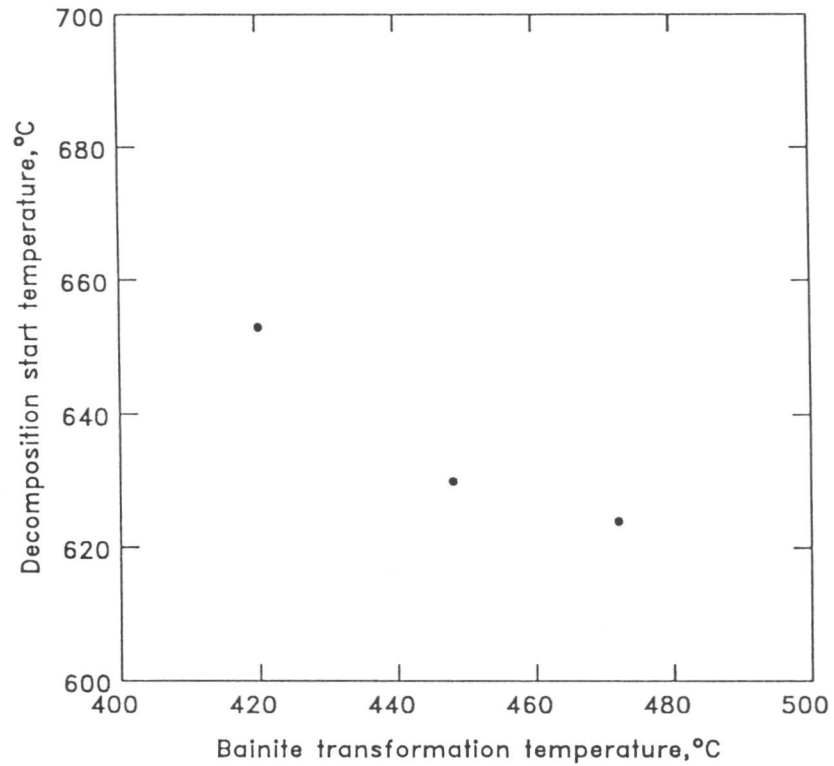


Fig. 4.35 Decomposition-start temperatures during continuous heating plotted against the bainite transformation temperature.

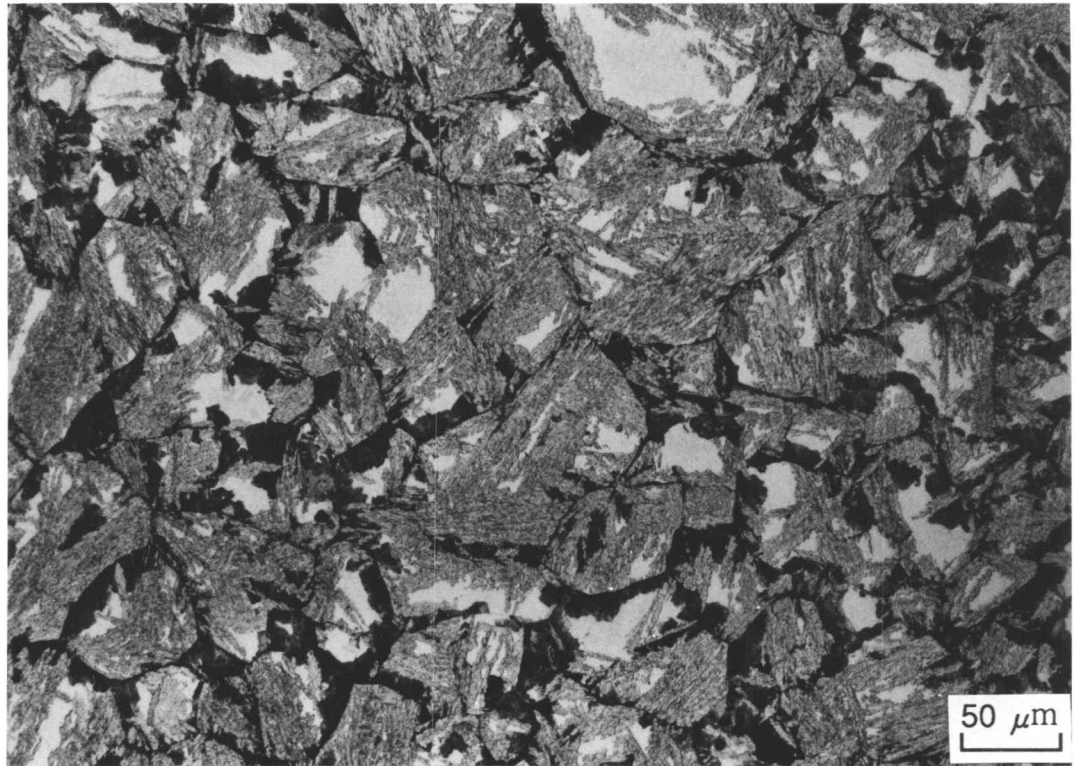


Fig. 4.36 Optical micrograph of a specimen helium quenched during the proceeding of decomposition of residual austenite on the way of the continuous heating reaustenitisation experiment at  $1.1\text{ }^{\circ}\text{C s}^{-1}$  after 30 min of isothermal bainite transformation treatment at  $445\text{ }^{\circ}\text{C}$ .



Fig. 4.37 TEM bright field image of the specimen in Fig. 4.36.

## CHAPTER 5

### PEARLITE TRANSFORMATION IN STEELS

#### 5.1 INTRODUCTION

The reconstructive formation of pearlite in steels is studied in this chapter. Since the bainite transformation stops before equilibrium is achieved, the untransformed austenite can decompose to ferrite and cementite by a reconstructive mechanism. This may happen during a prolonged isothermal holding at a bainite transformation temperature and during heating after bainitic transformation. The later case can be found, for example, in multirun welding where the successive deposition of weld metal heats up the underlying layers.

#### 5.2 DECOMPOSITION OF RESIDUAL AUSTENITE DURING HEATING

As discussed in the previous chapter, the austenite left untransformed after the completion of bainite transformation (*i.e.* residual austenite) decomposes to pearlite during slow heating. The decomposition-start temperature  $T_{ds}$  increases with the heating rate and no detectable decomposition of austenite occurs at higher heating rates (Fig. 5.1). The lower the bainite transformation temperature, the higher the decomposition-start temperature (Fig. 5.1).

An attempt to calculate the temperature  $T_{ds}$  at which the decomposition of residual austenite starts on heating, from an initial microstructure which is a mixture of bainitic ferrite and residual austenite, is made in this section.

The temperature  $T_{ds}$  for the reconstructive formation of ferrite from austenite on heating can be calculated by using the TTT curve for austenite which has the same chemical composition as the residual austenite. Scheil's rule may then be applicable for the calculation of the reconstructive formation of ferrite on heating, although there is no proof of that the reaction is isokinetic [1].

##### 5.2.1 TTT curve calculation of untransformed austenite

Bainite transformation ceases prematurely when the carbon concentration of the residual austenite reaches the  $T'_0$  curve ( $x_{T'_0}$ ), because the diffusionless formation of ferrite from austenite with its carbon content of more than  $x_{T'_0}$  at a reaction temperature will cause a positive free energy change, which is thermodynamically impossible. However, since the  $x_{T'_0}$  value is far less than the equilibrium carbon concentration of austenite, reconstructive transformations can occur even after the bainite reaction ceases. This decomposition may be expressed by the upper C-curve of the TTT diagram, which will be used here for the estimation of  $T_{ds}$ .

The calculation of TTT diagrams for the materials with different chemical compositions were carried out using a method reported by Bhadeshia [2]. He assumed an expression for incubation periods proposed by Russell [3], given by:

$$\tau \propto \frac{T}{(\Delta G_m^v)^p D} \quad (5.1)$$

where

$T$  : absolute temperature,

$D$  : an effective diffusion coefficient related to boundary or volume diffusion, depending on the coherency state of the nucleus concerned,

$\Delta G_m^v$  : the maximum volume free energy change accompanying the formation of a nucleus in a large amount of matrix phase,

$p$  : an exponent whose magnitude is a function of the nature of the nucleus. Russell [3] obtained  $p = 2$  for a coherent nucleus and  $p = 3$  for an incoherent one.

On substituting an Arrhenius expression for diffusion coefficients:

$$D \propto \exp(S_1/R) \exp(-Q_1/RT) \quad (5.2)$$

where  $S_1$  is the activation entropy for diffusion and  $Q_1$  is the activation enthalpy for diffusion. Bhadeshia [2] obtained the following relation:

$$\ln[(\Delta G_m)^p \tau/T] = Q_1/(RT) + C_{N1} \quad (5.3)$$

where  $\Delta G_m$  is the chemical free energy change accompanying the formation of one mole of nucleating phase in a large amount of matrix phase and  $C_{N1}$  is a constant. He then expressed  $Q_1$  and  $S_1$  as a function of temperature; *i.e.*  $Q_1 = Q_0 + C_{N2}(T - T')$  and  $S_1 = S_0 + C_{N3} \ln(T - T')$ , where  $S_0, Q_0, C_{N2}, C_{N3}$  and  $T'$  are constants, and finally obtained the following expression [2]:

$$\ln \left[ \frac{\tau(\Delta G_m)^p}{T^z} \right] = \frac{Q'}{RT} + C_{N4} \quad (5.4)$$

with constants  $z, Q'$  and  $C_{N4}$ . By maximizing the correlation coefficient when the equation is compared with experimentally observed TTT curves, Bhadeshia [2] obtained  $Q' = 0.2432 \times 10^{-6}$  J mol<sup>-1</sup>,  $C_{N4} = -0.0135$ ,  $p = 5$  and  $z = 20$  for shear transformation, and  $Q' = 0.6031 \times 10^{-6}$  J mol<sup>-1</sup>,  $C_{N4} = -0.01905$ ,  $p = 4$  and  $z = 20$  for diffusional transformation respectively. These values were used to calculate the transformation-start temperature of austenite during heating in the present work.

The carbon content of residual austenite  $x_1^\gamma\{T_b\}$  and the volume fraction of untransformed austenite  $V_\gamma$  have been calculated from the relative length change  $\Delta L/L$  during isothermal bainite transformation at each temperature  $T_b$  using equation 4.1, and the results are listed in Table 5.1. The calculated TTT curves for the austenite which has the carbon concentration identical to each values listed in Table 5.1 can be seen in Fig. 5.2. The incubation periods for both diffusional and displacive transformations become large with lowering the bainite transformation temperature. The lower the bainite transformation temperature, the lower the  $B_S$  and  $M_S$  temperatures of the austenite because of an increase in carbon concentration in the untransformed austenite.

$T_b, ^\circ\text{C}$	$\Delta L/L$	$x_1^\gamma\{T_b\}, \text{at.}\%$	$V_\gamma$
420	$3.86 \times 10^{-3}$	2.4	0.299
448	$1.76 \times 10^{-3}$	1.8	0.669
472	$2.90 \times 10^{-4}$	1.4	0.944

Table 5.1: Volume fractions and carbon contents of residual austenite in the initial microstructure

### 5.2.2 Kinetic calculation of decomposition-start temperature

A point on an upper C-curve representing the minimum detectable reconstructive formation of ferrite at a temperature  $T_i$  is now designated as an incubation period  $\tau\{T_i\}$ . When  $\Delta T$  refers to a small temperature step in a small time period  $\Delta t$ ,  $\frac{\Delta T}{\Delta t}$  gives a heating (or cooling) rate at a temperature. At a step between  $T_i$  to  $T_i + \Delta T$ , austenite spends a part of the incubation period ;

$$P_i = \frac{\Delta t}{\tau_i} \quad (5.5)$$

with

$$\tau_i = \frac{1}{2}(\tau\{T_i\} + \tau\{T_i + \Delta T\}).$$

When the summation of  $P_i$  becomes unity, the transformation is assumed to start. In order to calculate the position where the austenite is on the TTT diagram during heating after the completion of bainite transformation, the following equation is used (Fig. 5.3).

$$t_i\{T\} = \tau_i \sum_i P_i \quad (5.6)$$

where

$T : T_i + \frac{1}{2}\Delta T_i$   
 $t_i\{T\}$  : instantaneous time on the TTT diagram at a temperature  $T$  on heating.

The calculations were carried out for continuous heating at constant rates between 0.01 and 10 °C s<sup>-1</sup>, for three materials whose carbon contents are identical to the residual austenite left untransformed after the cessation of the bainite transformation at 420, 448 and 472 °C in the Fe-0.3C-4.08Cr wt.% alloy respectively (Fig. 5.4). Since the formation of bainitic ferrite is thermodynamically impossible above the temperature at which the bainite treatment was conducted, and since the incubation period of reconstructive formation of ferrite at temperatures below the  $B_S$  temperature is usually extremely large, the calculation was started from the  $B_S$  temperature. In Fig. 5.5, the transformation-start temperatures for each material are drawn with the  $T_{ds}$  temperatures obtained in the present experiments. Each calculated transformation-start curve corresponding to the different carbon content increases linearly with heating rate at low heating rates, and rapidly increases at higher heating rates, reaching to the  $Ae'_3$  temperature; above this heating rate, transformation is not expected to occur during heating. Although the calculation treats the austenite in isolation (*i.e.* ignore the presence of the bainitic ferrite), rather good agreement was obtained with experimental results (Fig. 5.5). The fact that almost no decomposition has been observed in the cases of the heating at more than 5 °C s<sup>-1</sup> is also explained as the austenite can be heated up above the  $Ae'_3$  temperature without meeting the diffusional C-curve on heating (Fig. 5.5).

The fact that the change in the decomposition-start temperature of austenite during continuous heating can be understood by using the  $T_0$  concept, is further evidence in support of the incomplete reaction phenomenon.

### 5.3 FORMATION OF PEARLITE BELOW THE $B_S$ TEMPERATURE

Pearlite formation at very low temperatures may become important under circumstances where austenite is held at low temperatures for an extended period of time without being cooled

below the  $M_S$  temperature of the alloy. This may occur, for example, in the heat affected zone of a multirun weld or in the very slow cooling of hot rolled steel strip after coiling.

Bhadeshia [4,5] reported a diffusional perturbation of the interface between bainitic ferrite and residual austenite in the Fe-0.3C-4.08Cr wt.% alloy after an extended period of isothermal holding at 478 °C, just below the  $B_S$  temperature 492 °C of the alloy. The growth rate of the perturbation of the interface was found to be far slower than the calculated growth rate of ferrite controlled by the carbon diffusion [5]. Although bainite transformation ceases when the carbon concentration in residual austenite becomes  $x_{T'_0}$ , reconstructive transformation to ferrite is still possible since  $x_{T'_0}$  is far smaller than the equilibrium carbon concentration of the austenite. A relative length change due to bainite transformation at 472 °C; which is very close to the reaction temperature used by Bhadeshia [5], in the Fe-0.3C-4.08Cr wt.% alloy can be seen in Fig. 4.3, showing that the bainite transformation completed within about 30 min of isothermal holding at the temperature.

Specimens with the identical alloy chemistry as [5] were heated to 1100 °C in a furnace and transferred to a different furnace at 478 °C. The specimens were then quenched into water after 300, 600, 241200 (67 hours), 576000 (160 hours), 1987200 (23 days), and 3715200 (43 days) seconds. The volume fraction of bainite increases with time and seems to remain constant beyond 30 min [5] as it can be seen in optical micrographs (Fig. 5.6). After 160 hours of isothermal holding, the formation of a new phase can be found at the austenite grain boundaries (Fig. 5.6). The new phase then grows into one of the austenite grains separated by the grain boundaries at which the nucleation takes place. From a TEM micrograph, one can see a lamellar structure of carbide and ferrite (Fig. 5.7). The structure and the temperature of the transformation suggest that the new phase is pearlite nucleated at the austenite grain boundaries.

The calculated upper C-curve which corresponds to reconstructive formation of austenite, was extrapolated to temperatures lower than the  $B_S$  temperature of the alloy. The extrapolated C-curve shows the time required to obtain the minimum detectable amount of reconstructive ferrite is about 150 hours, close to the value observed optically in the present work. This may mean that the austenite after the completion of bainite transformation behaves like an isolated austenite for reconstructive formation of ferrite.

The maximum thickness of pearlite at each holding time were measured and plotted in Fig. 5.8, giving the growth rate of pearlite in the alloy at 478 °C equal to about  $1.0 \times 10^{-9}$  cm s<sup>-1</sup>.

#### 5.4 GROWTH RATE OF PEARLITE

The pearlite discussed above seems to consist of a mixture of alloy carbide ( $M_7C_3$ ) and ferrite as mentioned by Bhadeshia [5]. However, it is established that the formation of conventional pearlite can form at a temperature below the  $B_S$  temperature after the completion of bainite transformation [6]. Therefore it is important to investigate the formation of pearlite at very low temperatures as well as at temperatures close to the  $Ae_1$  temperature. In this section, the growth theories of conventional pearlite which have been published so far are studied.

The formation of pearlite is expected to occur when austenite is cooled to temperatures at which both ferrite and cementite are thermodynamically stable. Pearlite is a lamellar mixture of iron and iron carbide which is very common constituent of a wide variety of steels contributing substantially to strength. As a result, it has been investigated intensively so far. The kinetics of pearlite transformation have been reviewed recently (for example [7,8]).

Pearlite transformation in steels is reconstructive and known to show a constant growth rate because the composition of untransformed matrix remains unchanged except near the transformation front [1]. The growth rate of pearlite is believed to be controlled by either volume diffusion of carbon [9,10] or by boundary diffusion of substitutional alloying element [11-13]. The two growth theories are summarized as follows.

When the growth rate of pearlite is controlled by the bulk diffusion of atoms in austenite ahead of the interface, the diffusion of carbon may play a more important role than that of substitutional alloying elements, since the diffusivity of the substitutional alloying elements in austenite is far smaller than that of carbon. As a result, the substitutional alloying elements may not diffuse a long distance during the reaction. Therefore the equilibrium condition which is maintained at the interface between austenite and pearlite may be either the negligible partitioning local equilibrium (NPLE) or paraequilibrium (PE). The growth rate of pearlite is expressed as follows [10]:

$$v_V = \frac{D}{g} \frac{s^2}{s_\alpha s_\theta} \frac{x_1^{\gamma\alpha} - x_1^{\gamma\theta}}{x_1^{\theta\gamma} - x_1^{\alpha\gamma}} \frac{1}{s} \left[1 - \frac{s_C}{s}\right] \quad (5.7)$$

where

- $v_V$  : volume diffusion controlled growth rate of pearlite,
- $D$  : volume diffusion coefficient for carbon in austenite,
- $g$  : geometric factor equal to 0.72 in plain carbon steels,
- $x_1^{\gamma\alpha}$  : carbon concentration at the  $\gamma/\alpha$  interface in  $\gamma$ , under either local equilibrium or paraequilibrium with  $\alpha$ ,
- $x_1^{\gamma\theta}$  : carbon concentration at the  $\gamma/\theta$  interface in  $\gamma$ , under either local equilibrium or paraequilibrium with  $\theta$ ,
- $x_1^{\theta\gamma}$  : carbon concentration at the  $\theta/\gamma$  interface in  $\theta$ , under either local equilibrium or paraequilibrium with  $\gamma$ ,
- $x_1^{\alpha\gamma}$  : carbon concentration at the  $\alpha/\gamma$  interface in  $\alpha$ , under either local equilibrium or paraequilibrium with  $\gamma$ ,
- $s$  : interlamellar spacing,
- $s_C$  : critical spacing at which the growth rate becomes zero,
- $s_\alpha, s_\theta$  : respective thickness of ferrite and cementite lamellar.

with the maximum velocity criterion, the relation between  $s$  and  $s_C$  can be obtained by setting the first derivative of equation (5.7) equal to zero, which leads to [9],

$$s = 2s_C \quad (5.8)$$

where

$$s_C = \frac{2\sigma_{\alpha\theta}T_E}{\Delta H\delta T} \quad (5.9)$$

with

- $\sigma_{\alpha\theta}$  : surface energy of ferrite/cementite interface,
- $\Delta H$  : change in enthalpy between the parent and product phases,
- $T_E$  : eutectoid temperature,
- $\delta T$  : undercooling below the eutectoid temperature.

The critical spacing  $s_C$  can be compared to observed interlamellar spacing assuming the relation (5.8). Interlamellar spacings in Fe-C, Fe-C-Cr, Fe-Ni and Fe-C-Mn alloys [8,15-17] were used to obtain an empirical expression for the interlamellar spacing as a function of the temperature and the alloy contents. Using the data (Table 5.2), the following relation was obtained for Fe-C, Fe-C-Mn, Fe-C-Ni and Fe-C-Cr steels.

$$\log\{s\} = -2.2358 + 0.09863 \times \text{Mn} - 0.05427 \times \text{Cr} + 0.03367 \times \text{Ni} - \log\left\{\frac{T_E - T}{T_E}\right\} \quad (5.10)$$

where  $s$  is measured in  $\mu\text{m}$  and Mn, Cr and Ni in wt.%. It is noted that an addition of Cr or Ni decreases the interlamellar spacing as it is observed in many other alloys, whereas a Mn addition causes an increase in the lamellar spacing. A comparison between observed and calculated interlamellar spacing can be seen in Fig. 5.9. The expression for the interlamellar spacing was applied to a material which contains both Mn and Cr. The observed and calculated interlamellar spacing of Fe-1.02Mn-1.05Cr wt.% alloy [18] are plotted in Fig. 5.10. The expression of interlamellar spacing obtained in the present work seems to represent experimental results very well even in alloys which contain both Mn and Cr.

Comparing equations (5.9) and (5.10) assuming the relation (5.8), the following relation should be maintained.

$$\log\left\{\frac{4\sigma_{\alpha\theta}}{\Delta H}\right\} = -2.2358 + 0.09863 \times \text{Mn} - 0.05427 \times \text{Cr} + 0.03367 \times \text{Ni}$$

If coefficients reported by Puls and Kirkaldy [7] are adopted, the left hand side becomes  $-2.404$  in plain carbon steels which is very close to the value  $-2.236$  obtained in the present analysis.

$$\begin{aligned} \Delta H &= 6.09 \times 10^9 \text{ erg cm}^{-3} \\ \sigma_{\alpha\theta} &= 600 \text{ erg cm}^{-2} \\ T_E &= 1000 \text{ K} \end{aligned}$$

It is, however, worth noting that using a more advanced theory proposed by Hashiguchi and Kirkaldy [19], the ratio  $s/s_C$  varies between 1 and 2.

When the partitioning of the substitutional alloying elements is substantial during the growth event of pearlite, boundary diffusion of the alloying elements may control the growth rate of pearlite, since the boundary diffusivity of the substitutional alloying elements may become comparable to the bulk diffusivity of carbon in austenite, and, as a result, a long range diffusion of the substitutional alloying elements may become possible during the reaction. The growth rate, in the case, is expressed as follows [13].

$$v_B = 12KD_B\delta \frac{s^2}{s_\alpha s_\theta} \frac{(x_2^{\gamma\alpha} - x_2^{\gamma\theta})}{\bar{x}_2} \frac{1}{s^2} \left(1 - \frac{s_C}{s}\right) \quad (5.11)$$

where

$v_B$  : boundary diffusion controlled growth rate,

$K$  : boundary segregation coefficient which is the ratio between alloying element concentration in austenite near the boundary and that in the boundary,

$D_B$  : boundary diffusion coefficient of substitutional alloying element,

- $\delta$  : thickness of the boundary,  
 $x_2^{\gamma\alpha}$  : substitutional alloying element concentration at the  $\gamma/\alpha$  interface in  $\gamma$  which is under either local equilibrium or paraequilibrium with  $\theta$ ,  
 $x_2^{\gamma\theta}$  : substitutional alloying element concentration at the  $\gamma/\theta$  interface in  $\gamma$  which is under either local equilibrium or paraequilibrium with  $\theta$ ,  
 $\bar{x}_2$  : average substitutional alloying element concentration in the alloy concerned.

Sharma *et al.* [14] determined the factor  $KD_B\delta$  for Cr steels with from 0.9 to 1.8 wt.% of Cr, giving:

$$KD_B\delta = 7.6 \times 10^{-8} \exp\left(-\frac{40350}{RT}\right), \text{ cm}^3 \text{ s}^{-1}. \quad (5.12)$$

These models have been applied to calculate theoretically the growth rate of pearlite [7,14,20,21]. Although the calculated results show reasonable agreement with experimentally observed growth rates of pearlite in plain carbon steels [7], it seems to be more difficult to predict the growth rate of pearlite in alloyed steels. At higher temperatures, where lower supersaturations are expected to exist, boundary diffusion of the substitutional alloying element seems to control the growth of pearlite [7,14,21]. At higher supersaturations, on the other hand, the reaction seems to be controlled by volume diffusion under local equilibrium [14,19,22]. It is, however, worth pointing out that experimentally observed growth rate of pearlite tends to have the maximum velocity at a certain temperature. This was observed in Fe-C-Cr alloys [14,21], in Fe-C-Mn-Cr alloys [18], in Fe-C-Mn alloys [16,23] and Fe-C alloys [15,24], whereas the theoretical calculations have not succeeded in reproducing the position of the peak and the slope below the peak, except a work of Hashiguchi and Kirkaldy [19] who have combined volume and boundary diffusion controlled growth models and managed to obtain an excellent agreement with experimentally observed growth rates of pearlite in a Fe-C binary system, although they had to adopt a few adjustable parameters. Therefore it can be said that the calculation of the growth rate of pearlite at lower temperature is not yet established.

## 5.5 CALCULATION OF THE INTERFACE COMPOSITIONS

The growth rate of pearlite as discussed in the previous section depends upon the interface compositions of ferrite, cementite and austenite. In order to determine the full set of the interface compositions, we need to know the  $\gamma/\alpha$ ,  $\gamma/\theta$  and  $\alpha/\theta$  interface compositions of carbon and the alloying element in Fe-C-X ternary alloys (X denotes the third substitutional element in the alloy). If the heterogeneity of the chemical concentration in ferrite and cementite is ignored, the eight interface compositions  $x_1^{\gamma\alpha}$ ,  $x_2^{\gamma\alpha}$ ,  $x_1^{\alpha\gamma}$ ,  $x_2^{\alpha\gamma}$ ,  $x_1^{\gamma\theta}$ ,  $x_2^{\gamma\theta}$ ,  $x_1^{\theta\gamma}$  and  $x_2^{\theta\gamma}$  are to be determined.

An approximate method which has been reported by Kirkaldy and his coworkers [25-27] will be used for the calculation of the interface compositions under either paraequilibrium or local equilibrium. The equilibrium condition can be expressed by the equality of the chemical potentials of each element in both phases at the interface. The chemical potentials of carbon, X and iron in ferrite, austenite and cementite are expressed as follows; the numbers 0, 1 and 2 denote, respectively, iron, carbon and the substitutional alloying element X.

In austenite and ferrite;

$$\mu_0 = G_0 + RT \ln x_0 - \frac{RT}{2} \sum \epsilon_{ii} x_i^2 - RT \epsilon_{12} x_1 x_2 \quad (5.13)$$

$$\mu_1 = G_1 + RT \ln x_1 + RT \sum \epsilon_{1i} x_i \quad (5.14)$$

$$\mu_2 = G_2 + RT \ln x_2 + RT(\epsilon_{12} x_2 + \epsilon_{22} x_2) \quad (5.15)$$

and in cementite;

$$\mu_{\text{Fe}_3\text{C}} = G_{\text{Fe}_3\text{C}} + \frac{3}{4} RT \ln y_0^\theta + \frac{3}{4} (1 - y_0^\theta) w_{02} y_2^\theta \quad (5.16)$$

$$\mu_{\text{M}_3\text{C}} = G_{\text{M}_3\text{C}} + \frac{3}{4} RT \ln y_2^\theta + \frac{3}{4} y_0^\theta w_{02} (1 - y_2^\theta). \quad (5.17)$$

where  $y_i^\theta = \frac{4}{3} x_i^{\gamma\theta}$  are the  $i$ -th element concentration in cementite,  $w$ 's are Fe-X interaction coefficients and  $\epsilon$ 's are Wagner's interaction coefficients.

In the case of paraequilibrium, the interface compositions can be determined from the following equations.

$$\mu_1^\gamma = \mu_1^\alpha \quad (5.18)$$

$$x_0^{\gamma\alpha} (\mu_0^\gamma - \mu_0^\alpha) + x_2^{\gamma\alpha} (\mu_2^\gamma - \mu_2^\alpha) = 0 \quad (5.19)$$

$$x_0^{\gamma\theta} \left( \frac{4}{3} \mu_{\text{Fe}_3\text{C}} - \mu_0^\gamma - \frac{1}{3} \mu_1^\gamma \right) + x_2^{\gamma\theta} \left( \frac{4}{3} \mu_{\text{M}_3\text{C}} - \mu_2^\gamma - \frac{1}{3} \mu_1^\gamma \right) = 0 \quad (5.20)$$

with the relation expressing the definition of the paraequilibrium,

$$\frac{x_2^{\alpha\gamma}}{x_0^{\alpha\gamma}} = \frac{x_2^{\gamma\alpha}}{x_0^{\gamma\alpha}} = \frac{x_2^{\gamma\theta}}{x_0^{\gamma\theta}} = \frac{y_2^\theta}{y_0^\theta} = \frac{\bar{x}_2}{\bar{x}_0} = k_2 \quad (5.21)$$

and the constant carbon concentration in cementite,  $x_1^{\theta\gamma} = 0.25$ .

In the case of the local equilibrium at the interface, on the other hand, the equilibrium conditions can be expressed as follows.

$$\mu_i^\alpha = \mu_i^\gamma, (i = 0 \text{ to } 2) \quad (5.22)$$

$$4\mu_{\text{Fe}_3\text{C}} = 3\mu_0^\gamma + \mu_1^\gamma \quad (5.23)$$

$$4\mu_{\text{M}_3\text{C}} = 3\mu_2^\gamma + \mu_1^\gamma \quad (5.24)$$

As long as a dilute solution is concerned, the following expressions can be adopted for the calculation of the interface compositions under either the paraequilibrium or the local equilibrium. For the  $\gamma/\alpha$  equilibrium:

$$x_1^{\alpha\gamma} = A_1 x_1^{\gamma\alpha} \quad (5.25)$$

$$x_2^{\alpha\gamma} = A_2 x_2^{\gamma\alpha} \quad (5.26)$$

and for the  $\gamma/\theta$  equilibrium:

$$y_2^\theta = B_2 x_2^{\gamma\theta} \quad (5.27)$$

with

$$A_1 = \frac{\exp(\Delta G_1^{\alpha\gamma}/RT + \epsilon_{11}^\gamma x_1^{\gamma\alpha})}{1 + \epsilon_{11}^\alpha x_1^{\gamma\alpha} \exp(\Delta G_1^{\alpha\gamma}/RT)} \quad (5.28)$$

$$A_2 = \frac{\exp(\Delta G_2^{\alpha\gamma}/RT + \epsilon_{1i}^\gamma x_1^{\gamma\alpha})}{1 + \epsilon_{1i}^\alpha x_1^{\gamma\alpha} \exp(\Delta G_1^{\alpha\gamma}/RT)} \quad (5.29)$$

$$B_2 = \exp\left[\left\{\left(\frac{4}{3}G_{\text{Fe}_3\text{C}} - G_0^\gamma - \frac{1}{3}G_1^\gamma\right) - \left(\frac{4}{3}G_{\text{M}_3\text{C}} - G_2^\gamma - \frac{1}{3}G_1^\gamma\right) - w_{02}\right\}/RT + \epsilon_{1i}^\alpha x_1^{\gamma\alpha}\right] \quad (5.30)$$

When the growth rate of pearlite is controlled by the diffusion of carbon in austenite ahead of the interface between pearlite and austenite, it is natural to assume that there is no redistribution of X between matrix and precipitate phases. Therefore, the interface composition may be determined by the paraequilibrium condition.

When the redistribution of the third element X can occur during the growth event of pearlite, on the other hand, the local equilibrium condition is maintained at the interfaces. Since the diffusion of X is the controlling process in this case, the flux of carbon in the parent phase should be negligible when it is compared with that of X in the interfaces. This condition is referred to as 'partitioning under local equilibrium' (PLE) as it is well established in the case of the formation of ferrite from austenite [28,29]. The diffusivity of X, in this case, is expected to be much faster than that in the matrix (*i.e.* austenite) [30]. The bulk diffusion coefficient of Cr in austenite at 600°C is calculated to be  $2.5 \times 10^{-18} \text{ cm}^2 \text{ s}^{-1}$  whereas the boundary diffusivity is  $9.6 \times 10^{-10} \text{ cm}^2 \text{ s}^{-1}$  [30], assuming that the thickness of the interface is  $3 \times 10^{-8} \text{ cm}^2 \text{ s}^{-1}$ , which is comparable to the diffusion coefficient of carbon in austenite calculated to be  $1.7 \times 10^{-9} \text{ cm}^2 \text{ s}^{-1}$  [31]. When the growth rate of pearlite is controlled by the diffusion of X atoms within the interface region, the partitioning under local equilibrium (PLE) may exist at the interfaces, under which the activities of carbon in austenite at the  $\gamma/\alpha$  and  $\gamma/\theta$  interfaces are identical so that the flux of carbon ahead of the interfaces is negligible, thus allowing the diffusion of X atoms catch up with that of carbon. Therefore the interface compositions can be determined by two tie lines AB and CD in Fig. 5.11, where the line AC is the isoactivity line of carbon in austenite. The PLE condition maintains until the supersaturation becomes large enough to make the flux of X atom comparable to that of carbon by producing a sharp spike at the vicinity of the interface. This condition should be designated as 'negligible partitioning under local equilibrium' (NPLE). Since there are two interfaces,  $\gamma/\alpha$  and  $\gamma/\theta$ , four different combinations of equilibrium at the interfaces are possible to exist; (1) PLE at the both interfaces, (2) NPLE at the both interfaces, (3) PLE at the  $\gamma/\alpha$  interface and NPLE at the  $\gamma/\theta$  interface, and (4) the vice versa. The transition from the PLE to the NPLE condition occurs when  $x_2^{\alpha\gamma} = \bar{x}_2^\gamma$  for the  $\gamma/\alpha$  interface and under the PLE condition  $x_2^{\theta\gamma} = \bar{x}_2^\gamma$  for the  $\gamma/\theta$  interface (Fig. 5.12).

At the final stage of the reaction, ferrite and cementite should be in equilibrium such that the compositions are determined by the tie line passing through the bulk composition of the steel in the ferrite/cementite two phase region. In the real situation, however, the partitioning of the substitutional alloying element becomes small as the temperature decreases.

Calculated phase diagrams for a Fe-1.08Mn-C wt.% and a Fe-1.41Cr-C wt.% alloys at different temperatures are presented in Fig. 5.13.

## 5.6 CALCULATION OF THE GROWTH RATE OF PEARLITE

Using the method described in the previous section for the calculation of the interface compositions, the growth rates of pearlite in Fe-C-X (X = Mn and Cr) ternary alloys were calculated. The two alloying elements were selected because fine experimental results are available from the published literature.

Calculation of paraequilibrium growth rate of pearlite is straightforward; *i.e.* the interface compositions calculated as discussed in the previous section will be used in equation (5.7) with the expressions for  $s$  and  $s_C$ . The diffusion coefficient of carbon in austenite is calculated as discussed by Trivedi and Pound [32]. The growth rate under the local equilibrium, on the other hand, is not as simple as the paraequilibrium case. In order to calculate the growth rate of pearlite under the local equilibrium, the constants  $K$ ,  $D_B$  and  $\delta$  in equation (5.11) should be determined. It is, however, less clear how to derive the constants. Therefore an empirical method which was used by Sharma *et al.* [14] is adopted here.

As mentioned earlier, the diffusion of substitutional alloying elements plays an important role when the supersaturation is low. As a result, the growth rate of pearlite is considered to be controlled by the interface diffusion of the substitutional alloying element at higher temperatures, whereas by the bulk diffusion of carbon at lower temperatures. However, as it is well established, the partitioning of chromium is observed even at temperatures where bainite transformation takes place [21]. Therefore interface diffusion may play an important role on governing the growth rate of pearlite even at low temperatures. Although Sharma *et al.* [14] obtained equation (5.12) using the data of the growth rate of pearlite at low supersaturations, it may be possible to modify the equation to include the data at higher supersaturations. Therefore the factor  $KD_B\delta$  is estimated using the calculated interface compositions and the interlamellar spacing for eutectoid steels containing Mn or Cr using the following equation.

$$KD_B\delta = v_B / \left[ 12 \frac{s^2}{s_\alpha s_\theta} \frac{(x_2^{\gamma\alpha} - x_2^{\gamma\theta})}{\bar{x}_2} \frac{1}{s^2} \left( 1 - \frac{s_C}{s} \right) \right] \quad (5.31)$$

where the ratio between  $s_\alpha$  and  $s_\theta$  is assumed to be 7. The values  $s_C$  and  $s$  are calculated using equations (5.8) and (5.9) respectively. The data used to obtain the equation are listed in Table 5.3.

Assuming the same expression of  $K\delta D_B$  as equation (5.12), we now obtain a relation as follows (Fig. 5.14).

$$KD_B\delta = C_0 \exp \left( -\frac{Q_B}{RT} \right), \text{ cm}^3 \text{ s}^{-1}. \quad (5.32)$$

where constants  $C_0$  and  $Q_B$  are  $2.223 \times 10^{-8} \text{ cm}^3 \text{ s}^{-1}$  and  $140940 \text{ J mol}^{-1}$  for the 1.1 wt.% Mn steel and  $1.052 \times 10^{-8} \text{ cm}^3 \text{ s}^{-1}$  and  $148320 \text{ J mol}^{-1}$  for the Cr steels with between 0.9 and 1.8 wt.% of Cr. Assuming that the boundary diffusivities of Mn and Cr are same as

$T, ^\circ\text{C}$	$\bar{x}_1, \text{wt.}\%$	$v_B, \text{cm}^2 \text{s}^{-1}$	$1/s, \text{cm}^{-1}$	$x_2^{\gamma\alpha} - x_2^{\gamma\theta}$	$KD_B\delta, \text{cm}^3 \text{s}^{-1}$
720	Cr=1.8	0.35E-04	0.78E+05	0.0102	8.90E-17
720	Cr=1.3	0.18E-04	0.58E+05	0.0074	8.94E-17
710	Cr=1.8	0.70E-04	0.97E+05	0.0186	7.94E-17
710	Cr=1.3	0.40E-04	0.76E+05	0.0157	7.00E-17
710	Cr=0.9	0.38E-04	0.58E+05	0.0133	9.41E-17
700	Cr=1.8	1.20E-04	1.07E+05	0.0269	7.87E-17
700	Cr=1.3	0.84E-04	0.94E+05	0.0238	6.35E-17
690	Cr=1.8	1.80E-04	1.36E+05	0.0353	5.67E-17
690	Cr=1.3	1.40E-04	1.12E+05	0.0316	5.65E-17
680	Cr=1.8	2.15E-04	1.55E+05	0.0441	4.22E-17
670	Cr=1.8	2.20E-04	1.75E+05	0.0530	2.78E-17
660	Cr=1.4	5.00E-04	1.94E+05	0.0504	3.94E-17
650	Cr=1.4	4.50E-04	2.14E+05	0.0504	2.56E-17
640	Cr=1.4	3.70E-04	2.33E+05	0.0592	1.57E-17
670	Mn=1.1	0.82E-04	0.56E+05	0.0220	1.16E-16
660	Mn=1.1	1.45E-04	0.72E+05	0.0266	1.01E-16
640	Mn=1.1	5.22E-04	1.04E+05	0.0378	1.21E-16
620	Mn=1.1	11.3E-04	1.36E+05	0.0529	1.09E-16
580	Mn=1.1	11.3E-04	2.01E+05	0.0827	3.25E-17
550	Mn=1.1	9.22E-04	2.49E+05	0.1050	1.37E-17
530	Mn=1.1	4.59E-04	2.81E+05	0.1200	4.73E-18

Table 5.3: Calculation of  $KD_B\delta$  from published pearlite growth data in Fe-C-Cr and Fe-C-Mn alloys. The first eleven data are after Sharma *et al.* [14], the next three data after Chance and Ridley [21] and the last seven data after Razik [16].  $x_2^{\gamma\alpha} - x_2^{\gamma\theta}$  is measured in mole fraction.

the self boundary diffusion coefficient of iron in austenite,  $D_B\delta$  can be expressed as  $5.4 \times 10^{-8} \exp(-155500/RT) \text{cm}^2 \text{s}^{-1}$  [30]. This gives expressions for the boundary segregation coefficients  $K = 0.41 \exp(14560/RT)$  and  $K = 0.20 \exp(7180/RT)$  for Mn and Cr respectively. The boundary segregation coefficients of Mn and Cr are evaluated to be 3.0 and 0.54 at 600° C respectively.

Ridley [8] reported the growth rate of pearlite, interlamellar spacing and partition coefficient in 1.08 wt% Mn and 1.41 wt.% Cr eutectoid steels (Fig. 5.15). The growth rate of pearlite has a peak in both cases whereas the partition coefficient shows a monotonous decrease towards the unity at lower temperatures. It is worth noting, however, the change in the partition coefficient as a function of reaction temperature in the Cr steel is more moderate than that in the Mn steel (Fig. 5.15).

The calculation of the interface compositions under local equilibrium was carried out using the method described in the previous section. The calculated interface compositions  $x_2^{\theta\gamma}$  and  $x_2^{\alpha\gamma}$  were then used to derive the partition coefficient  $K_P$  of X using the following expression.

$$K_P = x_2^{\theta\gamma}/x_2^{\alpha\gamma} \quad (5.33)$$

At higher temperatures, the partition coefficient is expected to have a larger value since the supersaturation of austenite is small at those temperatures whereas the mobility of X atom is high. The value  $K_P$  decreases with temperature and reaches the unity when the NPLE condition maintains both at the  $\gamma/\alpha$  and at the  $\gamma/\theta$  interfaces. A change in the  $K_P$  value in eutectoid steels with either 1.08% Mn or 1.41% Cr as a function of the transformation temperature is plotted in Fig. 5.16 and Fig. 5.17. Experimentally observed partition coefficients [8] were

also plotted in the figures. The calculation was conducted for 0.8, 0.7 and 0.6 wt.% alloys to clarify the effect of supersaturation on the partition coefficient in the case of the Mn steel. As it can be seen from the figures, the calculation seems to express the change in the  $K_P$  value successfully except at higher temperatures where an effect of the level of supersaturation is large. The difference in the change in the  $K_P$  values between the Mn and Cr steels was also reproduced successfully by the present model. The  $K_P$  in the Fe-C-Cr alloy stays higher even at low temperatures when it is compared with the Fe-C-Mn alloy. The PLE condition maintains even at 600° C in the Fe-C-Cr alloy whereas the NPLE condition takes over at around 600° C in the Fe-C-Mn alloy.

The calculated growth rates of pearlite are compared with the experimental values reported by Ridley [8] in Fig. 5.18. The growth rate calculated assuming paraequilibrium diffusion of carbon in austenite shows a good agreement with the observed growth rates except at lower temperatures than the temperature at which the growth rate becomes the maximum. The growth rate of pearlite under local equilibrium also shows a peak which is consistent with the experimental results (Fig. 5.18). Since the constants in equation (5.11) were determined by fitting the equation to the data for the Fe-C-Mn alloy, the growth rate of pearlite calculated under the local equilibrium is naturally consistent to the experimental values.

The paraequilibrium growth rate is retarded by Mn additions as shown in Fig. 5.19. Since the  $Ae_1$  temperature is affected strongly by Mn addition, the growth rate at higher temperature is more sensitive to Mn addition than the lower temperatures. In the case of the local equilibrium, the effect of the Mn addition is more substantial (Fig. 5.20). In the both cases, the growth rate and the peak temperature are reduced by the Mn addition.

The growth rate calculation was also carried out for the Fe-1.41 wt% Cr eutectoid alloy. Calculated growth rates of pearlite under paraequilibrium or local equilibrium conditions are compared against observations in [8] (Fig. 5.21). Although the agreement is not as good as for the Mn steel, the temperature dependence of the growth rate seems to be well expressed especially by the local equilibrium calculation.

Although the equations derived in this work can only be appropriate for the steels concerned above, the calculation was extended to a Fe-0.3C-4.08Cr wt.% in which the growth rate of pearlite at 478 °C was measured to be around  $1.0 \times 10^{-9} \text{ cm s}^{-1}$ . The paraequilibrium growth rate of pearlite at 478 °C was calculated to be  $1.9 \times 10^{-3} \text{ cm s}^{-1}$  which is far larger than the observed one. The local equilibrium calculation gave the growth rate of pearlite equal to  $6.8 \times 10^{-5} \text{ cm s}^{-1}$  at 478 °C which is much smaller than the paraequilibrium growth rate but still orders of larger than the experimental value. However, it should be noted that the theory discussed here is for conventional pearlite whereas the pearlite observed in the Fe-0.3C-4.08Cr wt.% alloy is alloy pearlite. Although the theory of the growth of alloy pearlite has not been developed, this result may suggest, for the first approximation, that the growth of pearlite at very low temperatures is not a diffusion controlled reaction but rather an interface controlled process. As a movement of an interface is controlled both by diffusions of atoms, which provide the chemical concentration differences within each phase, and by a sluggish transfer of atoms across the interface, which therefore does not give rise to any large concentration differences. The former case is referred to as a diffusion-controlled process, and the latter as an interface-controlled process [33]. It is not difficult to imagine that transformations from austenite to ferrite are controlled by the interface process more strongly than the diffusion of atoms. The rate of reaction will then be smaller than that expected by the local equilibrium mechanism

[33].

The rate of reaction controlled by the interface process is given by the following equation [1]:

$$v_I = \delta \nu \exp\left(\frac{-\Delta_a g^*}{RT}\right) \left[1 - \exp\left(\frac{-\Delta g^{\beta\alpha}}{RT}\right)\right] \quad (5.34)$$

where  $\delta$  is the width of the interface,  $\Delta_a g^*$  and  $\Delta g^{\beta\alpha}$  are the activation energy and the driving force for the transformation per atom,  $\nu$  is a characteristic frequency which is given by the value  $kT/h$  where  $k$  and  $h$  are Boltzmann's and Plank's constants respectively.

$\Delta g^{\beta\alpha}$  is calculated as the free energy change due to the formation of pearlite from austenite as follows [34].

$$\begin{aligned} \Delta g^{\beta\alpha} = & (1 - x_1^\gamma) \Delta G_{\text{Fe}}^{\gamma \rightarrow \alpha} + x(\Delta G^\theta + 4.01T - 10580) \\ & - RT \left[ \frac{1 - x_1^\gamma}{5} \ln\left(\frac{1 - 6x_1^\gamma}{1 - x_1^\gamma}\right) + \ln\left(\frac{x_1^\gamma}{1 - 6x_1^\gamma}\right) \right] \end{aligned} \quad (5.35)$$

where

$$\begin{aligned} \Delta G^\theta &= 29325 - 28.74T \text{ J mol}^{-1} \\ \Delta G_{\text{Fe}}^{\gamma \rightarrow \alpha} &= -5024 + 9.86 \times 10^{-3}T^2 - 6.44 \times 10^{-6}T^3 \text{ J mol}^{-1} \end{aligned}$$

Assuming that  $\delta$  being the lattice parameter of austenite,  $\nu$  being  $kT/h = 1.57 \times 10^{13} \text{ s}^{-1}$ , the growth rate controlled by the interface process can be calculated using equation (5.34) as a function of the activation energy  $\Delta_a g^*$ . Since the growth rate of pearlite at  $478^\circ \text{C}$  was measured to be  $1.0 \times 10^{-9} \text{ cm s}^{-1}$ , the activation energy  $\Delta_a g^*$  can be calculated from the equation.  $\Delta G^\theta, \Delta G_{\text{Fe}}^{\gamma \rightarrow \alpha}$  are  $7743.5$  and  $-1551 \text{ J mol}^{-1}$ , hence  $\Delta g^{\beta\alpha} = -1496 \text{ J mol}^{-1}$ . Using the data  $\delta = 3.573 \times 10^{-10} \text{ m}$  and  $\nu = kt/h = 1.57 \times 10^{13} \text{ s}^{-1}$ ,  $\Delta_a g^*$  is calculated to be  $202 \text{ kJ mol}^{-1}$ , which is close to the activation energies of the self diffusion of iron in austenite and ferrite; *i.e.*  $286$  and  $240 \text{ kJ mol}^{-1}$ . Although the activation energy calculated from the observed growth rate at  $478^\circ \text{C}$  is close to that of the self diffusion of iron, it is still uncertain if the reaction is controlled by the interface process. Further work is necessary together with the study of the growth rate of alloy pearlite instead of conventional pearlite to reach a decisive conclusion.

## 5.7 CONCLUSIONS

Although the bainite transformation terminates when the carbon concentration of the untransformed austenite reaches the  $T_0$  or  $T_0'$  curve, the austenite can nevertheless decompose to ferrite and cementite by reconstructive transformation. A case is the formation of pearlite after the cessation of the bainite transformation. In this chapter, pearlite transformation kinetics at low temperatures and the formation of pearlite during heating after the termination of bainite transformation were studied and following conclusions were obtained.

- 1) The formation of pearlite during heating from a bainite transformation temperature after the cessation of the bainite reaction can be understood by the TTT curve for untransformed austenite with the carbon concentration of  $x_{T_0'}$  at the bainite transformation temperature, and by Scheil's rule.
- 2) The result of the analysis is evidence for the incomplete reaction phenomenon during the bainite transformation.

- 3) The incubation period for pearlite transformation observed at 478 °C is reproducible by the upper C-curve of the TTT curve for the alloy.
- 4) The growth rate of pearlite was studied theoretically and the local equilibrium calculation of the interface compositions gave the partition coefficient of the substitutional alloying element which agrees reasonably well with the published results.
- 5) The growth rate of pearlite observed at 478 °C ( $1.0 \times 10^{-9} \text{ cm s}^{-1}$ ) is far smaller than the calculated diffusion controlled growth rate. Although the pearlite observed in this work is alloy pearlite, this discrepancy in the growth rate may mean that the formation of pearlite at very low temperatures is controlled by the interface process instead of the long range diffusion of atoms.

## REFERENCES

1. J. W. Christian: *"The Theory of Transformations in Metals and Alloys Part 1"*, Pergamon Press, Oxford, 1975.
2. H. K. D. H. Bhadeshia: *Metal Science*, 1982, **16**, 159.
3. K. C. Russell: *Acta Metall.*, 1969, **17**, 1123.
4. H. K. D. H. Bhadeshia: *Acta Metall.*, 1980, **28**, 1103.
5. H. K. D. H. Bhadeshia: *Proc. Int. Conf. "Solid-Solid Phase Transformations"*, 1981, 1041.
6. H. K. D. H. Bhadeshia and D. V. Edmonds: *Metall. Trans. A*, 1979, **10A**, 895.
7. M. P. Puls and J. S. Kirkaldy: *Metal. Trans.*, 1972, **3**, 2777.
8. N. Ridley: *Metal. Trans.*, 1984, **15A**, 1019.
9. C. Zener: *Trans. AIME*, 1946, **167**, 550.
10. M. Hillert: *Jernkont Ann.*, 1957, **141**, 757.
11. J. M. Shapio and J. S. Kirkaldy: *Acta Metall.*, 1968, **16**, 579.
12. B. E. Sandquist: *Acta Metall.*, 1968, **16**, 1413.
13. M. Hillert: *"The Mechanism of Phase Transformations in Crystalline Solids"*, Institute of Metals, London, 1969, 231.
14. R. C. Sharma, G. R. Purdy and J. S. Kirkaldy: *Metall. Trans.*, 1979, **10A**, 1129.
15. D. Brown and N. Ridley: *JISI*, 1966, **204**, 811.
16. N. A. Razik, W. Lorimer and N. Ridley: *Acta Metall.*, 1974, **22**, 1249.
17. J. W. Cahn and W. C. Hagel: *"Decomposition of Austenite by Diffusional Processes"*, ed. by V. F. Zackay and H. I. Aaronson, Interscience Publishers, New York, NY, 1962, 131.
18. S. A. Al-Salman, G. W. Lorimer and N. Ridley: *Acta Metall.*, 1979, **27**, 1391.
19. K. Hashiguchi and J. S. Kirkaldy: *Scandinavian Journal of Metall.*, 1984, **13**, 240.
20. B. E. Sandquist: *Acta Metall.*, 1969, **17**, 967.
21. J. Chance and N. Ridley: *Metall. Trans.*, 1981, **12A**, 1205.
22. M. Hillert: *Proc. Int. Conf. on "Solid-Solid Phase Transformations"*, 1981, 789.
23. M. L. Picklesimer, D. L. McElroy, T. M. Kegley, Jr., E. E. Stansbury and J. H. Frye, Jr.: *Trans. AIME*, 1960, **218**, 473.
24. J. H. Frye, Jr, E. E. Stansbury and D. L. McElroy: *Trans. AIME*, 1953, **February**, 219.
25. J. S. Kirkaldy, B. A. Thomson and E. A. Baganis: *"Hardenability Concepts with Applications to Steel"*, ed D. V. Doane and J. S. Kirkaldy, AIME, 1978, 82.
26. J. G. Gilmour, G. R. Purdy and J. S. Kirkaldy: *Metall. Trans.*, 1972, **3**, 1455.

27. K. Hashiguchi and J. S. Kirkaldy: *CALPHAD*, 1984, **8**, 173.
28. M. Hillert: *Internal Report, Swedish Institute of Metals Research*, 1953.
29. J. S. Kirkaldy: *Canadian J. Phys.*, 1958, **36**, 907.
30. J. Fridberg, L-E. Törndahl and M. Hillert: *Jernkont. Ann.*, 1969, **153**, 263.
31. J. Ågren: *Acta Metall.*, 1982, **30**, 841.
32. R. Trivedi and G. M. Pound: *J. Appl. Phys.*, 1969, **38**, 3569.
33. M. Hillert: *Metall. Trans. A*, 1975, **6A**, 5.
34. L. Kaufman and S. V. Radcliffe: "*Decomposition of Austenite by Diffusional Processes*", ed. by V. F. Zackay and H. I. Aaronson, *Interscience Publishers, New York, NY*, 1962, 313.

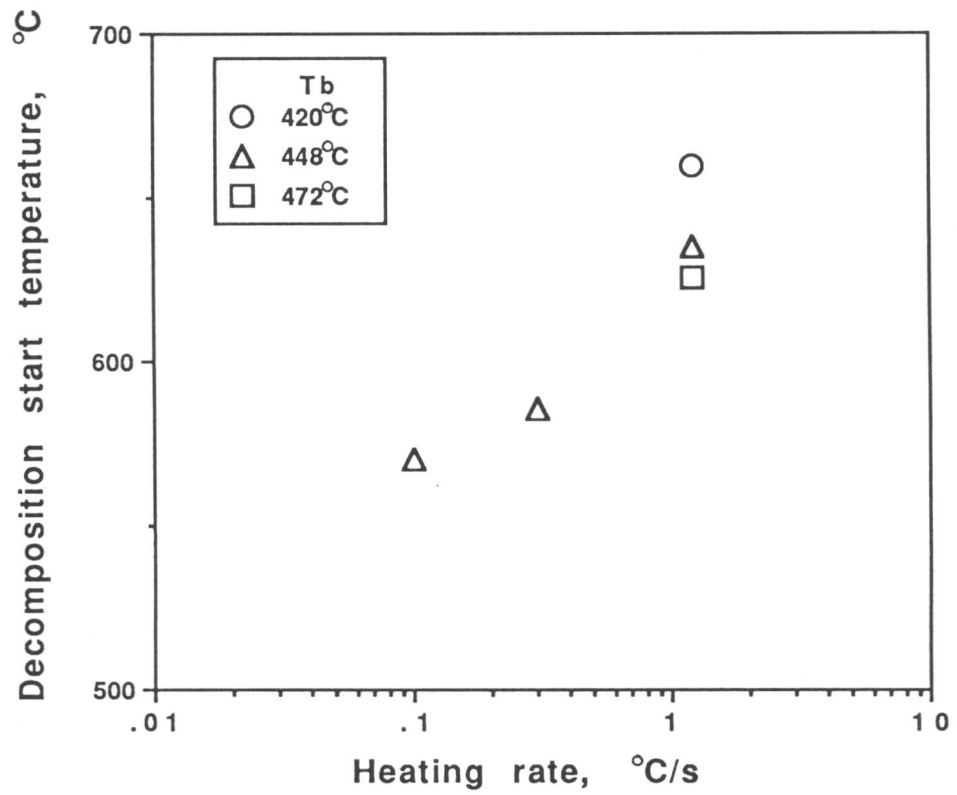


Fig. 5.1 Effect of heating rate on decomposition-start temperature of austenite remaining untransformed after the completion of the bainite transformation.

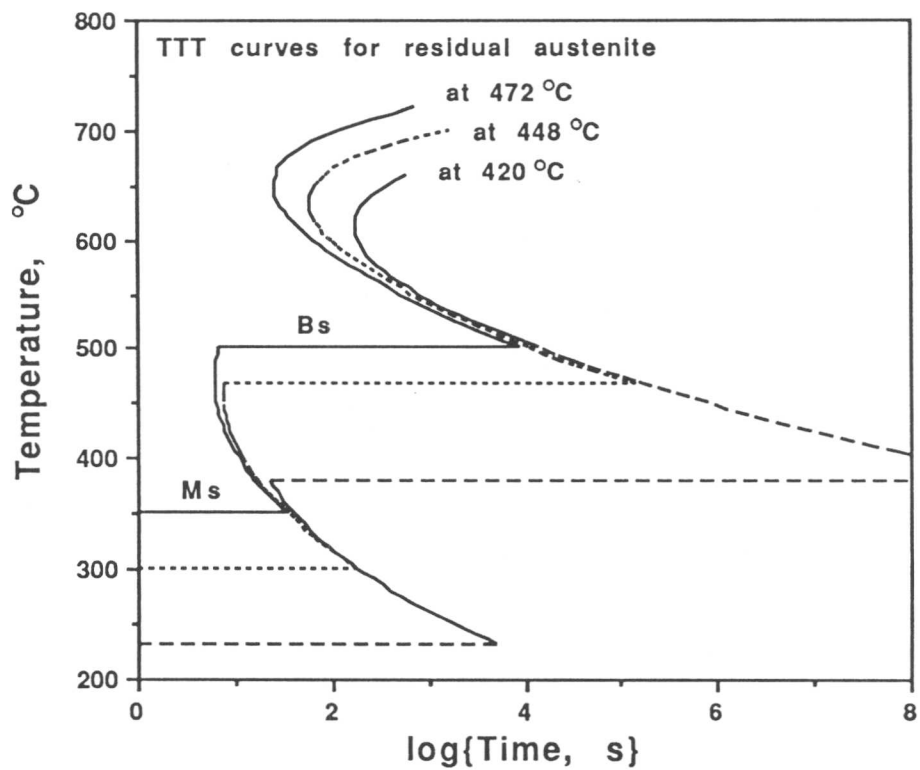


Fig. 5.2 Calculated TTT curves of austenite with chemical composition identical to the residual austenite after the formation of bainitic ferrite at 420 °C, 448 °C and 472 °C respectively.

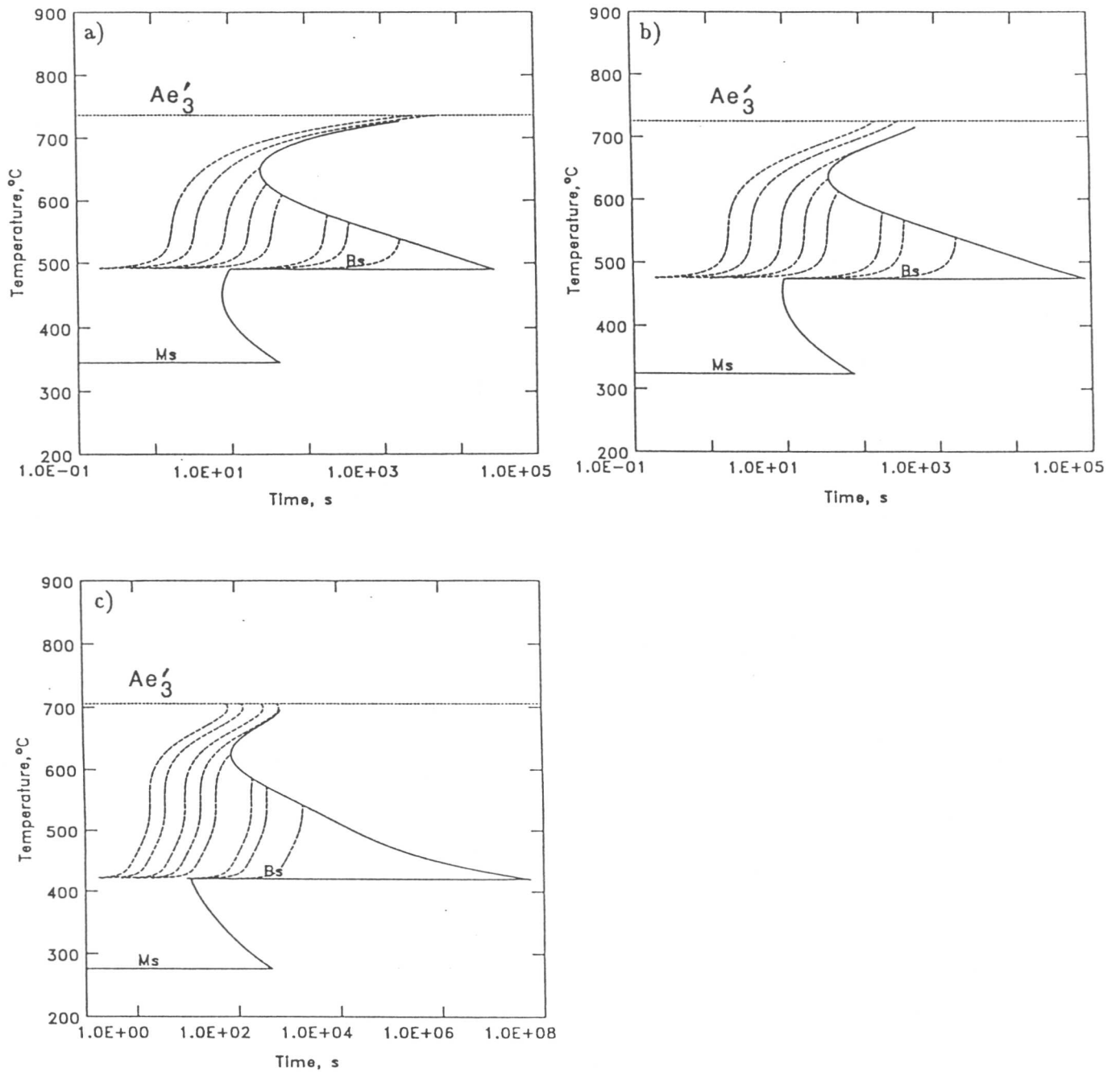


Fig. 5.3 Calculated TTT curves of residual austenite at (a) 420 °C ( $x_{\gamma_0} = 2.4$  at.%), (b) 448 °C ( $x_{\gamma_0} = 1.8$  at.%) and (c) 472 °C ( $x_{\gamma_0} = 1.4$  at.%) (solid line), and the position of austenite in the TTT curves during continuous heating at constant heating rates between 0.01 and 10 °C s<sup>-1</sup> (dashed lines).

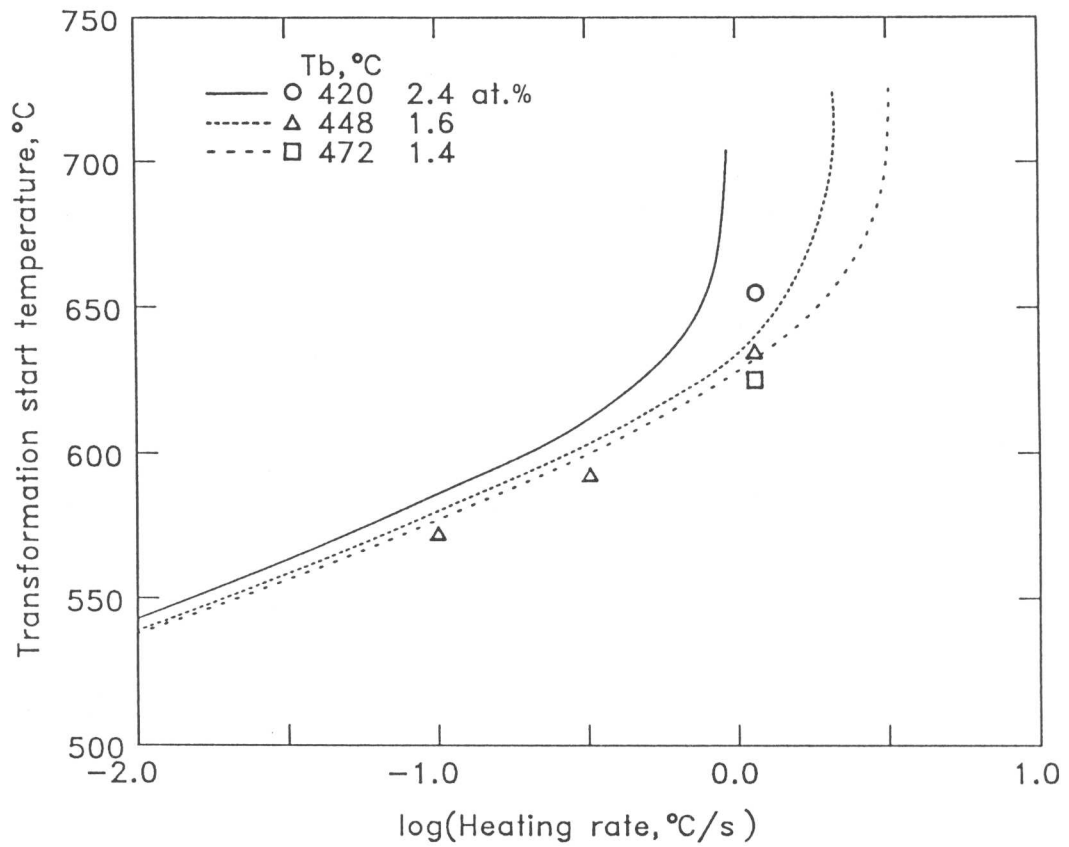


Fig. 5.4 Comparison between observed and calculated decomposition-start temperatures during the heating of austenite which is left untransformed after the bainite transformation steps.

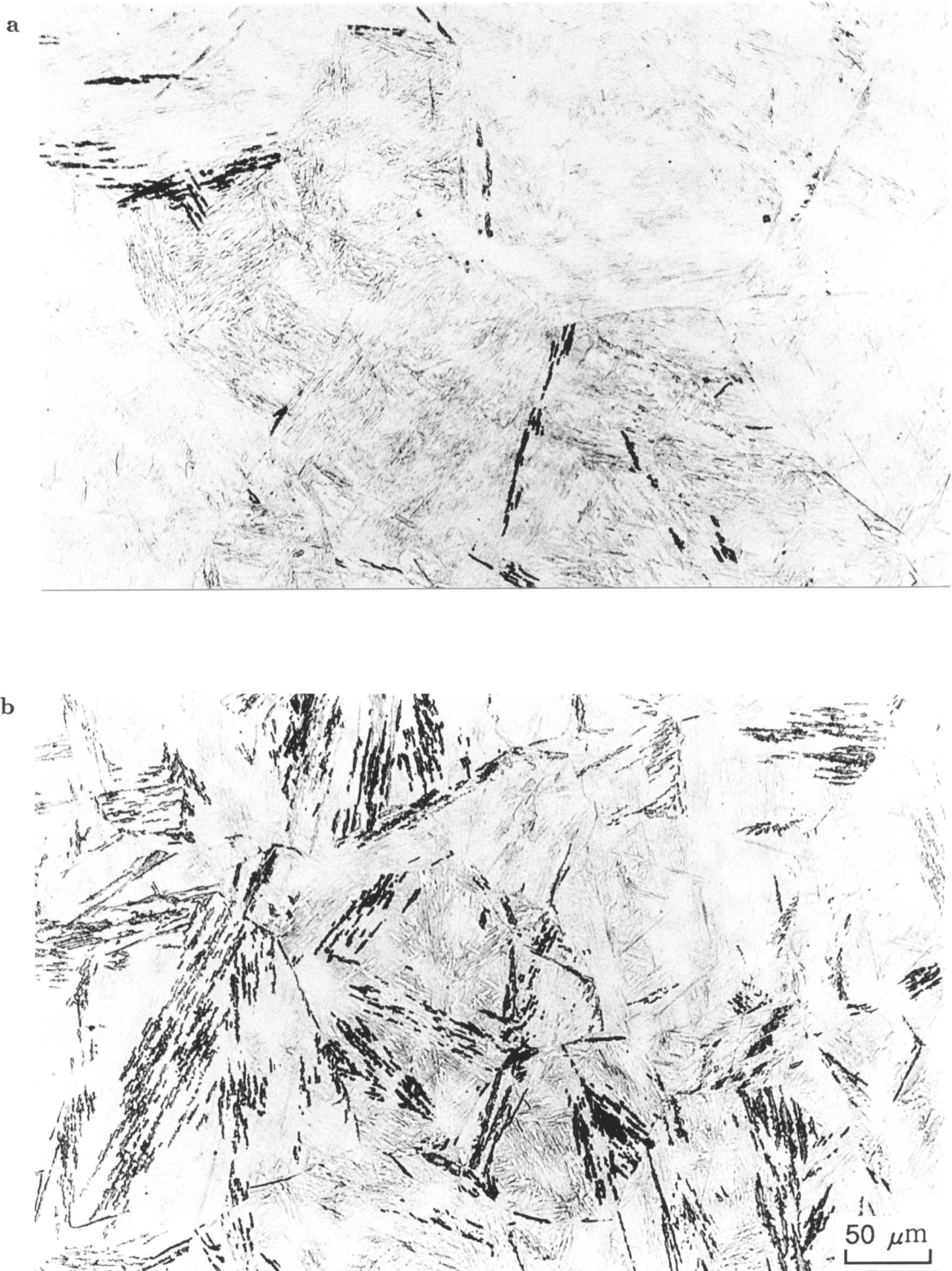
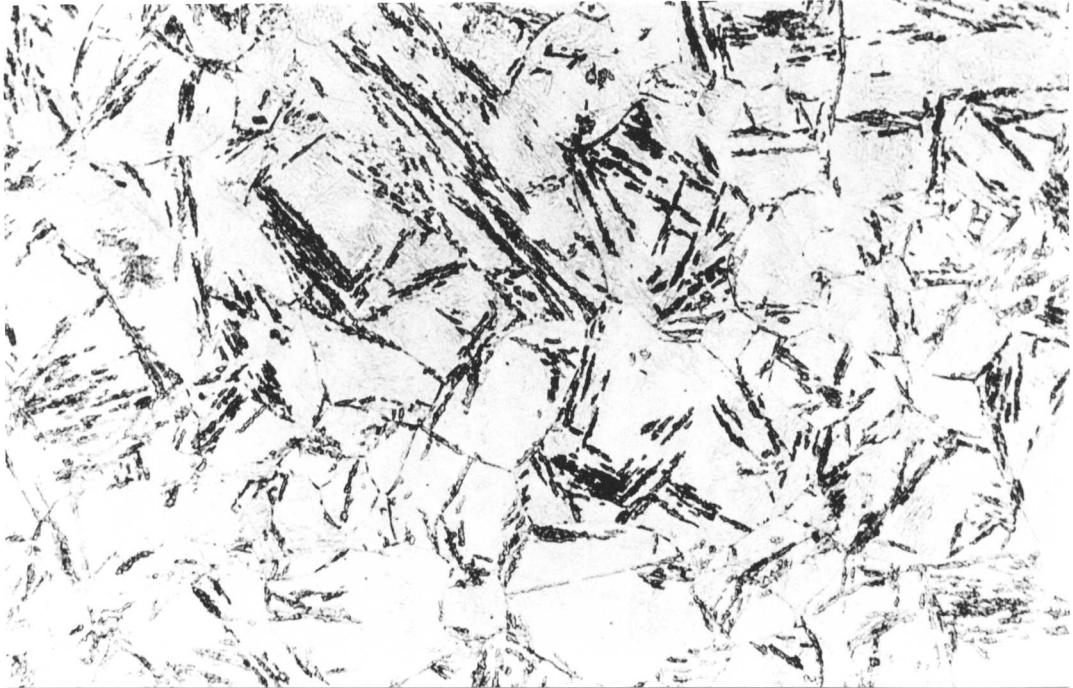


Fig. 5.5 Optical micrographs of specimens isothermally held at 478 °C for (a) 300 sec, (b) 600 sec, (c) 67 hours, (d) 160 hours, (e) 23 days and (f) 43 days.

c



d

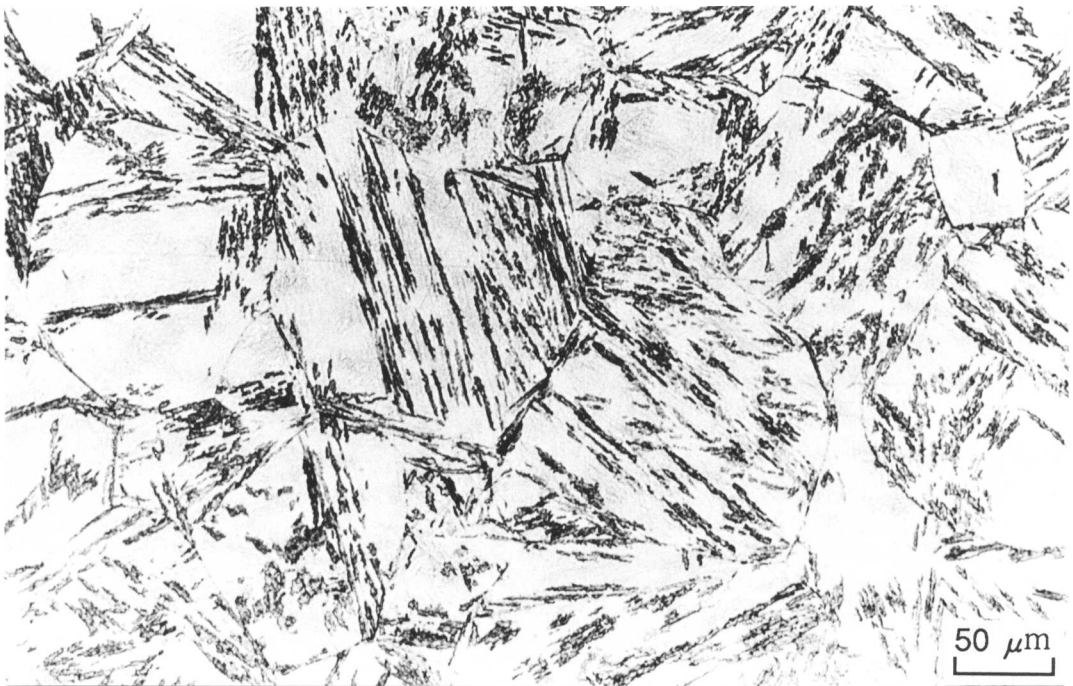


Fig. 5.5 (continued)

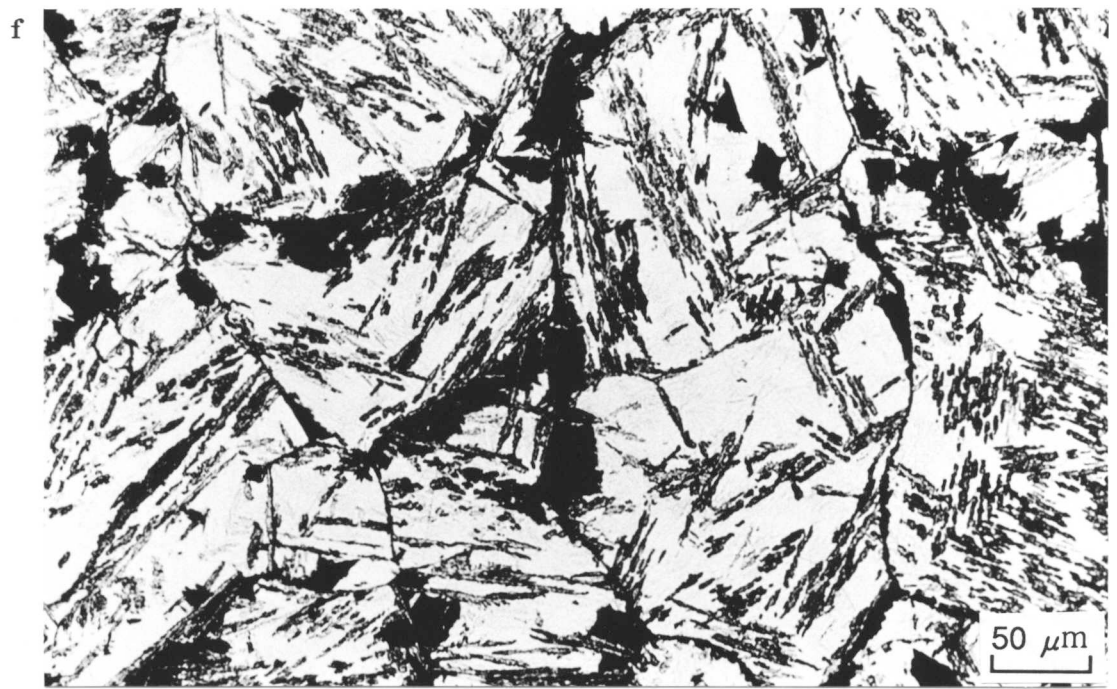
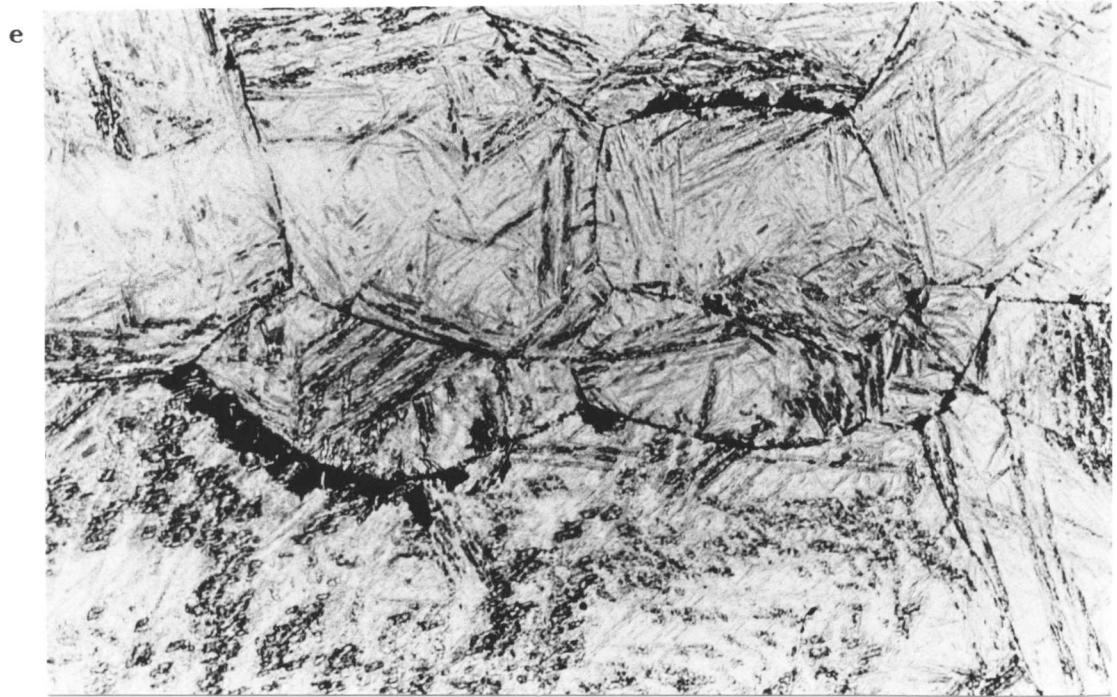


Fig. 5.5 (continued)

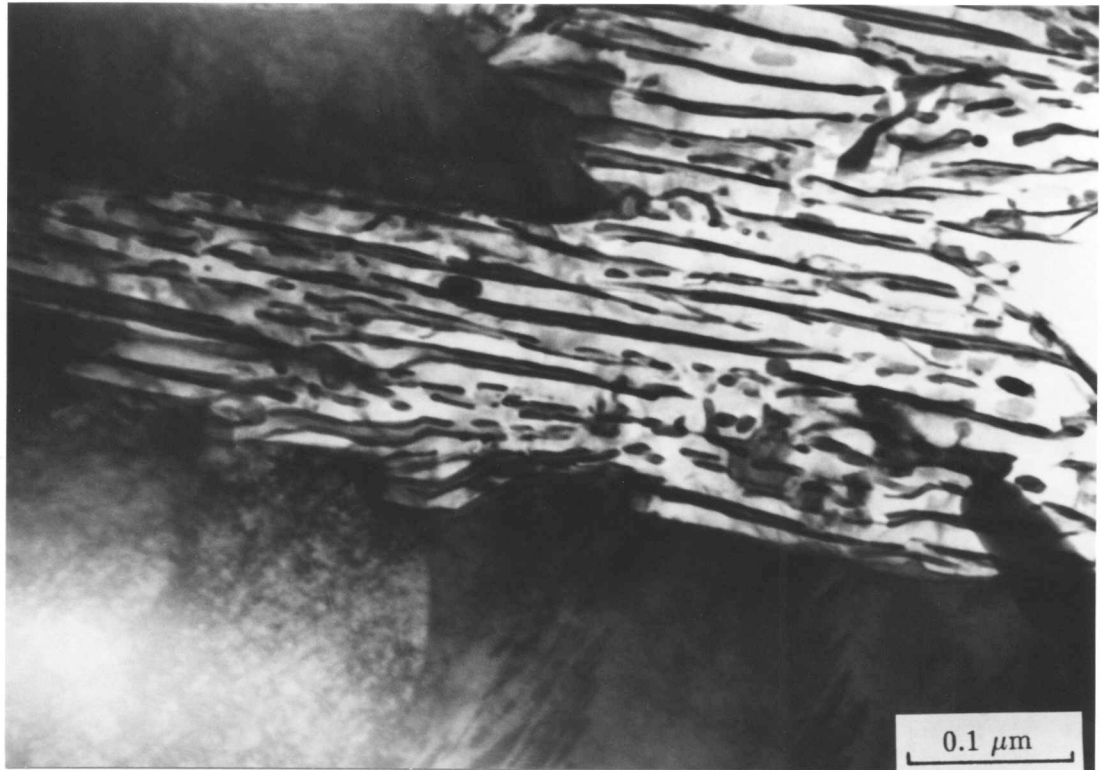


Fig. 5.6 TEM bright field image of alloy pearlite.

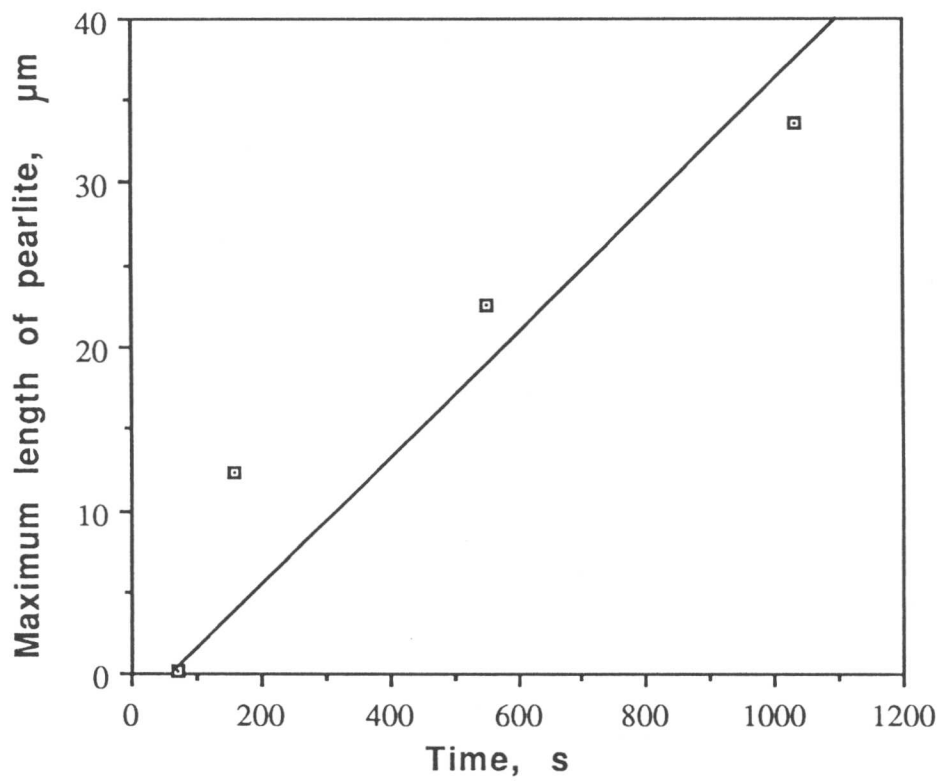


Fig. 5.7 Change in the maximum thickness of pearlite with isothermal holding time at 478 °C.

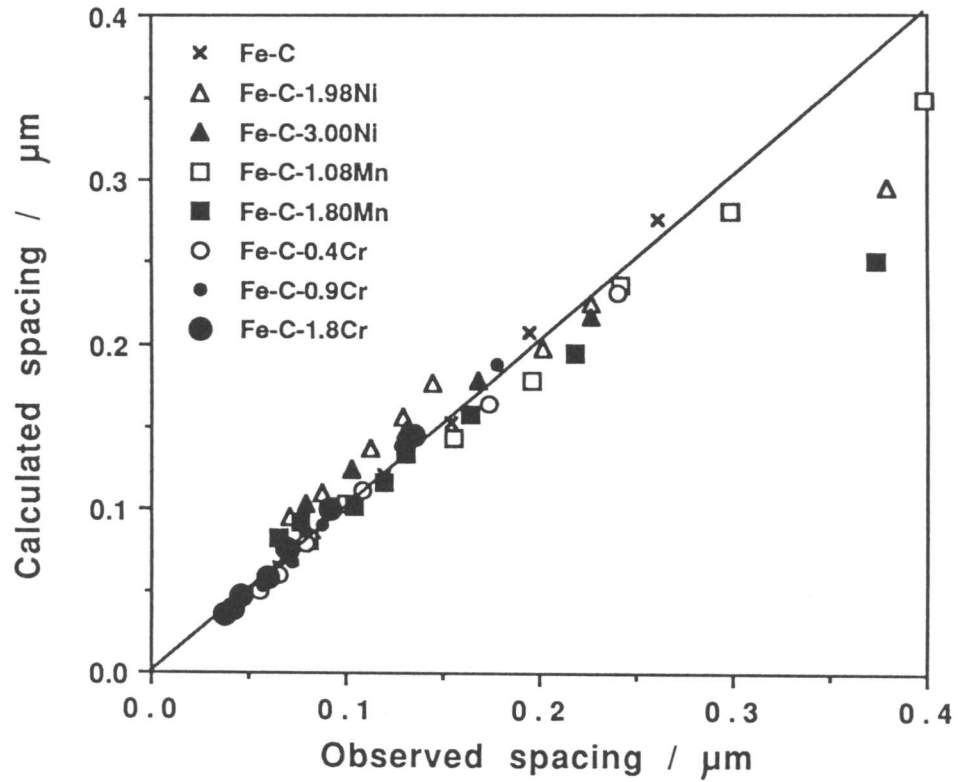


Fig. 5.8 Comparison between observed and calculated interlamellar spacing in Fe-C-Mn, F-C-Ni and Fe-C-Cr alloys.

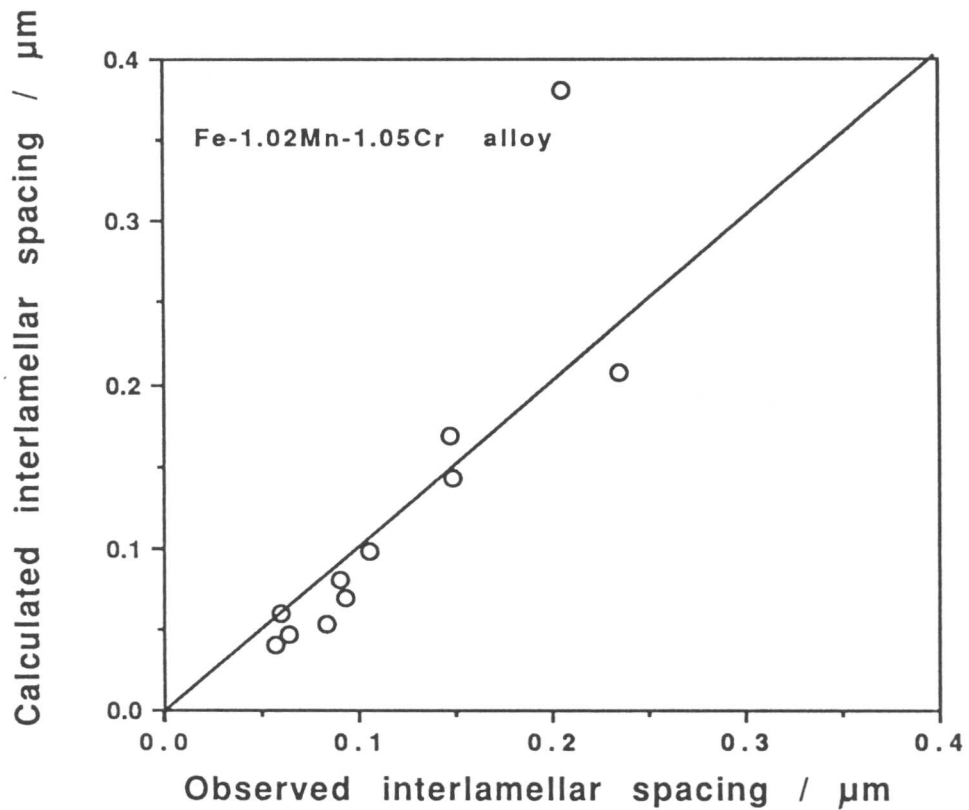


Fig. 5.9 Comparison between observed [18] and calculated interlamellar spacing in a Fe-1.02Mn-1.05Cr alloy.

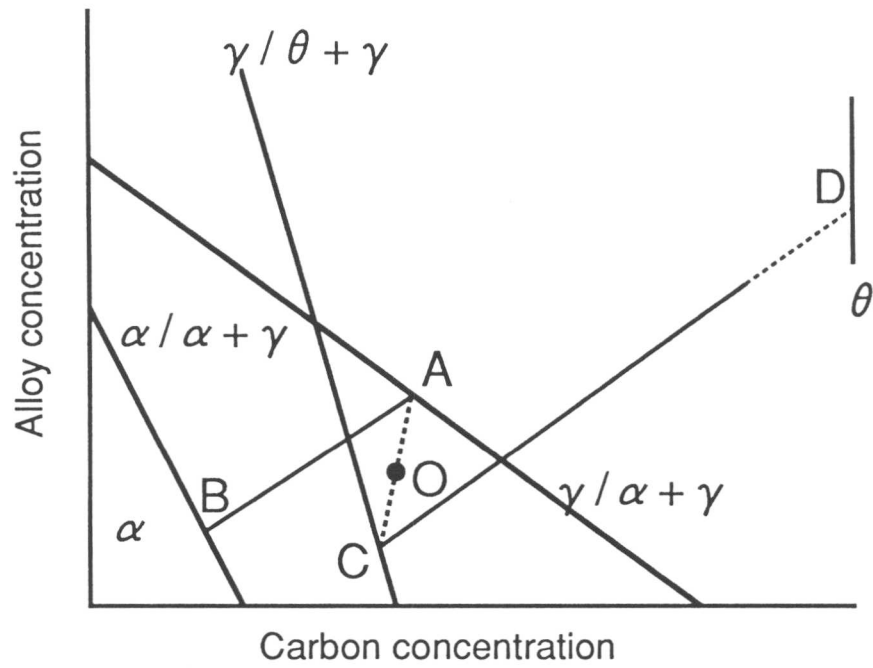


Fig. 5.10 Schematic illustration of the phase diagram showing the interface compositions during the growth of pearlite under local equilibrium.

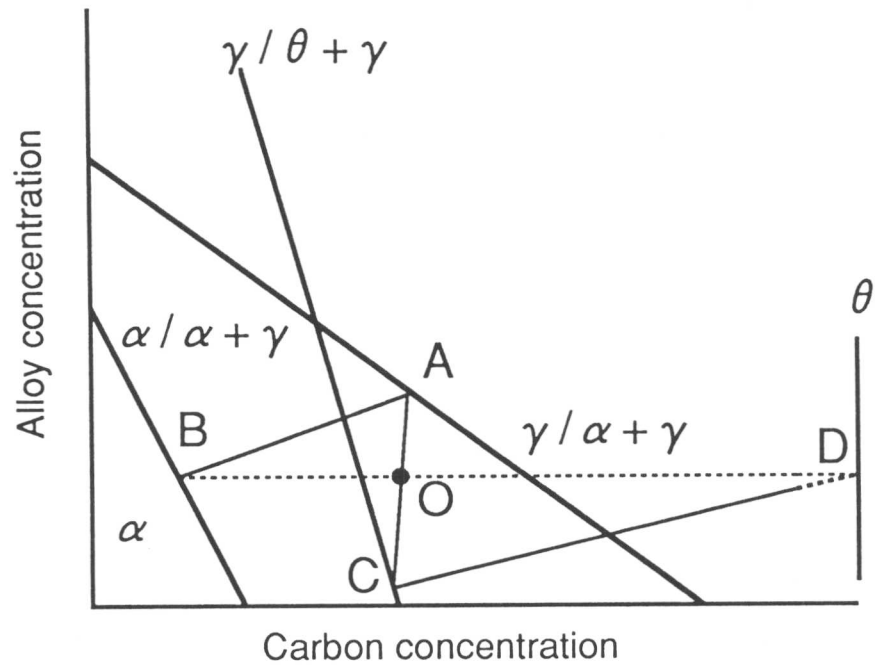


Fig. 5.11 Schematic illustration of the phase diagram showing the interface compositions during the growth of pearlite under the negligible partitioning under local equilibrium.

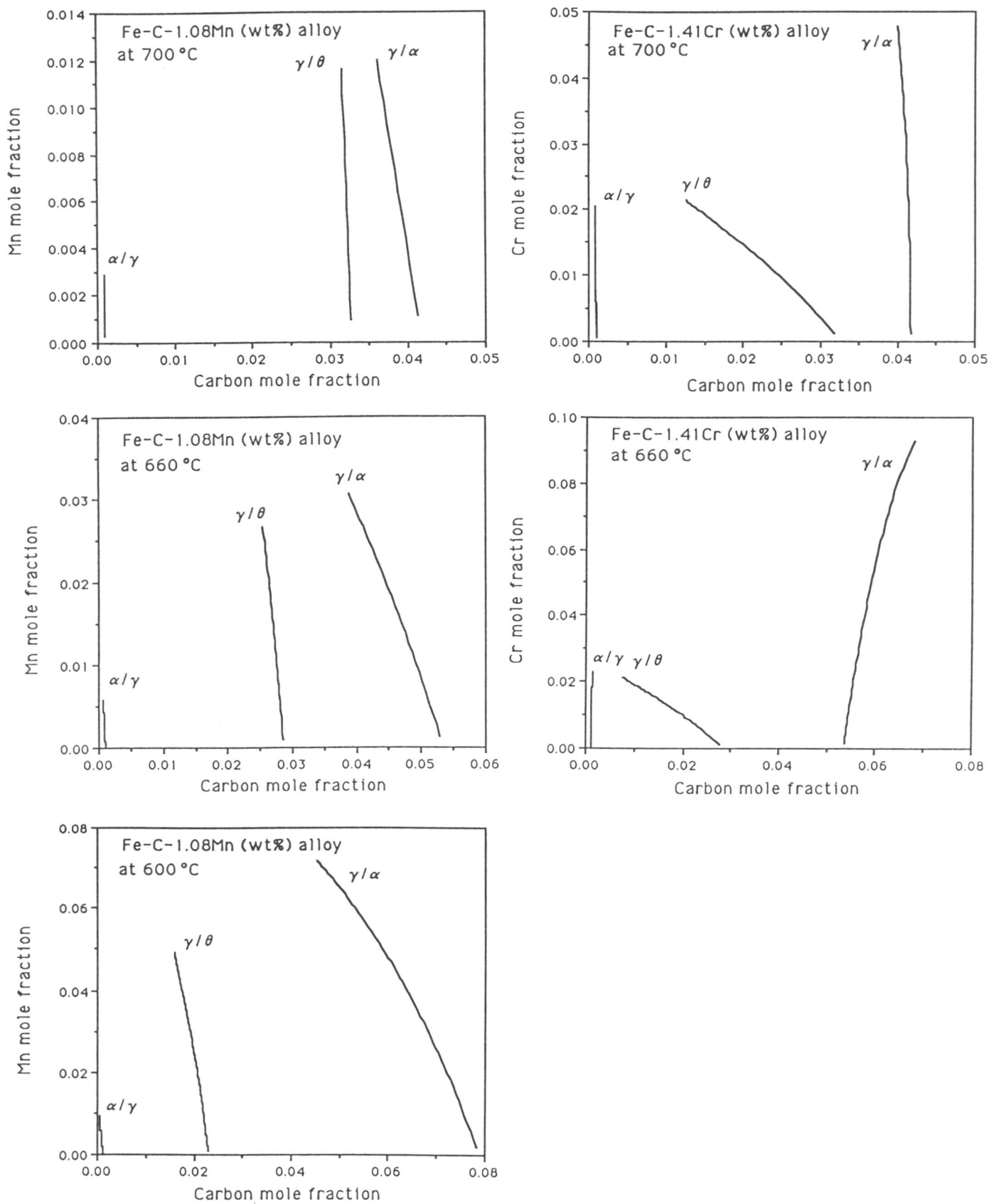


Fig. 5.12 Calculated phase diagrams for a Fe-1.08Mn-C wt.% and a Fe-1.41-C wt.% alloys.

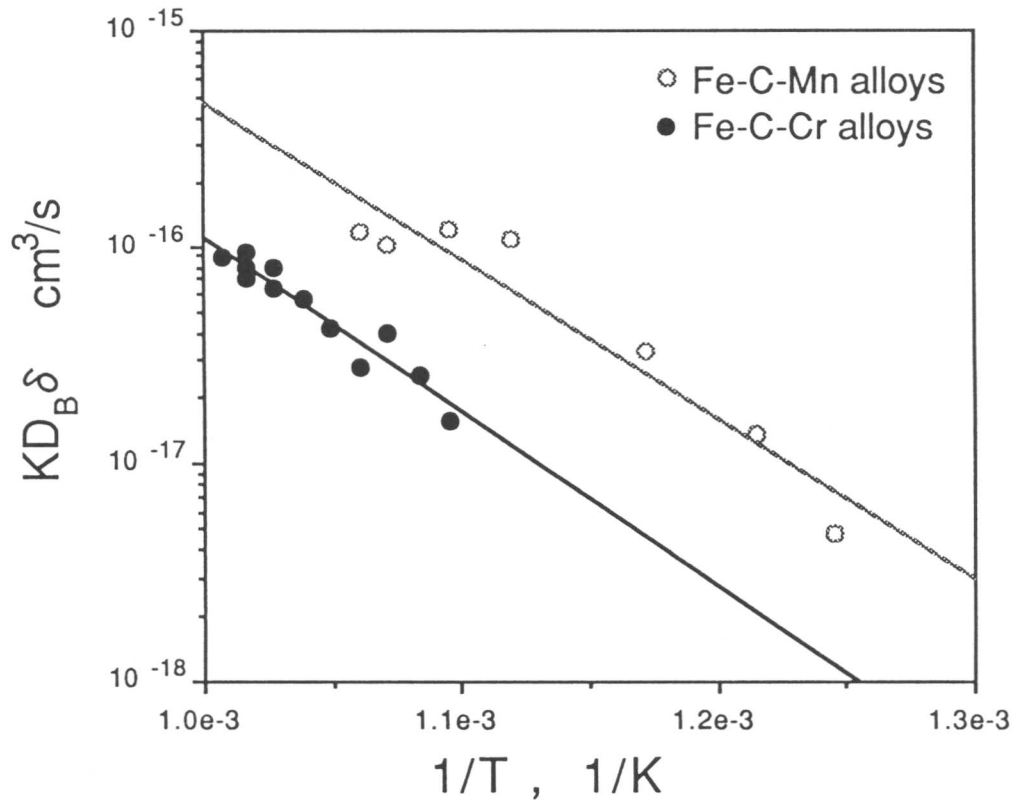


Fig. 5.13 Comparison between observed and calculated  $KD_B\delta$  values in Fe-C-Cr and Fe-C-Mn alloys.

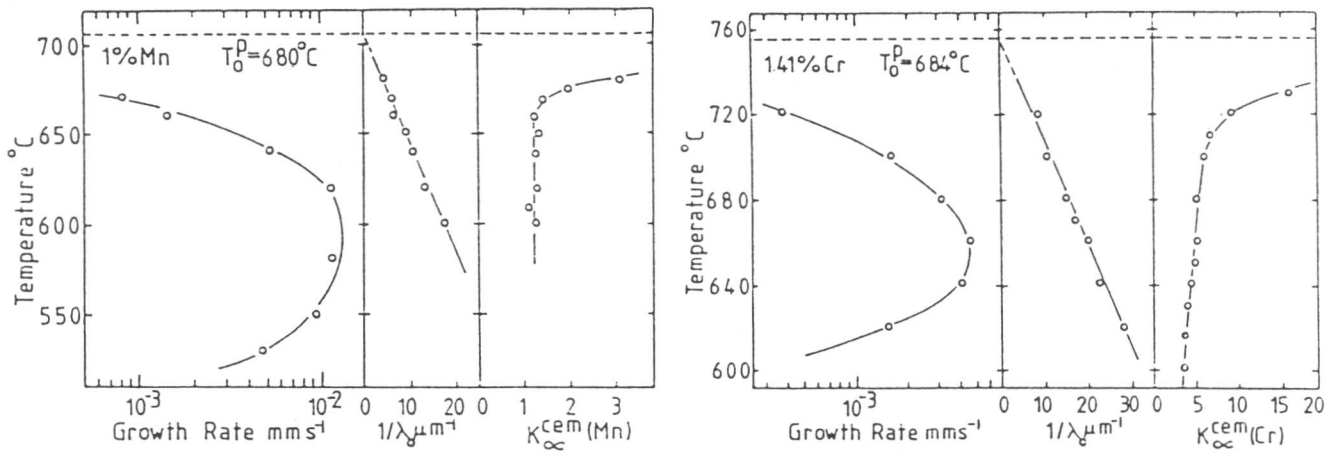


Fig. 5.14 Growth rate of pearlite and the partitioning coefficient of substitutional alloying element as a function of the reaction temperature in (a) a Fe-1.08Mn-C wt.% and (b) a Fe-1.41Cr-C wt.% alloys [8].

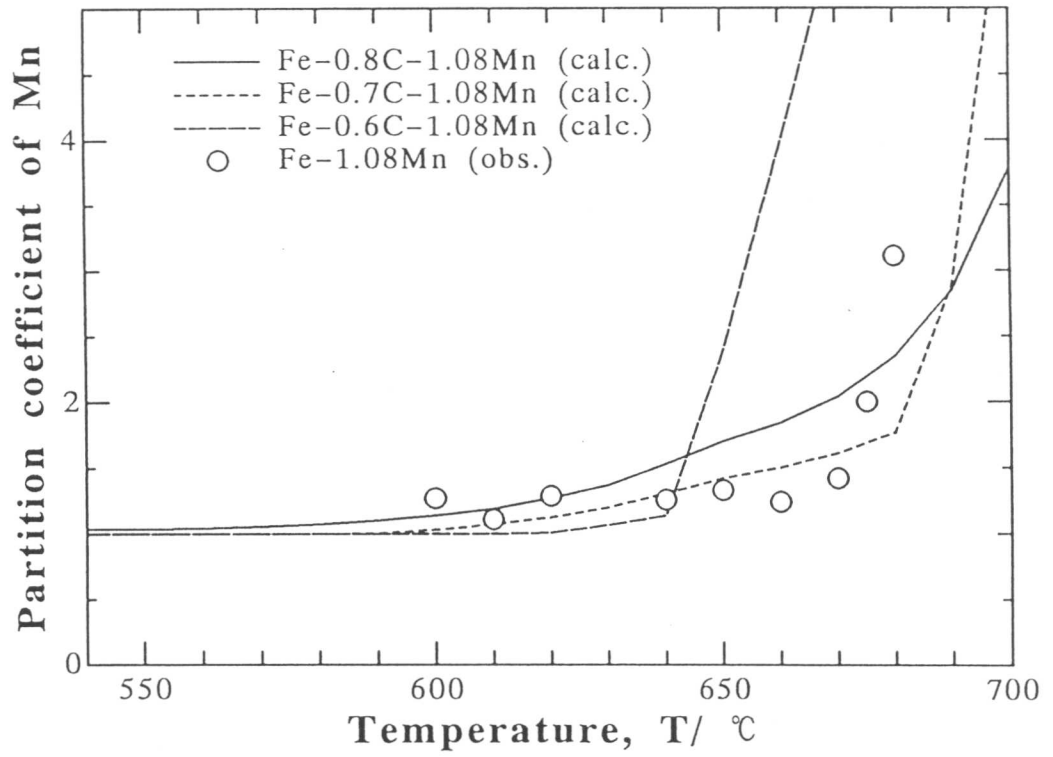


Fig. 5.15 Calculated partition coefficient of Mn in a Fe-1.08Mn-C wt.% alloy. Plots are after Ridley [8].

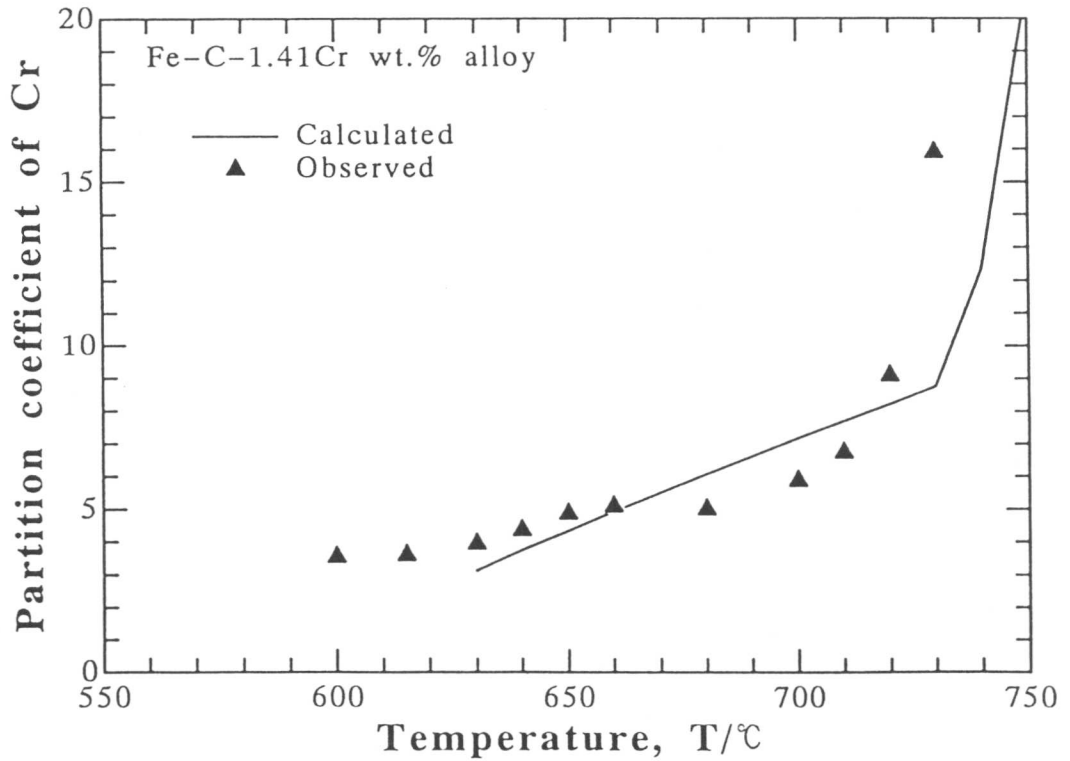


Fig. 5.16 Calculated partition coefficient of Cr in a Fe-1.41Cr-C wt.% alloy. Plots are after Ridley [8].

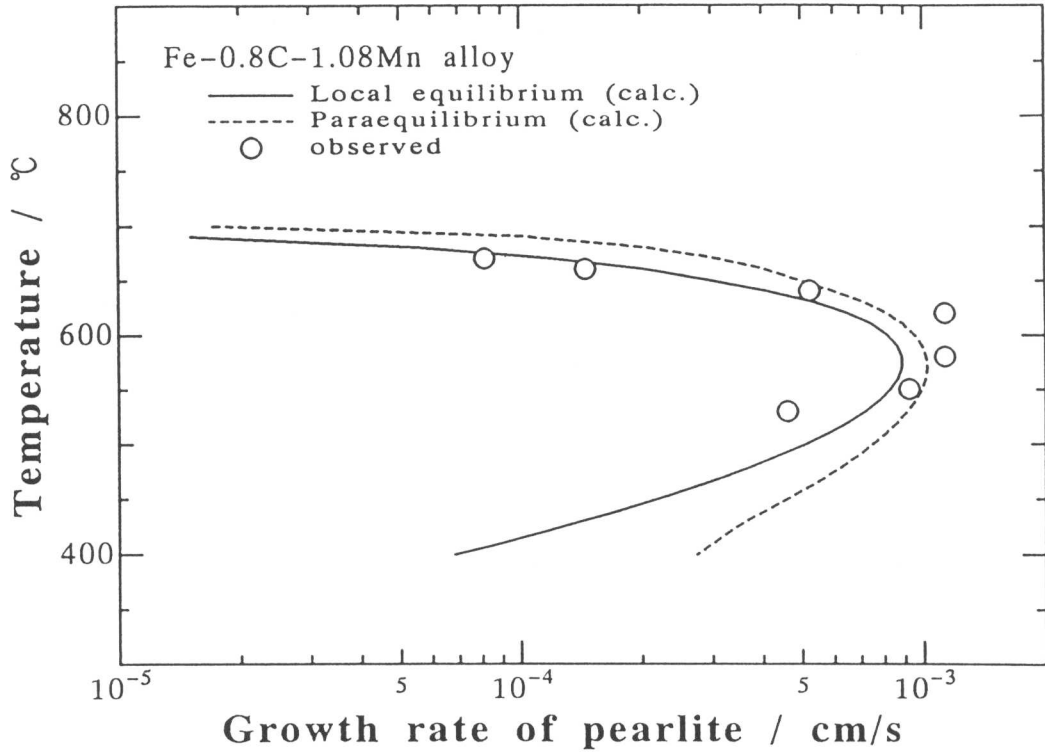


Fig. 5.17 Comparison between observed and calculated growth rate of pearlite in a Fe-1.08Mn-C wt.% alloy.

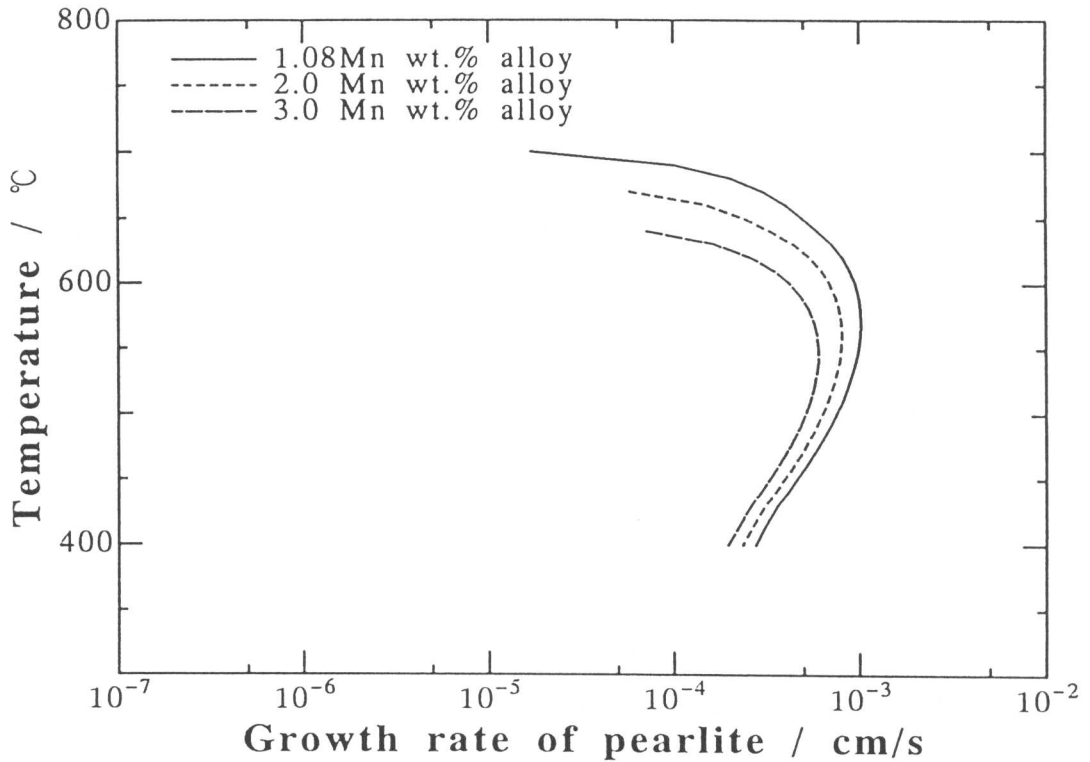


Fig. 5.18 Effect of the amount of Mn addition on the growth rate of pearlite under paraequilibrium.

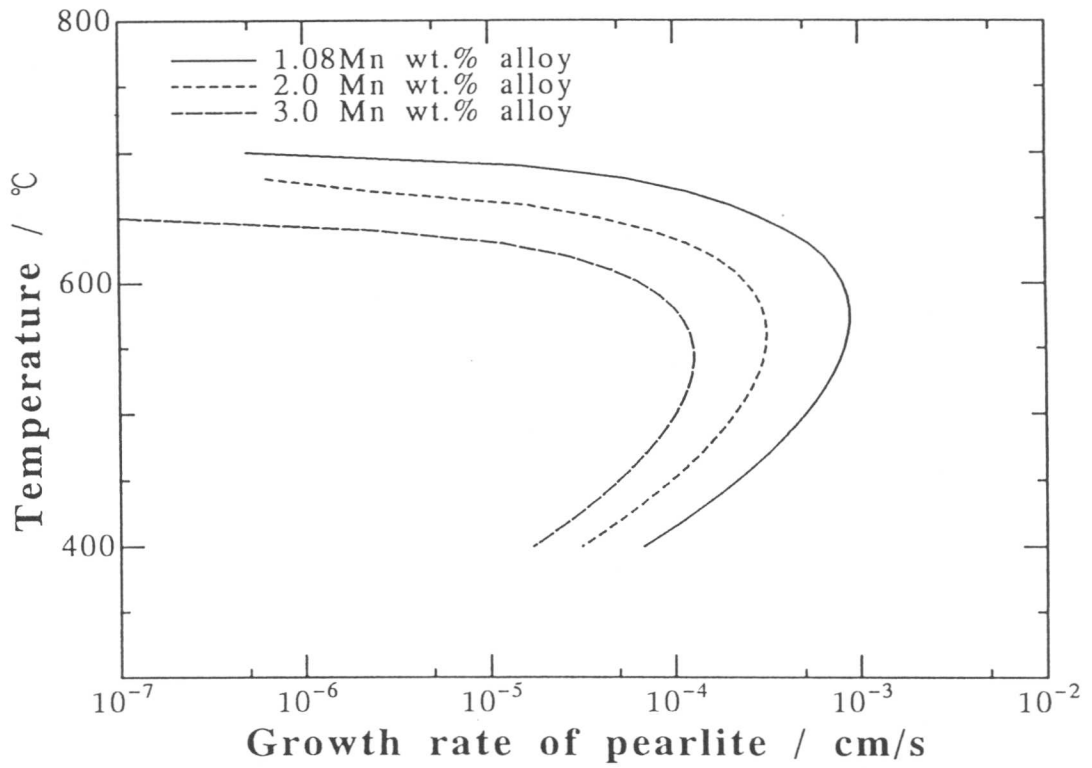


Fig. 5.19 Effect of the amount of Mn addition on the growth rate of pearlite under local equilibrium.

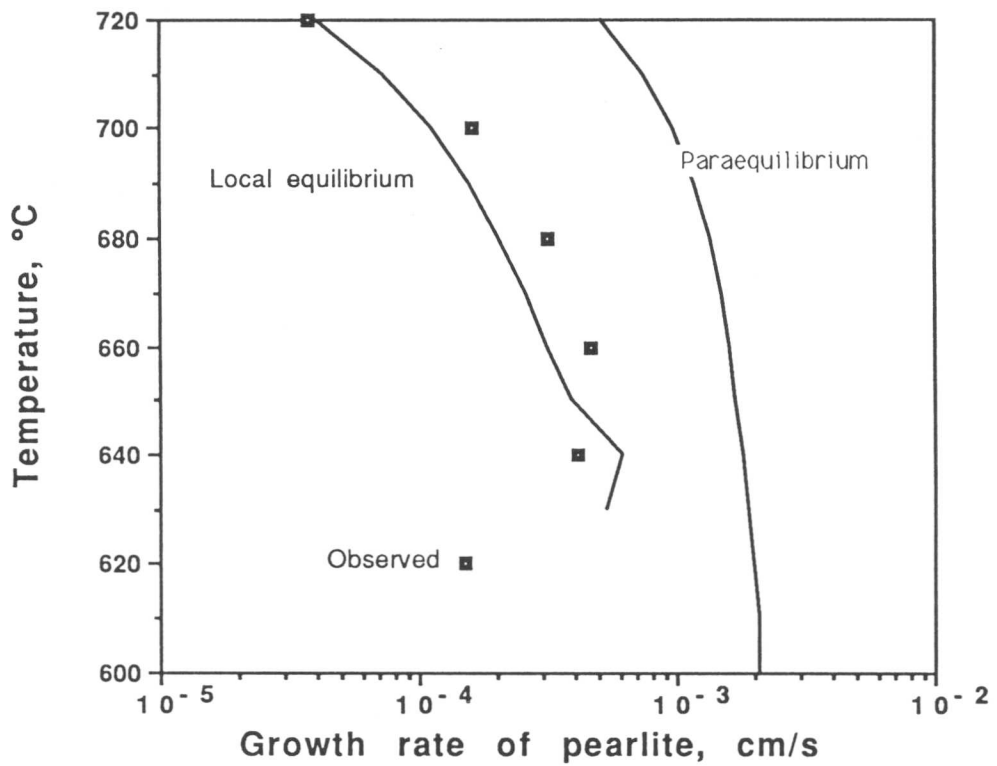


Fig. 5.20 Comparison between observed and calculated growth rate of pearlite in a Fe-1.41Cr-C alloy.

Table 5.2 Interlamellar spacing data for Fe-C, Fe-Mn-C, Fe-Ni-C and Fe-Cr-C alloys reported by (a) Brown and Ridley [15], (b) Razik *et al.* [16], (c) Ridley [8] and (d) Cahn and Hagel [17].

Temp. °C	Alloy wt%	S $\mu$ m	ref.	Temp. °C	Alloy wt%	S $\mu$ m	ref.
700		0.221	a)	672	1.98Ni	0.652	a)
680		0.130	a)	667	1.98Ni	0.379	a)
660		0.092	a)	660	1.98Ni	0.227	a)
640		0.071	a)	656	1.98Ni	0.201	a)
620		0.057	a)	652	1.98Ni	0.145	a)
690	1.08Mn	0.398	b)	647	1.98Ni	0.129	a)
685	1.08Mn	0.299	b)	641	1.98Ni	0.112	a)
680	1.08Mn	0.241	b)	629	1.98Ni	0.088	a)
670	1.08Mn	0.196	b)	620	1.98Ni	0.071	a)
660	1.08Mn	0.156	b)	648	3.00Ni	0.649	a)
640	1.08Mn	0.100	b)	644	3.00Ni	0.463	a)
620	1.08Mn	0.080	b)	640	3.00Ni	0.227	a)
670	1.80Mn	0.373	b)	633	3.00Ni	0.168	a)
660	1.80Mn	0.218	b)	625	3.00Ni	0.130	a)
650	1.80Mn	0.164	b)	616	3.00Ni	0.103	a)
640	1.80Mn	0.131	b)	605	3.00Ni	0.079	a)
630	1.80Mn	0.119	b)				
620	1.80Mn	0.104	b)				
610	1.80Mn	0.077	b)				
600	1.80Mn	0.065	b)				
Temp. °C	Alloy wt%	S $\mu$ m	ref.	Temp. °C	Alloy wt%	S $\mu$ m	ref.
720	1.80Cr	0.135	c)	706	0.40Cr	0.240	c)
705	1.80Cr	0.092	c)	696	0.40Cr	0.174	c)
690	1.80Cr	0.069	c)	680	0.40Cr	0.109	c)
670	1.80Cr	0.060	c)	660	0.40Cr	0.079	c)
650	1.80Cr	0.046	c)	637	0.40Cr	0.065	c)
630	1.80Cr	0.041	c)	620	0.40Cr	0.055	c)
620	1.80Cr	0.037	c)	790	9.00Cr	0.200	d)
710	0.90Cr	0.178	c)	750	9.00Cr	0.075	d)
700	0.90Cr	0.128	c)	700	9.00Cr	0.050	d)
680	0.90Cr	0.088	c)	675	9.00Cr	0.040	d)
660	0.90Cr	0.072	c)				
640	0.90Cr	0.057	c)				
618	0.90Cr	0.046	c)				

## CHAPTER 6

### REAUSTENITISATION ACCOMPANIED BY NUCLEATION OF AUSTENITE

#### 6.1 INTRODUCTION

The aim of this chapter is to study the effect of the initial microstructure on reaustenitisation, in circumstances where the nucleation of austenite is required. Martensitic microstructures and mixtures of ferrite and carbide particles, are studied as the starting microstructures. It is essential for austenite to nucleate in these cases unlike the mixture of bainite and austenite which was discussed in Chapter 4. Differences in the overall transformation kinetics between reaustenitisations with and without the need to nucleate austenite may provide insight into the effect of nucleation on reaustenitisation.

#### 6.2 EXPERIMENTAL PROCEDURE

All materials used in the experiments were homogenised at 1250 °C for 3 days before the heat treatment to obtain the appropriate initial microstructures. A Fe-0.3C-4.08Cr wt.% and a Fe-0.12C-2.0Si-3.0Mn wt.% alloys were heated to either 1250 °C or 1100 °C and were quenched into iced water to give martensitic microstructures. Mixtures of carbide particles and ferrite were obtained by tempering specimens of the martensitic microstructure either at 500 °C or at 700 °C. After these heat treatments, the specimens were “up-quenched” to the reaustenitisation temperatures at the fastest heating rate available (about 500 °C s<sup>-1</sup>) in order to investigate isothermal reaustenitisation, or were heated continuously at a variety of rates to study anisothermal reaustenitisation. The specimens were helium quenched in the dilatometer after the heat treatment. The cooling rate during quenching was about 30 °C s<sup>-1</sup> between 800 and 500 °C. The same methods were used for the nickel plating to prevent surface degradation and for the sealing of specimens into a quartz tube while they were heat treated in a furnace as mentioned in Chapter 4. After the experiments, specimens were examined as discussed in Chapter 4.

#### 6.3 ISOTHERMAL REAUSTENITISATION

The isothermal reaustenitisation behaviour of ferrite in which nucleation of austenite is required, is described in this section.

##### 6.3.1 Reaustenitisation from a martensitic microstructure

##### Martensitic initial microstructure in the Fe – 0.3C – 4.08Cr wt.% alloy

First, reaustenitisation from martensite in the Fe-0.3C-4.08Cr wt.% alloy, obtained by quenching from 1100 °C, was studied. An optical micrograph of the initial microstructure is shown in Fig. 6.1. A TEM micrograph of the specimen shows a lath martensitic microstructure (Fig. 6.2). The hardness of the initial microstructure was measured to be  $H_V\{98.1N\} = 551$ , which is very close to the value 582 calculated from the chemical composition and the cooling rate using the following equation (concentrations expressed in wt.%) [1].

$$H_V = 127 + 949C + 27Si + 11Mn + 8Ni + 16Cr + 21 \times \log\{\text{cooling rate, (}^\circ\text{C s}^{-1}\text{)}\} \quad (6.1)$$

The martensitic samples were then up-quenched to elevated temperatures to study isothermal re-austenitisation. Optical micrographs of the specimens helium quenched after 30 min of isothermal re-austenitisation at each reaction temperature are shown in Fig. 6.3. Austenite was not observed after reaction at 750 °C (Fig. 6.3 a). When the reaction temperature was raised to 780 °C, isolated islands of austenite (white regions, Fig. 6.3 b) were found. The preferential nucleation site of austenite is the prior austenite grain boundaries. The austenite particles are globular in shape or slightly elongated along the prior austenite grain boundaries. The volume fraction of austenite increased with the reaction temperature (Fig. 6.3 b,c,d) and a fully austenitic microstructure (fully martensitic on quenching to ambient temperature) can be obtained above 805 °C (Fig. 6.3 e).

The austenite particles which nucleated at the prior austenite grain boundaries tended to grow only into one of the two adjacent prior austenite grains. At some grain boundaries, all of the austenite particles were found to grow into the same prior austenite grain (indicated by arrows in Fig. 6.3 c). A magnified micrograph shows detail of the structure of austenite nucleated at a prior austenite grain boundary (Fig. 6.4). Most of the austenite particles seem to grow into one prior austenite grain and a coalescence between adjacent austenite particles seems to occur at the later stage of transformation.

Similar results have been reported by Speich *et al.* [2] and Law and Edmonds [3] for the formation of austenite from a mixture of ferrite and spheroidised cementite particles. These austenite particles were found to grow into a grain to which the austenite particles are not orientation related.

At relatively high temperatures (790 °C for 20 seconds), the prior austenite grain boundaries first became covered completely with newly formed austenite particles (Fig. 6.5). The new austenite particles coalesced to form an allotriomorph of austenite at the prior austenite grain boundaries. After the occurrence of the site saturation at the prior austenite grain boundaries, nucleation of austenite within the prior austenite grains seems to become more prominent (Fig. 6.6; 790 °C for 50 seconds). The austenite particles are rather acicular in shape instead of the globular grains which form at the prior austenite grain boundaries. The austenite plates found within a given martensite block were parallel to each other. This suggests that the austenite plates are influenced by the ferrite/ferrite interfaces. They grew along these interfaces as discussed by Plichta and Aaronson [4].

These microstructural features of re-austenitisation from martensite were also obtained when the prior austenite grain size was large. Specimens heated to 1250 °C for three days and quenched in iced water were re-austenitised. The amount of austenite which forms at 778 °C was found to be very small (Fig. 6.7) with individual austenite grains separated at the prior austenite grain boundaries. Small particles of austenite appears at a prior austenite grain boundary at an early stage of the reaction, which seem to grow along the boundary and bulge into one of the grains which are separated by the boundary.

#### Martensitic initial microstructure in the Fe - 0.12C - 2.0Si - 3.0Mn wt.% alloy

When a martensitic starting microstructure in the Fe-0.12C-2.0Si-3.0Mn wt.% alloy was heated, intragranular austenite was found to form as discussed by Plichta and Aaronson [4]. The prior austenite grain boundaries are no longer the most preferred nucleation sites as shown in Fig. 6.8, which illustrates partially re-austenitised microstructures. The austenite particles are acicular and there is almost no nucleation observed at the prior austenite grain boundaries. The

is, therefore, expected to be higher in ferrite than in austenite causing the difference in particle sizes in the two phases.

In some part of tempered region, dislocation networks can be observed. Fig. 6.12 a) shows an example of this in a specimen isothermally held at 790 °C for 20 seconds and quenched. Dislocations are found to be tied up by carbide particles in the tempered region. Interaction between the particles and dislocations can be clearly seen in another position of the specimen heat treated at 790 °C (Fig. 6.12 b). Fig. 6.13 shows a bright field image of a recovered ferrite microstructure where ferrite grains whose interfaces seems to be pinned by particles, are found. However, a dark field image of the area shows that those grains have almost the same orientations, suggesting that those grains are subgrains separated by dislocation networks.

The particles observed in the tempered region show a similar orientation which can be seen in Fig. 6.14, together with a bright and a corresponding dark field images. This may indicate that these particles have precipitated in ferrite with a reproducible orientation relationship with that phase.

Twinned martensite is often observed in austenite regions (Fig. 6.15), which suggests that the carbon concentration there is high. Microhardness measurements near interfaces between tempered ferrite and austenite were conducted with the indentation load of 0.0981 N. Since the microstructure which is to be examined is martensite with more than 0.3 wt.% of carbon, the hardness measurement with the load smaller than 0.0981 N causes a substantial scatter. A decrease in hardness near the interfaces was observed (Fig. 6.16). This may correspond to the carbon profile in austenite which is considered to be maintained while austenite grows (Fig. 6.17). There is, however, the possibility of interference from surrounding soft ferrite phase near the interfaces.

### Dilatometry

Typical relative length changes during isothermal reaustenitisation from martensitic initial microstructure obtained by water quenching from 1100 °C and from 1250 °C, are shown in Fig. 6.18 and Fig. 6.19. Since reaustenitisation happens during heating at high temperatures even at heating rates as high as 500 °C s<sup>-1</sup>, the temperature correction which was discussed in Chapter 4 was used here again. The temperature corrected relative length changes are plotted in Fig. 6.20. The rate of the reaction increases with temperature. The maximum relative length change at each temperature increases with temperature and reaches a maximum value. These features of isothermal reaustenitisation are very similar to those in the case of reaustenitisation from a mixture of bainitic ferrite and austenite. The maximum relative length changes were plotted against the reaction temperature in Fig. 6.21. As was observed for the initial microstructure of bainitic ferrite and austenite, the maximum relative length change shows a maximum value at around 790 °C which is identical to the value observed in the bainite + austenite initial microstructure within the accuracy of the experiments.

These two sets of the maximum relative length changes are compared in Fig. 6.22. The maximum relative length change at temperatures higher than 790 °C (100% austenite) is larger for the martensitic initial microstructure since the amount of ferrite available for transformation is larger. The  $\Delta L/L$  values at 790 °C for the two different initial microstructures are consistent with the initial amount of ferrite which is 1.0 in the martensitic initial microstructure and 0.7 in the other. The maximum relative length change above the peak temperature shows a linear decrease which is parallel to that in the bainite + austenite starting microstructure. This

feature can be attributed to the difference in the thermal expansivities of ferrite and austenite as discussed in Chapter 4.

The thermal expansion coefficient during cooling after isothermal reaustenitisation at each reaction temperatures are plotted in Fig. 6.23 with the data obtained for reaustenitisation from the mixture of bainite and austenite in the Fe-0.3C-4.08Cr wt.% alloy. The thermal expansion coefficients during cooling depend on the microstructure at the end of isothermal holding and vary with the volume fraction of austenite and ferrite; *i.e.*  $1.244 \times 10^{-5} \text{ } ^\circ\text{C}^{-1}$ , when the volume fraction of austenite is zero, to that of austenite; *i.e.*  $2.065 \times 10^{-5} \text{ } ^\circ\text{C}^{-1}$ , when the microstructure is fully austenitic. It can be said that the fully austenitic microstructure is obtained above  $790 \text{ } ^\circ\text{C}$ , consistent with the results obtained from dilatometry and from optical micrographs.

When the microstructure at the end of isothermal reaustenitisation contains austenite, decomposition of that austenite can be observed during cooling. The relative length changes during helium quenching after 30 min of isothermal reaustenitisation at each temperatures can be seen in Fig. 6.24. The temperatures at which the decomposition of austenite is first observed were plotted against the reaustenitisation temperature (Fig. 6.25). The decomposition-start temperature decreases with increasing the reaustenitisation temperature independent of the initial microstructure. Since the average carbon concentration in austenite is higher at lower reaustenitisation temperatures, decomposition of austenite is expected to be retarded more when the reaustenitisation temperature is lowered. The experimental result contradicts this. To understand this, the phase equilibrium calculation was conducted using “Thermo-Calc” for the Fe-0.3C-4.08Cr wt.% alloy, although calculated equilibrium phase boundaries are not completely in agreement with the experimental results obtained in the present work. “Thermo-Calc” gives phase boundaries as shown in Fig. 6.26 a in which *fcc*, *bcc*,  $\text{M}_7\text{C}_3$  and cementite were taken into account. As expected, the carbon concentration in austenite decreases with increasing temperature in the intercritical temperature range as shown in Fig. 6.26 b, but increases again with temperature when ferrite phase disappears. The chromium concentration, on the contrary, increases monotonically with temperature. This means that the kinetics of the formation of ferrite from austenite formed at an intercritical temperature can be retarded by higher concentration of chromium when the temperature is raised. Four temperatures, which are indicated as points **A**, **B**, **C** and **D** in Fig. 6.26 b,c, are selected to assess the effect of reaustenitisation temperature on the TTT curve for the formation of ferrite in this alloy. The TTT curve calculation method proposed by Bhadeshia [6] was used here. Using the equilibrium chemical compositions at these four temperatures, the TTT curves for these austenite compositions were calculated (Fig. 6.27). Both of the upper and lower C-curves are shifted to the right so the formation of ferrite is retarded by raising the reaustenitisation temperature. In addition to this, the lower the reaustenitisation temperature is, the smaller the austenite grain is expected, which also accelerates the reaction rate of ferrite formation.

### 6.3.2 Reaustenitisation from mixtures of ferrite and carbide particles

Two different mixtures of ferrite and carbide particles were studied. These initial microstructures were obtained by tempering the martensitic microstructure which was studied in the previous section at either 700 °C or at 500 °C.

#### Microstructure tempered at 500 °C

An optical micrograph of a specimen tempered at 500 °C for 17 hours is shown in Fig. 6.28. A TEM bright field image (Fig. 6.29) clearly shows a tempered microstructure. There are two types of carbides in this microstructure, one of which is rather small and elongated, and the other is larger and globular in shape. TEM diffraction patterns (Fig. 6.29) show that the former one is cementite and the latter  $M_7C_3$  carbide. As shown in Chapter 4, cementite precipitation occurs from carbon supersaturated bainitic ferrite below the  $B_S$  temperature. Therefore cementite precipitation is expected to occur at 500 °C (which is just above the  $B_S$  temperature) at least at the early stages of tempering. A prolonged holding at the temperature, however, may have allowed the  $M_7C_3$  carbide, which is thermodynamically more stable than cementite, to form. The specimens were then up-quenched to intercritical temperatures to study isothermal reaustenitisation. A typical microstructure obtained by 30 min at 784 °C is presented in Fig. 6.30. Austenite particles can be seen not only at the prior austenite grain boundaries but also within the grains, before all of the prior austenite grain boundaries are covered with newly formed austenite. The intragranular austenite as well as that nucleated at the grain boundaries were found to be globular in shape, in contrast to the formation of austenite from a martensitic microstructure. When the latter is heated, the prior austenite grain boundaries are first covered with austenite and intragranular transformation occurs afterwards. The shape of the austenite is acicular along the ferrite/ferrite interfaces in the tempered microstructure. Clearly, a nearly tempered microstructure contains ferrite/ferrite interfaces within the prior austenite grains, which are preferential nucleation sites for austenite. There are some prior austenite grain boundaries which are free from austenite formation as indicated by arrows in Fig. 6.30 even when austenite particles are found within the prior austenite grains.

#### Microstructure tempered at 700 °C

When a martensitic specimen was tempered at 700 °C for 51 hours, a slightly different microstructure was obtained. Fig. 6.31 shows carbide particles both at prior austenite grain boundaries and within the grains. The particles at the prior austenite grain boundaries are coarse and elongated along the boundaries, showing a “stitched” morphology. The particles at the boundaries appear disc shaped, of about 5  $\mu\text{m}$  diameter. The particles within the grains are small in comparison. When this microstructure is heated to 785 °C for 30 min, austenite particles nucleate both at the prior austenite grain boundaries and within the grains (Fig. 6.32). The preferred nucleation site is intragranular. Austenite particles can be found to grow across the boundaries as illustrated by the arrows in Fig. 6.32. In some regions, the growth of austenite is blocked by elongated carbide particles at the boundaries. This starting microstructure gives a more homogeneous dispersion of austenite than previously discussed.

During reaustenitisation from both the tempered martensitic microstructures, austenite nucleated within the prior austenite grains exhibited irregular (or wavy) interfaces. This may

be a result of a irregular substructure of the matrix which contains a lath martensitic microstructure, but is broken by prolonged isothermal holding at elevated temperatures. This substructure is not polygonal but acicular, and a sheaf like structure can also be seen which may provide various different direction of the growth of austenite causing wavy interfaces of the growing austenite.

A TEM micrograph of a specimen quenched after 30 min of isothermal reaustenitisation at 785 °C from the microstructure tempered at 700 °C is shown in Fig. 6.33. The micrograph contains an interface between tempered ferrite and austenite (now martensite). The carbide particles are found in both phases as discussed in the previous section. The particles are, however, almost of the same size in both phases. If the dissolution of carbide particles occurs in austenite after being engulfed, the particles found in austenite region are expected to be smaller than that in tempered ferrite region as shown in the starting microstructures of the bainite + austenite (Chapter 4) or martensite. This assumption, however, cannot explain the fact observed in the present case. The other possibility is due to the difference in the growth rate of carbide in each phase as discussed in the previous section. This assumption seems to be applicable for all of the cases. When the starting microstructure does not contain alloy carbide, the alloy carbide is required to nucleate and grow at the reaction temperature. The difference in the growth rate of carbide in each phase, as a result of the lower diffusivities of atoms in austenite than in ferrite, may play the most important role in determining the particle sizes in both phases; *i.e.* particles in austenite are smaller than those in ferrite. When the starting microstructure contains these carbide particles, these particles may grow or dissolve in both phases. The growth or dissolution of the particles may not be significant in the present case since the particles in the starting microstructure formed at 700 °C which is only 85 °C below the reaction temperature. As a result, the particles found in both phases are of almost the same size.

### Dilatometry

Relative length changes during reaustenitisation from a microstructure tempered at 500 °C are presented in Fig. 6.34. The maximum relative length change which can be obtained from these data after the temperature correction (Chapter 4) can be seen in Fig. 6.35. The changes obtained in the present work; *i.e.* reaustenitisation from mixtures of bainite and austenite, martensitic microstructures and tempered martensitic microstructures, are compared in Fig. 6.36. No significant difference can be found for these different initial microstructures except for the bainite and austenite mixture where the maximum relative length change for 100% of reaustenitisation is smaller than others, as discussed in the previous section.

## 6.4 CONTINUOUS HEATING REAUSTENITISATION

### 6.4.1 Dilatometry

The relative length changes during continuous heating are shown in Fig. 6.37. The overall reaustenitisation behaviour can also be seen in Fig. 6.38. The transformation-start and -finish temperatures can be determined from the relative length change during continuous heating as points at which the relative length deviate from the constant thermal expansion of the initial and final microstructures. The transformation-start and -finish temperatures are plotted against heating rate in Fig. 6.39. Both temperatures increase with heating rate, consistent with the data on reaustenitisation from a mixture of bainite and austenite.

### 6.4.2 Tempering of martensite during heating

When the starting microstructure is supersaturated martensite, tempering can occur during heating to the austenitisation temperatures. The importance of this has been pointed out by Baeyertz [7]. When a specimen is heated at a slow heating rate, the tempering can be detected using dilatometry. The relative length changes obtained during continuous heating of a martensitic microstructure are presented in Fig. 6.37. A small deviation from the normal thermal expansion effect is seen to occur before the onset of reaustenitisation, at around 300 °C, which is designated as the “tempering-start temperature” (marked by arrows in Fig. 6.37), As expected, the tempering-start temperature increases with the heating rate (Fig. 6.40).

The expected relative length change during the tempering of martensite can be calculated from the difference in volume between carbon supersaturated martensite and a mixture of ferrite and cementite:

$$\frac{\Delta L}{L} = \frac{a_{\alpha'}^2 c_{\alpha'} - a_{\alpha}^3 (1 - V_{\theta}) - \frac{1}{6} a_{\theta}^3 V_{\theta}}{a_{\alpha'}^2 c_{\alpha'}} \quad (6.2)$$

where  $a_{\alpha'}$  and  $c_{\alpha'}$  are lattice parameters of martensite,  $a_{\alpha}$  is that of ferrite and  $a_{\theta}^3$  is the volume of cementite per unit cell, respectively. The volume fraction of cementite formed by tempering of carbon supersaturated martensite can be calculated from the total amount of carbon in the martensite. The thermal expansion coefficient of martensite was assumed to be identical to that of ferrite. The constants discussed in Chapter 4 were used here for the lattice parameters and the thermal expansion coefficients. The relative length change in equation 6.2 was calculated to be  $-0.00077$ . This decrease in relative length change is consistent with the experimentally observed one during heating and also during isothermal holding at 500° C for 30 min (Fig. 6.41). To compare this value with the experimentally observed contraction due to tempering, relative length changes at each heating rates were measured as differences between the two linear expansion lines before and after the tempering effect. The average of these values gives  $-0.00036$ . The smaller observed magnitude can be attributed to incomplete tempering.

## 6.5 CONCLUSIONS

Reaustenitisation from either martensite or mixtures of ferrite and carbide particles has been studied, in circumstances where new nucleation of austenite is necessary.

- 1) Prior austenite grain boundaries are the preferred nucleation sites for reaustenitisation from a martensitic initial microstructure, but are less prominent when the starting microstructure is tempered martensite in a Fe-0.3C-4.08Cr wt.% alloy. Almost no nucleation of austenite was observed at the prior austenite grain boundaries during reaustenitisation from martensite in a Fe-0.12C-2.0Si-3.0Mn wt.% alloy. The reason for this is not clear.
- 2) Formation of austenite within prior austenite grains became possible in the Fe-0.3C-4.08C wt.% alloy after the prior austenite grain boundary sites became saturated.
- 3) Austenite particles found at the prior austenite grain boundaries were globular whereas those formed within the grains are acicular in the case of reaustenitisation from martensitic initial microstructures. Globular austenite can, however, be found within the prior austenite grains when tempered martensite (a mixture of ferrite and carbide particles) is reaustenitised.
- 4)  $M_7C_3$  particles observed in the untransformed ferrite matrix are larger than those in the austenite region when the starting microstructure is martensite, whereas no significant

- difference in the particle size was observed for the starting microstructure tempered at 700 °C. This suggests that the difference in the particle size can be attributed to the difference in the growth rate of the particles in both phases.
- 5) When martensitic initial microstructure is heated slowly, tempering can occur on heating, and the starting temperature increases with heating rate. Even in the case of high heating rates carbide precipitation seems to occur at the very early stages of the reaction.

#### REFERENCES

1. R. Blondeau, Ph. Maynier, J. Dollet and B. Vieillard-Baron: "*Heat Treatment '76*", *Metals Society, London*, 1976, 189.
2. G. R. Speich and A. Szirmae: *Trans. TMS-AIME*, 1969, **245**, 1063.
3. N. C. Law and D. V. Edmonds: *Metall. Trans.*, 1980, **11A**, 33.
4. M. R. Plichita and H. I. Aaronson: *Metall. Trans.*, 1974, **5**, 2611.
5. J. Fridberg, L-E. Törndahl and M. Hillert: *Jernkont. Ann.*, 1969, **153**, 263.
6. H. K. D. H. Bhadeshia: *Metal Sci.*, 1982, **16**, 159.
7. M. Baeyertz: *Trans. ASM*, 1942, **30**, 458.



Fig. 6.1 Optical micrograph of martensite obtained by water quenching from 1100 °C in the Fe-0.3C-4.08Cr wt.% alloy.



Fig. 6.2 TEM bright field image of martensite obtained by water quenching from 1100 °C in the Fe-0.3C-4.08Cr wt.% alloy.

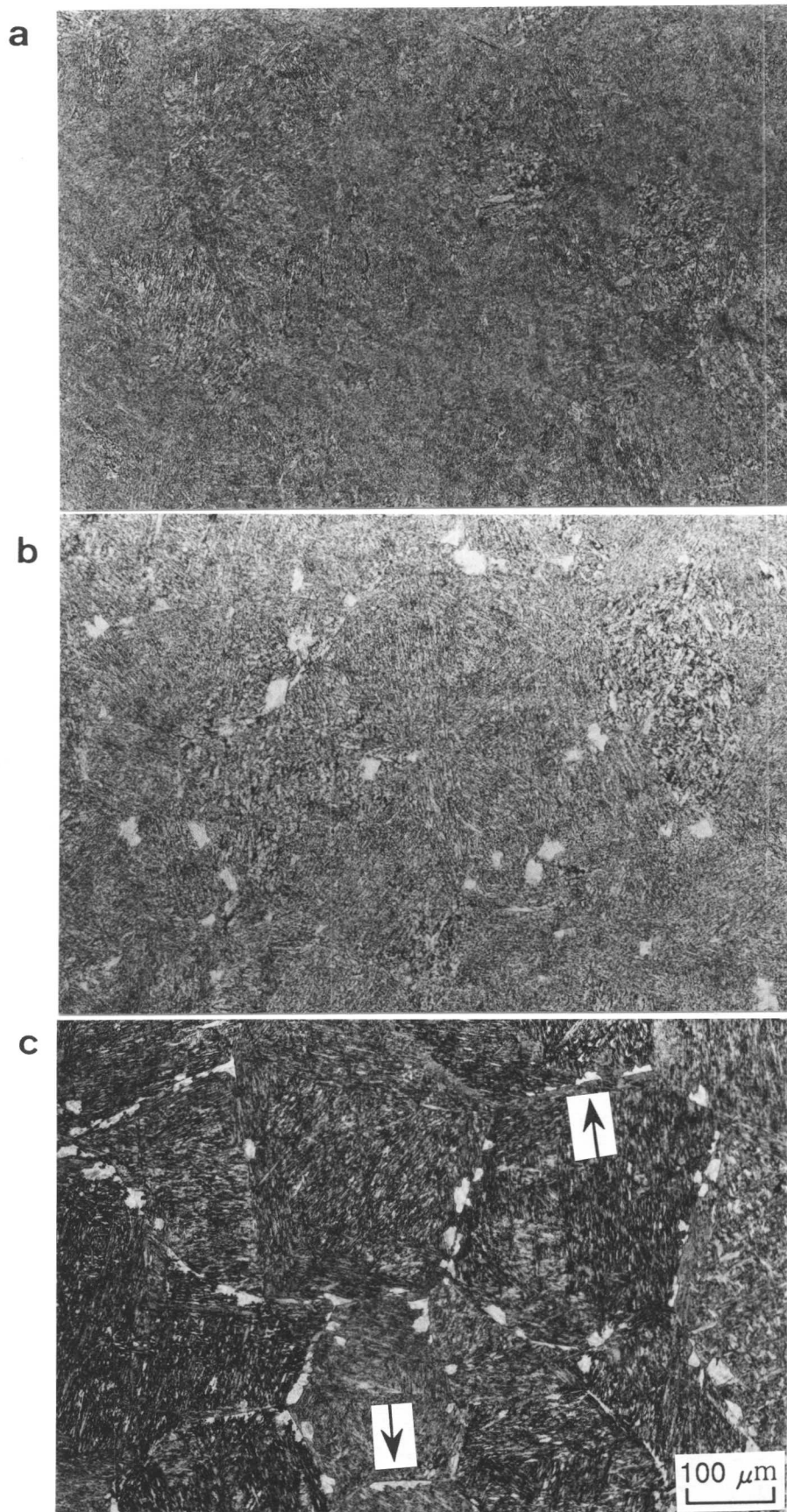


Fig. 6.3 Optical micrographs of specimens helium quenched after 30 min of isothermal re-austenitization at a) 750 °C, b) 780 °C, c) 785 °C, d) 800 °C and e) 805 °C.

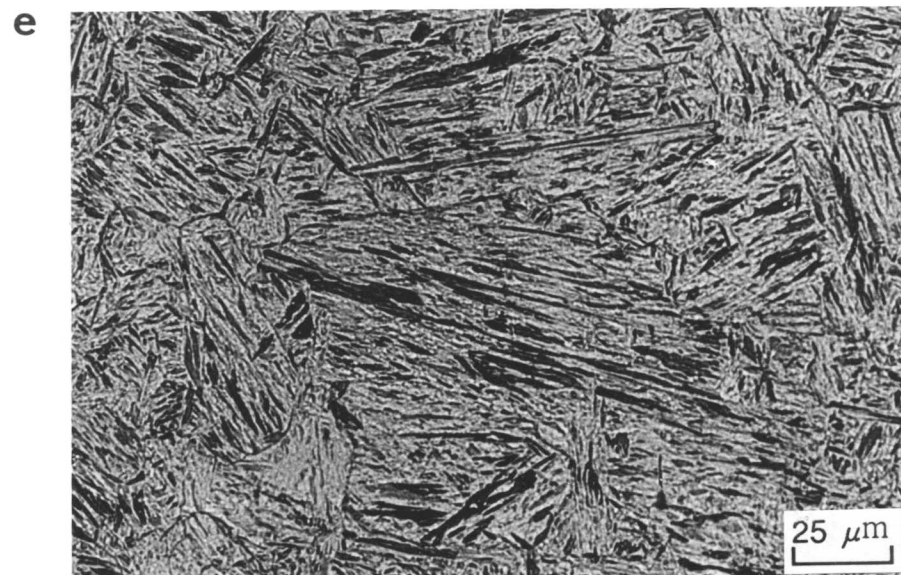
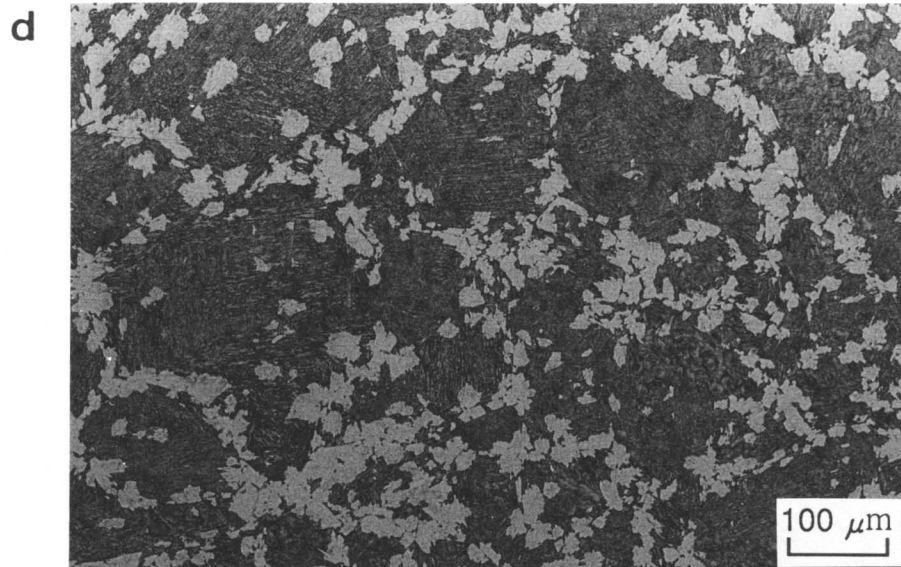


Fig. 6.3 (continued)

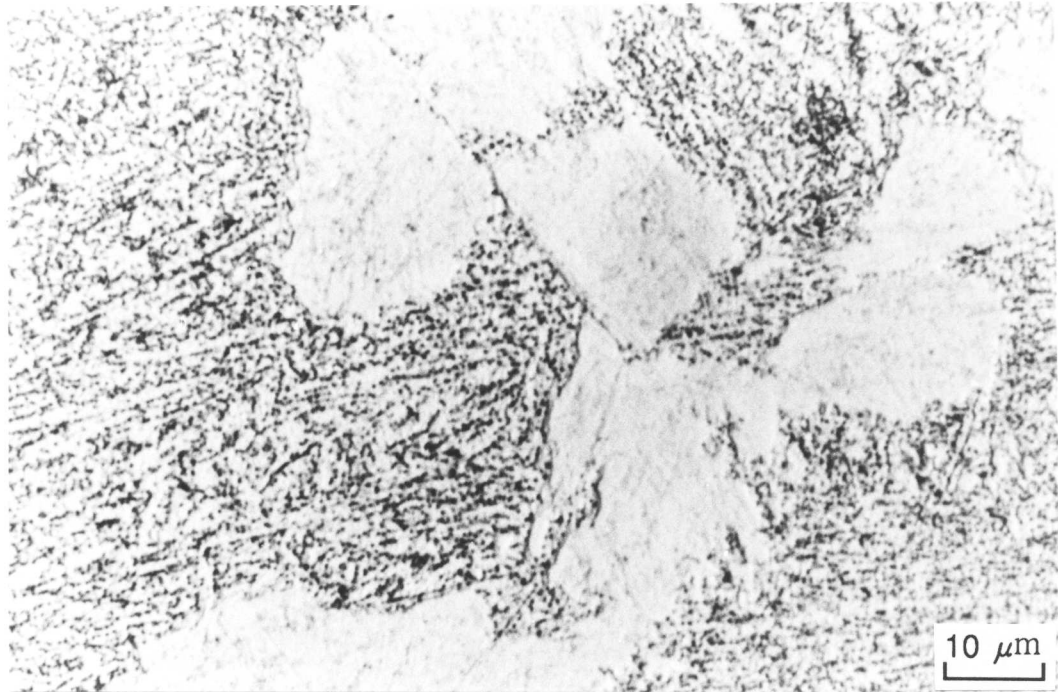


Fig. 6.4 Optical micrograph of a specimen helium quenched after 30 min of isothermal reaustenitisation at 800 °C.

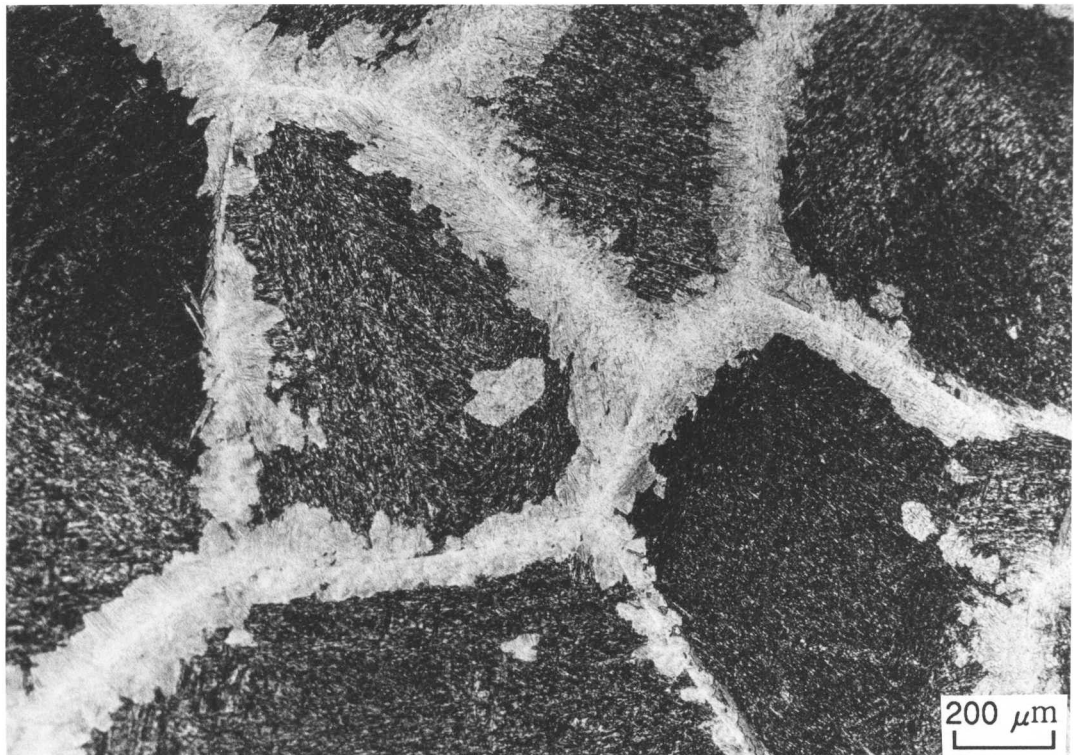


Fig. 6.5 Optical micrograph of a specimen helium quenched after 20 seconds of isothermal reaustenitisation at 790 °C showing a polycrystalline layer of austenite at the prior austenite grain boundaries.

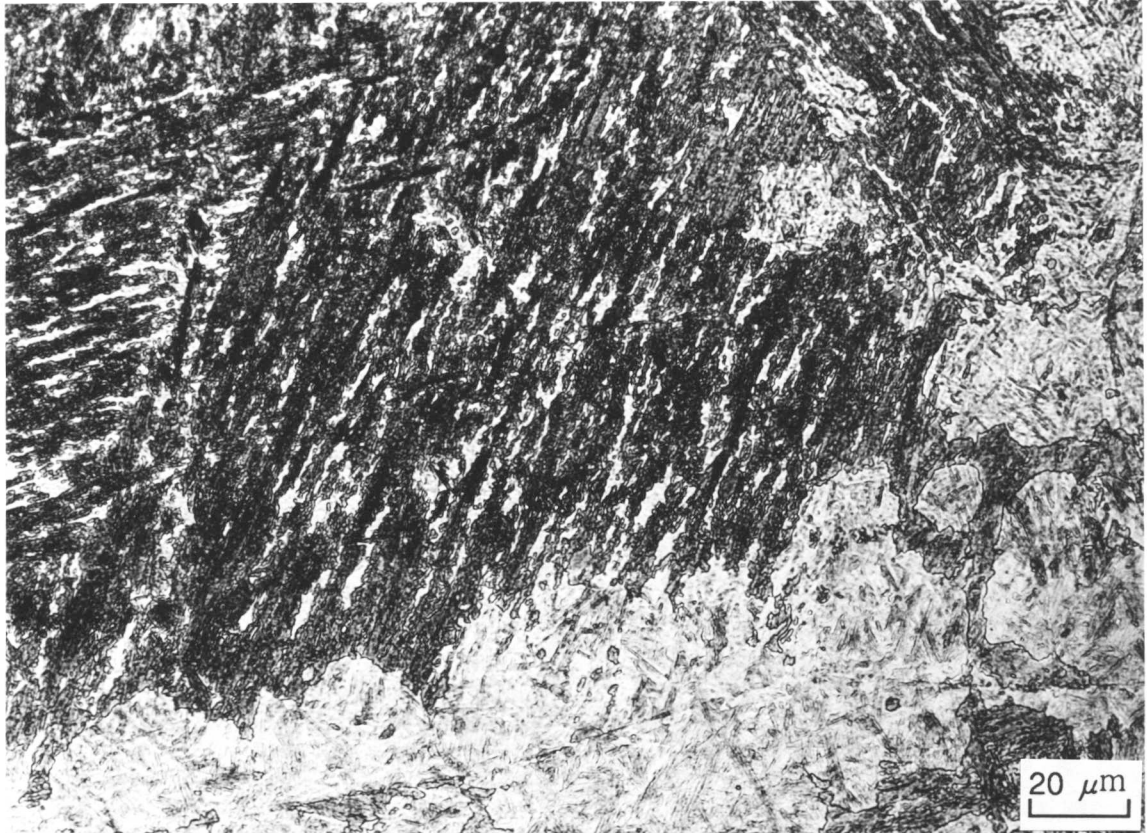


Fig. 6.6 Optical micrograph of a specimen helium quenched after 50 seconds of isothermal reaustenitisation at 790 °C.

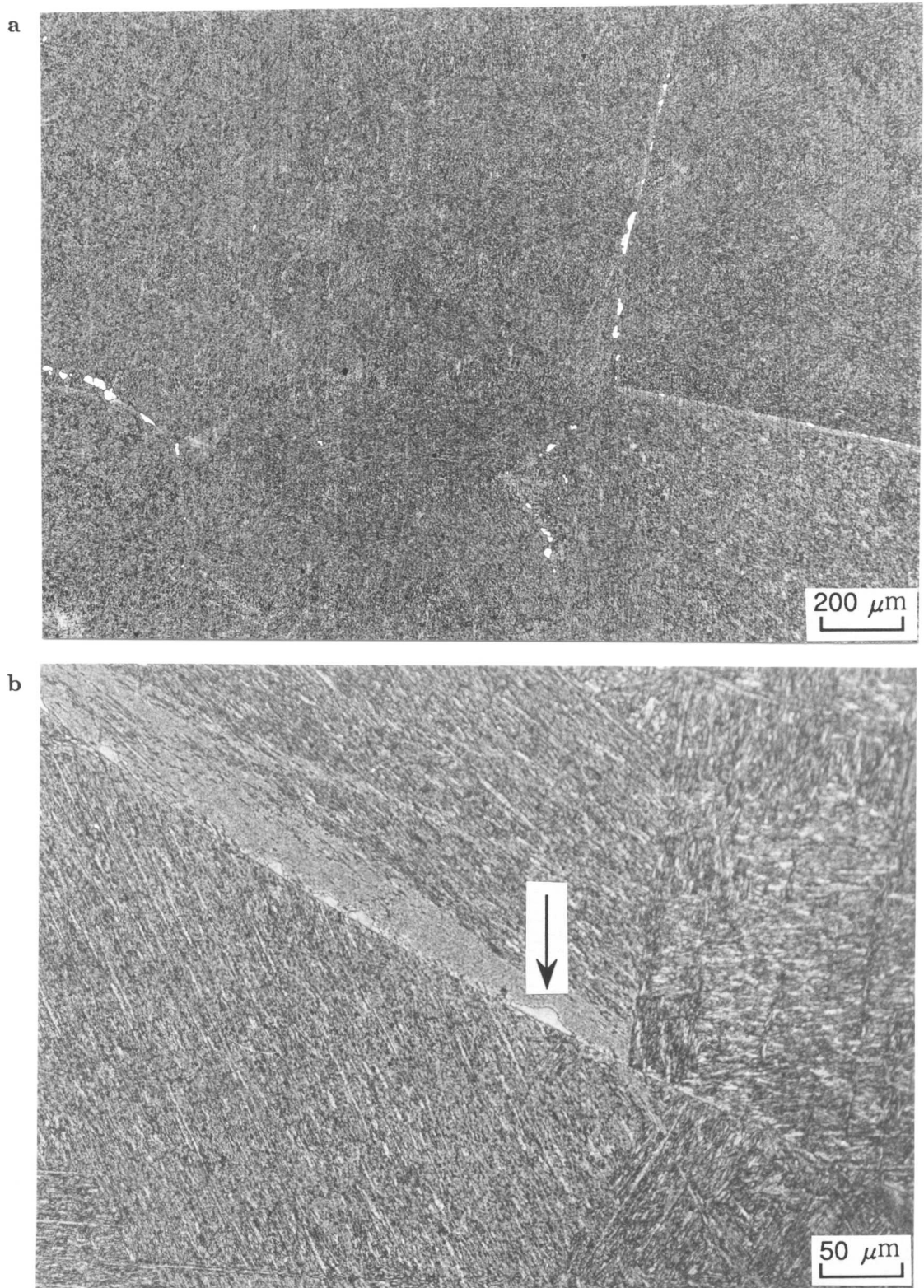


Fig. 6.7 Optical micrograph of a specimen helium quenched after 30 min of isothermal reaustenitisation at 778 °C. The initial microstructure is martensite obtained by water quenching from 1250 °C.

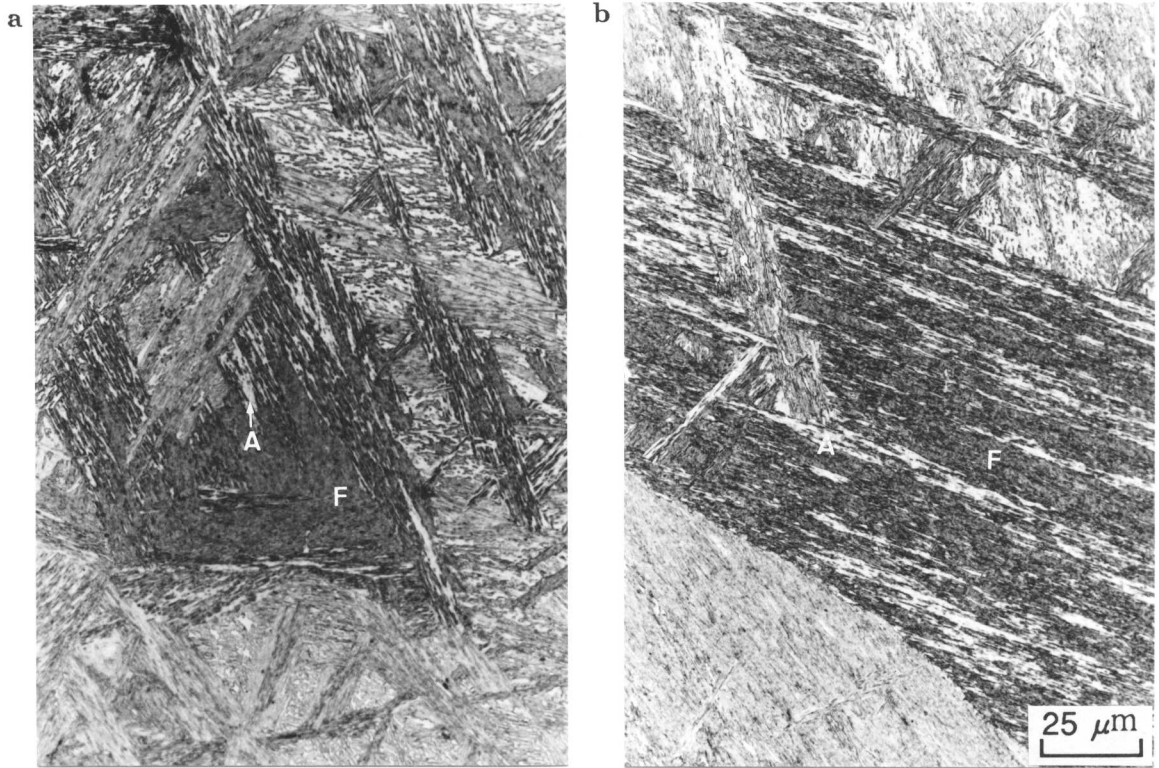


Fig. 6.8 Optical micrograph of a specimen helium quenched after 30 min of isothermal re-austenitisation at a) 770 °C and b) 790 °C. The initial microstructure is martensite obtained by water quenching from 1250 °C in the Fe-0.12C-2.0Si-3.0Mn wt.% alloy. (A: austenite, F: ferrite)



Fig. 6.9 TEM bright field image of a specimen helium quenched after 20 seconds of isothermal re-austenitisation from martensite at 790 °C in the Fe-0.3C-4.08Cr wt.% alloy.

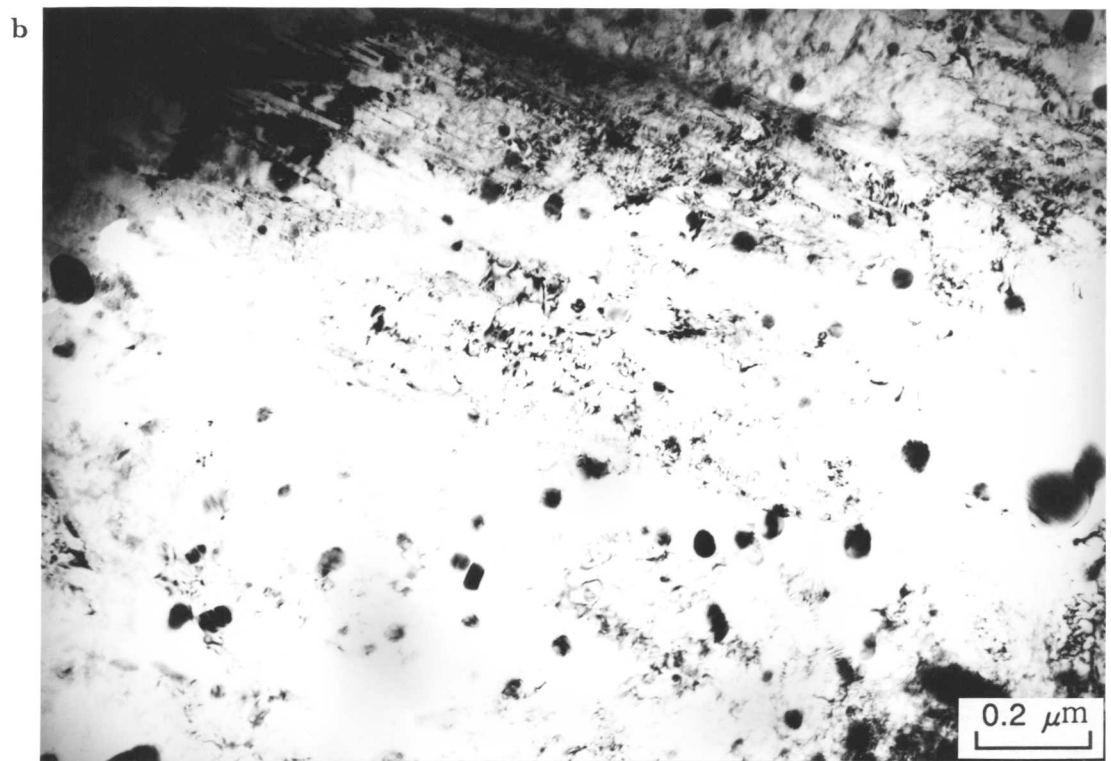


Fig. 6.10 TEM bright field images of a specimen helium quenched after 30 min of isothermal re-austenitisation from martensite at 800 °C. a) represents an untransformed part and b) an austenitised area in the Fe-0.3C-4.08Cr wt.% alloy.

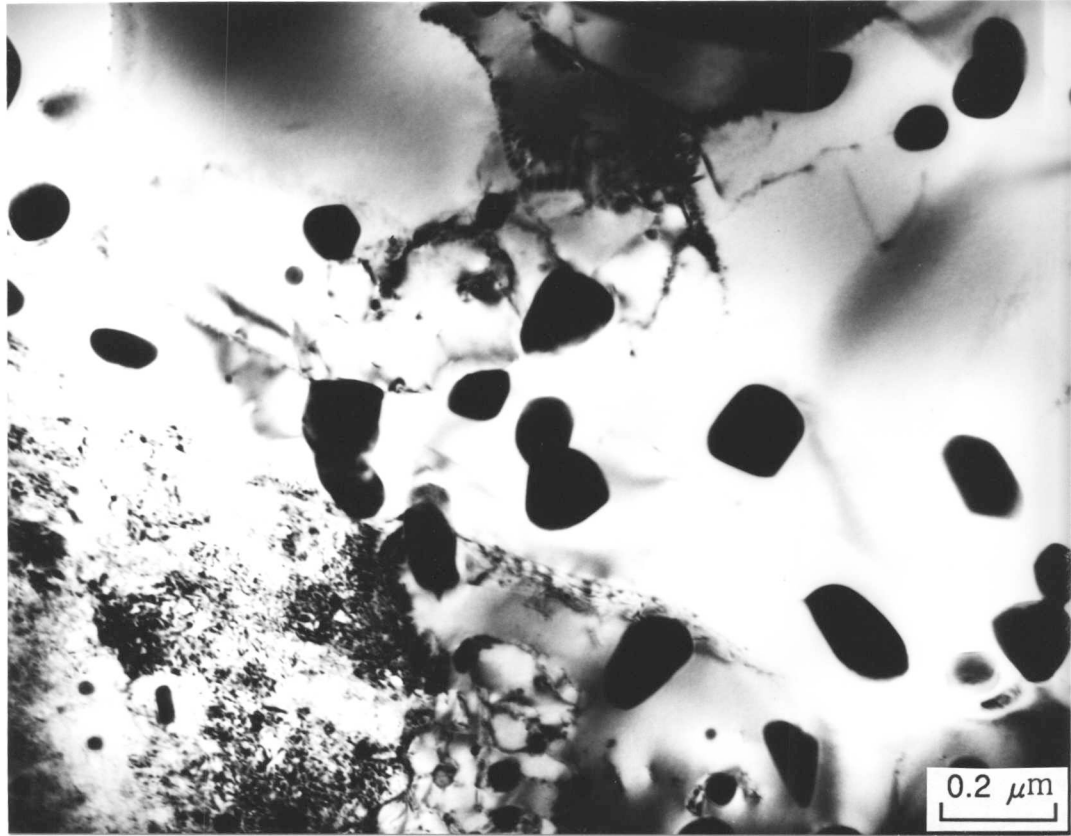
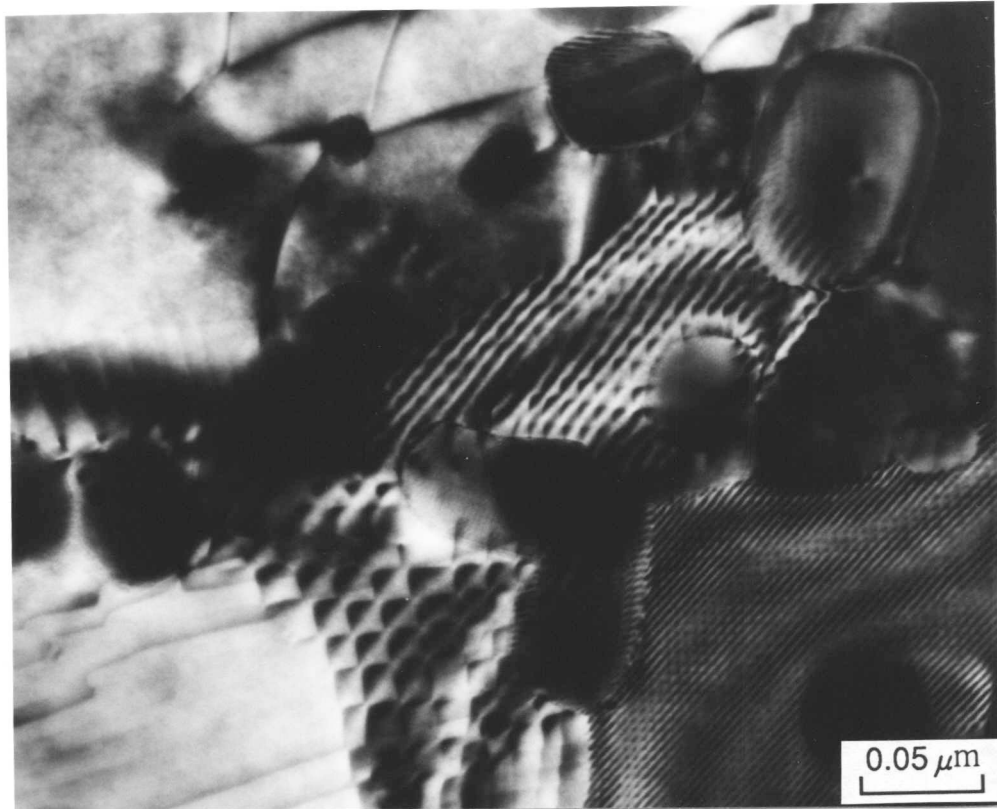


Fig. 6.11 TEM bright field image of a specimen helium quenched after 30 min of isothermal reaustenitisation from martensite at 785 °C in the Fe-0.3C-4.08Cr wt.% alloy.

a



b

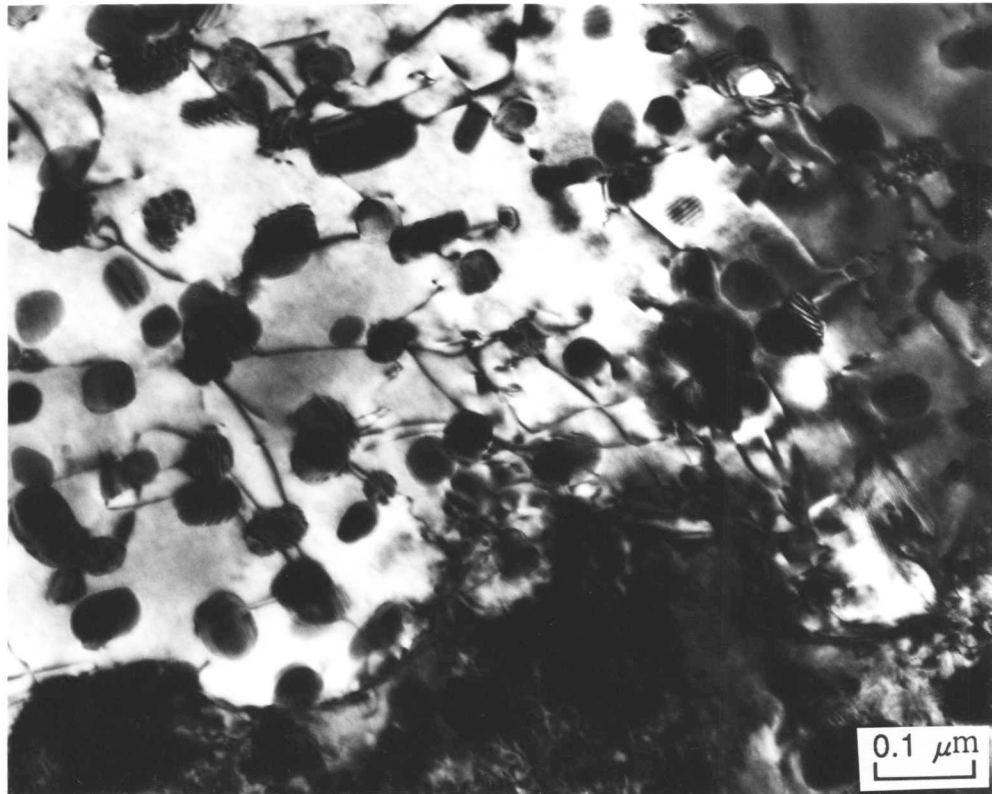


Fig. 6.12 Dislocation networks which are found in an untransformed region tempered during isothermal reaustenitisation for 20 seconds at 790 °C in the Fe-0.3C-4.08Cr wt.% alloy.

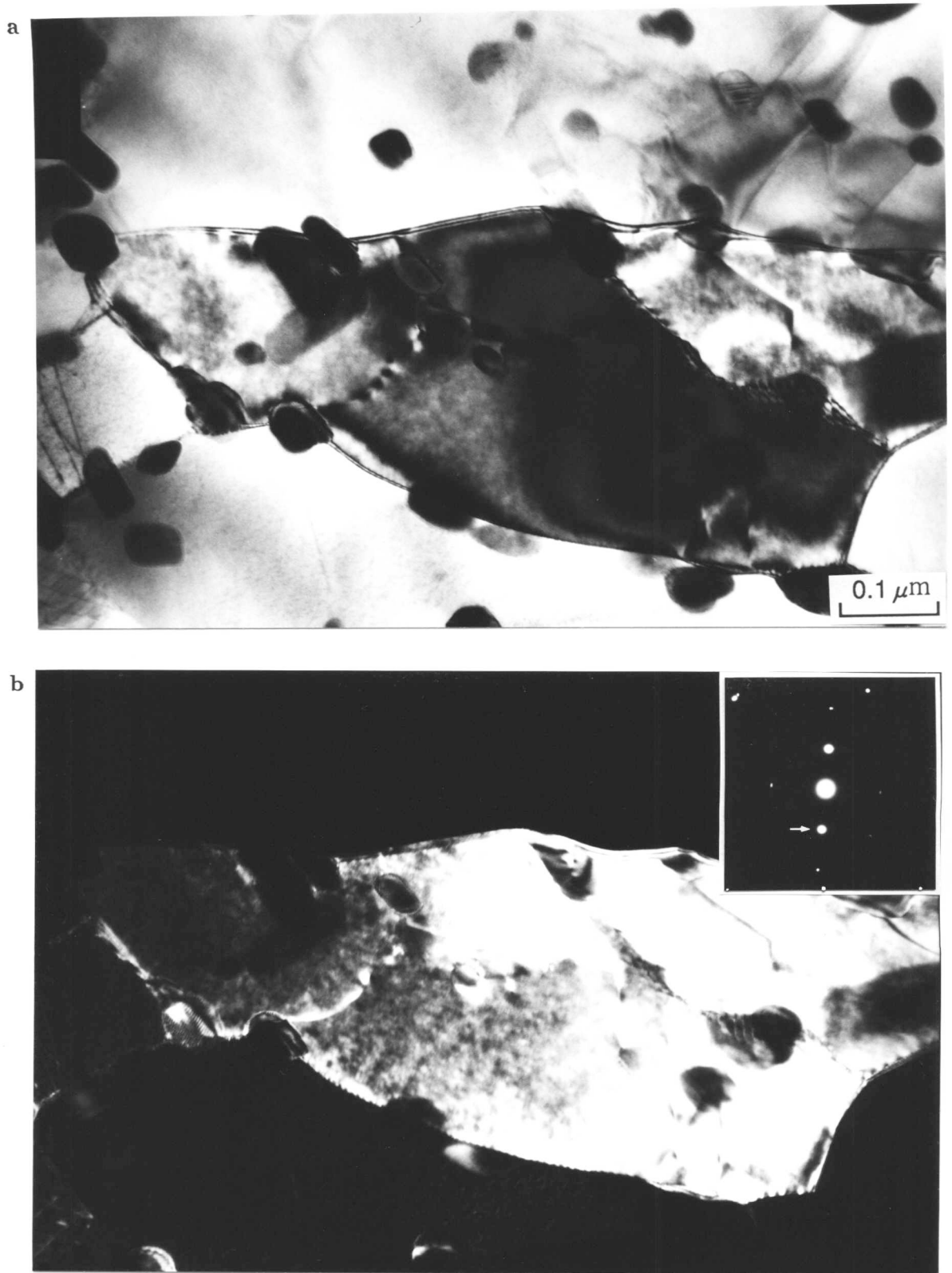


Fig. 6.13 TEM bright and dark field images showing a subgrain structure in a tempered martensite region after reaustenitisation at 790 °C in the Fe-0.3C-4.08Cr wt.% alloy.

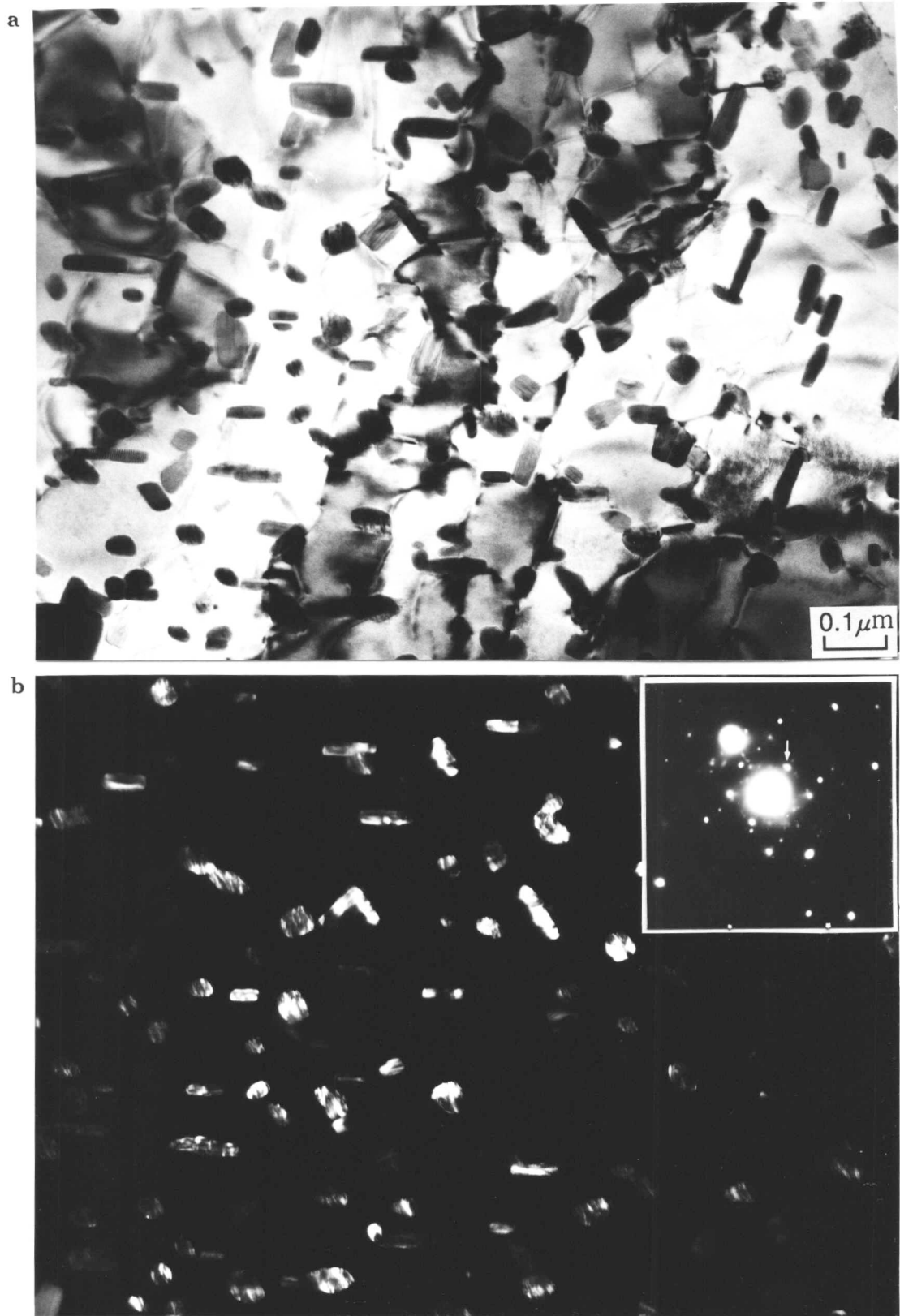


Fig. 6.14 TEM bright and dark field images of carbide particles found in the tempered martensite region in the Fe-0.3C-4.08Cr wt.% alloy.

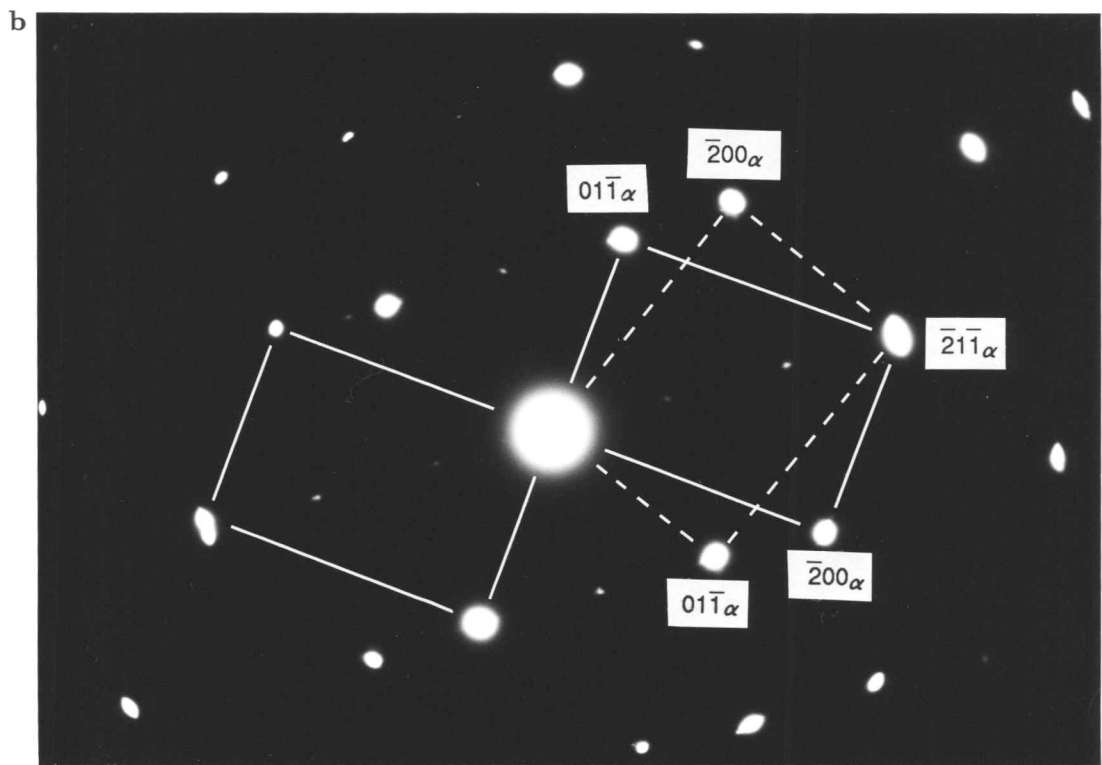
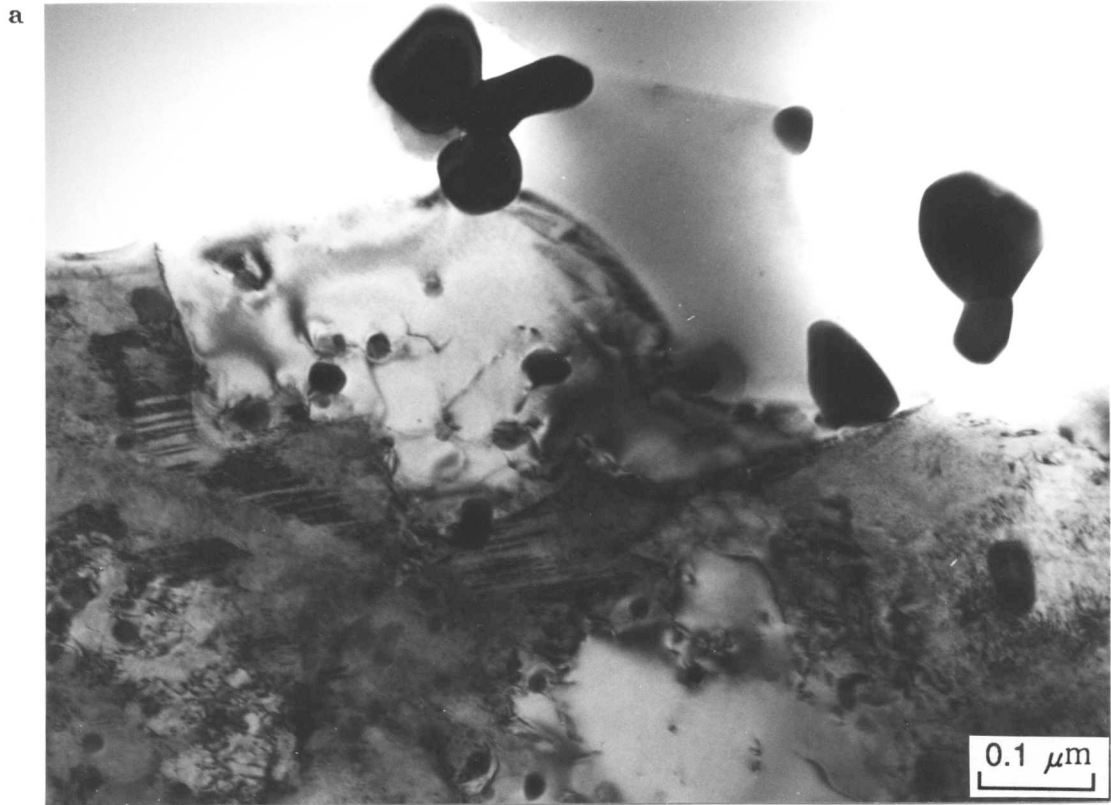


Fig. 6.15 Twinned martensite observed near the interface between austenite and untransformed ferritic matrix and a selected area electron diffraction pattern showing a twin relation.